Multi Contrast, Multi illumination and Microwave Imaging of 2D Inhomogeneous Scatterers.

Md. Mosharrof Hossain

A Thesis

in

The Department

of

Electrical and Computer Engineering

Presented in Partial Fulfillment of the Requirements

for the Degree of Master of Applied Science at

Concordia University

Montreal, Quebec, Canada

March 2006

Your file Votre référence
ISBN: 0-494-14261-8
Our file Notre référence
ISBN: 0-494-14261-8

Multi contrast, and Multi illumination and Microwave Imaging of 2D Inhomogeneous Scatterers.

Abstract

Md. Mosharrof Hossain

In this thesis, we consider the microwave imaging for reconstructing the material properties of inhomogeneous lossy dielectric cylinders using scattered field data. The scattered field is numerically computed using direct/forward method. The scatterer is an inhomogeneous two-dimensional (2D) arbitrary-shaped cylindrical structure containing impurities at any transverse location. The scatterer is immersed in a known dielectric media (like air, water, saline-water etc). The known surrounding dielectric is used as an observation domain whereas the complex scatterer is used as an investigation domain. Unrelated multi sources are used to illuminate the scatterer at different angles for reconstructing the less erroneous complex permittivity profile. Multi-frequency effect with the noise is addressed during the reconstruction of the complex permittivity profile using numerical simulations.

The objective function as well as the permittivity profile are computed using an inverse scattering method from the corresponding scattered field. The two-dimensional "Lippmann-Schwinger" integral equation for nonlinear inverse-scattering problem is discretized by the method of moment (MoM). Uniform rectangular discretization and a special proposed layered cylindrical discretization technique that provides better reconstruction of the permittivity profile, are applied throughout. The resulting ill condition matrix of the integral equation is solved by the pseudo-inversion algorithm.

The numerical simulations show the effect of different high contrasts in the layered scatterer (like human head, breast or whole human body) with complex permittivity on the reconstruction of the desired profile. Extensive numerical simulations are carried out to analyze the effect of contrast of different scatterers on the reconstruction of permittivity profile, the effect of multi view illumination on the reconstruction of scatterer's permittivity profile, the effect of noise on the reconstruction of dielectric profile and the effect of frequency on the reconstructed profile either for the transverse magnetic (TM) or transverse electric (TE) case.

The total and scattered electromagnetic fields on the scatterer measured from the numerical simulation using the proposed algorithm are validated by comparing with published results. In the sequence of the validation, the simulated complex permittivity profile is also compared with published results and with the Born approximation method for weak scatterers. At last, the uncertainty of the algorithm is measured by satisfying the boundary condition on the cross-section of the investigated dielectric object.

Acknowledgements

I would like to express my humble gratitude to Professor Dr. A. R. Sebak of Concordia University for his valuable support, proper guidance, incessant supervision, respective comments and continuous encouragement throughout this research. Also I would like to express my hearten thanks to all of the member of EMC group for providing suggestive discussion and friendly environment in the research lab and to the all faculty member and staffs of Electrical Engineering department, Concordia university.

I would like to thank my little kids and my wife for their patience, endurance and unremitting support. Finally thanks to all of my family and my best wishers for their spiritual assistance. At last I express my gratitude to Almighty Allah keeping my whole family always healthy.

TABLE OF CONTENTS

LIST OF FIGURES

LIST OF TABLES

CHAPTER-1

Introduction

1.1 Introduction:

Motivations, objectives and over views of this thesis are mainly described in this chapter. Our main goal is to show the interaction of the electromagnetic fields with scatterers including a human body for reconstructing their dielectric profiles. Various effects on the reconstruction of the dielectric profile are discussed. At last, the over view of different chapter of this thesis is described.

1.2 Motivation:

When microwave imaging was proposed as a noninvasive technique in medical applications, the potential advantages of this technology seemed to allow great developments with the early work in this area summarized in [1]. In the context of medical diagnostics, microwave imaging was indicated as the future leading technique for microwave decimetry [2]. Microwave imaging mammography has potential advantage compared to X-ray mammography and Computed Tomography (CT) scanning [3]. More than for any other cancers, breast tumors have electrical properties at microwave frequencies that are significantly different than those of healthy breast tissues. A normal breast tissue is also more transparent to microwave signals than many other

tissues, such as muscle or brain. A published report from U.S. Institute of Medicine (IOM) reviews the current state of mammography and other technologies suggested for breast cancer screening [4]. According to the report, there are some limitations of mammography such as missing data of breast cancers up to 15%, difficulty in imaging women with dense breasts and inconclusive results. Approximately 10% of mammograms contain suspicious areas and less than 10% of these are diagnosed as malignancies. Diagnosis often involves waiting for further imaging or biopsies. The limitations of X-ray mammography provide a clear motivation for the development of complementary breast-imaging tools to assist in detection and diagnosis. Magnetic Resonance Imaging (MRI) is useful for examining women with implants but it is expensive and currently unproven as a screening tool [4]. Microwave imaging for tumor detection has the potential to be both sensitive and specific, to detect small tumors and to be less expensive than MRI and nuclear medicine. The key to sensitivity, specificity and the ability to detect small tumor is the electrical property (conductivity, permittivity etc) contrast. The dielectric constant and conductivity for cancerous breast tissue is three or more times greater than that of the host tissue [5]. The contrast between normal and malignant breast tissue is closer to 1:2 [6]. The denomination of microwave imaging was almost exclusively restricted to remote sensing or radar situation, corresponding to large-range. Recently, microwave technology was used for Industrial, Scientific and Medical (ISM) applications via microwave imaging and real time vision of imaging to provide obstacle detection, precise navigation and route planning for transportation. Microwave imaging involves the use of non-ionizing, low power radiation, and is thus less hazardous

than other forms of radiation. It has an advantage over ultrasound imaging in its ability to penetrate air and bone. Limitations of existing systems for imaging dielectric objects encourage implementation of microwave imaging system.

1.3 Objectives and Methodology:

The present thesis describes a simple algorithm to reconstruct the dielectric profile of the cross section of the scatterer and to determine the portion of the target area that is occupied by a scattering object, due to frequency varying incident fields. Also a special discretization technique of the nonlinear and ill posed integral equation of the inverse scattering problem is used to obtain more accurate results. In particular, we assume that the scatterers have unknown cross-section, shape and dielectric properties. They are located at unknown position inside a fixed area of interest. Moreover, the scatterers are assumed to be characterized by dielectric parameters that do not vary along its axis. We assume that the electromagnetic wave propagates in a direction perpendicular to the cylindrical axis, with the incident electric field vector polarized and uniform along this axis. Under the above assumptions, the problem becomes a two-dimensional inverse scattering one. This assumption is effective for either weak or strong scatterer. The object is illuminated by the known source in multi directions for a better-reconstructed profile.

To this end, the integral equation of the electromagnetic scattering is discretized by the method of moment (MoM) [8]. It is expressed in terms of the total as well as scattering fields and the distribution of the equivalent current density of the whole area. The total field due to interaction of the known electromagnetic field on the dielectric

body is computed according to the Richmond theory [9]. A pseudoinverse algorithm [10], [11] is used to solve this system owing to the ill conditioning of the problem. The problem is then reduced to solving a linear algebraic system whose coefficients depend only on the problem's geometry, the physical properties of the propagating media and the frequency. Our final goal is to deduce the distribution of the permittivity profile in the area of interest by solving the related matrix equation.

1.4 Overview of the Thesis:

Chapter 2 reviews the literature for microwave imaging. Various previous methods for microwave imaging are briefly presented and discussed.

Chapter 3 reviews formulation of total and scattered fields radiated by a dielectric cylinder of arbitrary cross-section for the Transverse Magnetic (TM) case. The mathematical formulation is derived in terms of equivalent current for all kinds of scatterers. From the equivalent surface current as well as scattered field, the objective function as well as the complex dielectric permittivity are derived. For numerical simulation, the Maxwell's equation and Helmholtz equation are discretized by the method of moment using Dirac delta for both the basis and testing functions (point matching method) to avoid the required number of integrations.

Mathematical expression of the total field as well as the scattering field are also derived for the Transverse Electric (TE) case. Formulation of analytical solution for scattered field is reported in appendix C.

In Chapter 4, we present numerical results to validate the proposed algorithm with

published work, exact solution (if available) and with well-recognized "Born Approximation" for weak scatterers. There are two parts in the proposed algorithm: direct/forward scattering and inverse scattering parts. The direct scattering-part is validated with [12] and also with an exact analytical solution. In the inverse scattering-part, the objective function as well as the permittivity is computed from the known total field obtained in the direct scattering-part. The inverse scattering-part is validated with [13]. Both the direct and inverse scattering parts are also validated with the well-known "Born Approximation" in the case of the weak scatterers.

Chapter 5 describes an algorithm for finding the permittivity profile and shows the effect of various parameters on the reconstruction of the dielectric permittivity profile. In the proposed algorithm, the total electric field is computed from the known incident field. Then the reconstructed permittivity profile is computed from the surface current and the scattered field. The investigated domain is illuminated by a group of unrelated plan waves in all direction around the object to achieve better results for the reconstruction of the permittivity profile. The effect of varying the cell size on the reconstruction of the complex permittivity is studied. Multi contrasts of multi layers-inhomogeneous arbitrary shaped dielectric objects are also simulated to reconstruct the complex permittivity profile. The noise effect on the reconstruction of the complex permittivity is also considered. Multi frequency effect on the reconstruction of the complex permittivity is also taken into consideration. If the scatterer changes its position in the investigated domain, the error in the reconstruction of the complex permittivity changes with the corresponding position either in the noisy simulation or in the noise free

simulation. TE case is also investigated briefly.

Chapter 6 describes overall conclusions of the thesis and future works. Results of the numerical simulation prove the strength of the proposed algorithm by obtaining qualitative dielectric reconstruction of 2D objects.

CHAPTER-2

Literature Review

In this chapter, various numerical techniques and microwave imaging methods previously proposed by various researchers are briefly reviewed, together with a discussion of their applications, advantages and limitations.

2.1 Classification of Numerical Techniques Domain:

There are several classification schemes for numerical techniques. One criterion for classification is the domain in which the actual physical problem is defined. If the problem is defined in the time domain, then the method is described as a time domain method. In this case, the computational domain is both space and time dependent. Alternatively, the frequency domain may be chosen, leading to the frequency domain methods. In this case the computational domain is only space dependent as the problem is solved at a single frequency. The time domain formulation is suitable for studying transients or obtaining the response over a wide frequency range. The latter can be obtained using Fourier transformation of the time domain information. The frequency domain formulation is used for studying the steady state response at a single frequency. The choice of the domain is usually based on the efficiency of particular problem.

To investigate electromagnetic field problem, techniques belonging to both the frequency and time domain have been used. For most antenna application and radar

cross-section analysis, frequency domain results are usually required. For certain electromagnetic compatibility (EMC) problems, the transient response may be required.

2.2 Classification of Numerical Techniques Formulation:

The starting point in modeling electromagnetic field problems is usually Maxwell's equations, which provide the basis for studying various electromagnetic phenomena. Two kinds of mathematical formulations can be used to describe electromagnetic field problems based on the form in which Maxwell's equations are given. These are the integral equation formulation and the differential equation formulation.

2.2.1 Integral Equation Formulation Based Techniques:

The integral equation formulation can be used to solve open problems and treat complex geometries. The appropriate selection of a Green's function for the problem under consideration is the staring point for the integral equation formulation. The formulation reduces the problem into an integral equation in terms of unknown constant (such as scattered field, surface current) and these Green's functions. This usually results in a system with a dense matrix equation. Assuming a time harmonic variation, the integral equation can be formulated in the frequency domain. The method of moments (MoM) [8] and the geometrical theory of diffraction (GTD) [14] are considered the leading methods in the integral equation frequency domain formulation. The method of moments is used to discretize the integral equation thus allowing for a numerical solution for the problem at single frequency. For frequencies above the resonance range, the geometrical theory of diffraction may be used. The integral equation can also be

formulated in the time domain [15]. In such a case, it allows for study of transients in the system. A detailed review of the numerical methods based on the integral equation formulations can be found in [16].

2.2.2 Differential Equation Based Techniques:

The differential equation formulation can be used to solve closed inhomogeneous problems more easily than the integral equation formulation. Also, as the complexity of the problem increases, the differential equation based formulations become more computationally efficient than the integral equation based formulation. The numerical solution of the differential equation formulation can be obtained via such techniques as the finite difference time domain (FDTD) [17] or the transmission line matrix method (TLM) [18], both of them are time domain methods. The finite difference time domain is based simply on the application of the central finite difference in both space and time to Maxwell's equations. Both approaches lead to systems of algebraic equations that must be solved at each time step. They also require discretization of the entire simulation space in which a non-zero field distribution exists. For open region problems, they require the application of absorbing boundary conditions to truncate the simulation space to a reasonable size. Both techniques can be used an electromagnetic modeling, simulation and analysis tools. The differential equation form of Maxwell's equations can also be formulated in the frequency domain. The finite element (FE) method is widely used technique that belongs to this category [19]. Because of the type of space discretization, which is tetrahedral elements for three-dimensional problems, the method can handle a

wide range of geometry.

2.3 Microwave Imaging Techniques:

Various methods of microwave imaging proposed by various researchers in recent years are described here with their advantages and limitations. These are: the microwave tomography technique, the pseudoinverse method with equivalent current modeling, the Born and distorted Born iterative methods, a Newton iterative method, an adaptive iteration algorithm, Levenberg-Marquardt method, the conjugate gradient method, the hybrid element method, the stochastic inversion method, the maximum entropy method, the simulated annealing approach and the time domain method.

2.3.1 Microwave Tomography:

This approach is based on the Fourier diffraction projection theorem. It has been applied to cross-sectional or two-dimensional and three-dimensional imaging [20] – [24]. Conventional microwave tomography systems are based on illuminating the body by a set of plane waves. For each illumination, the forward scattered field is sampled along a straight line, for the two-dimensional case, and on a plane for three-dimensional case. Either Born or Rytov approximations are applied, thus forcing the assumption that the inhomogeneities in the body are weak scatterers. The Fourier transform of the forward scattered field gives the values of the two-dimensional Fourier transform of the object along a circular arc in the two-dimensional Fourier spectral domain. According to the Fourier diffraction project theorem, by illuminating the body from different directions and repeating the same procedure the spectral domain can be filled with samples of the

body over an ensemble of circular arcs. Using Fourier inversion, the body can be reconstructed. The main advantage of the microwave tomography is using an existing efficient numerical algorithm, which is the fast Fourier Transform (FFT). This makes the speed of the data processing fast enough to allow for real time imaging. However, microwave tomography is subject to both mathematical and experimental limitations. The mathematical limitations are imposed by Born and Rytov approximations. These approximations are fundamental to the reconstruction process and limit the range of objects that can be examined. The experimental limitations are due to the finite amount of the collected data, which in turn limits the resolution of the permittivity distribution reconstruction.

2.3.2 Pseudoinverse with Equivalent Current Modeling:

This thesis is based on this algorithm. Many researchers used this method. Its detail theoretical formulation is described in the chapter-3. The background of this method is only discussed briefly here.

Ney et al [25] was the first to propose the method of pseudoinverse transformation to microwave imaging. In this method the linearized integral equations, via equivalent current modeling, are first transformed into matrix equations using the method of Moments (MoM). The complex permittivities are then derived using the following procedure: first the equivalent current distribution is obtained from the measured scattered field; second this current distribution is used to obtain the total field. Knowing the total field and equivalent current, the object function is obtained and thus

the permittivity distribution. The first step involves the used of the pseudoinverse transformation [25]-[26] to obtain the inverse of an ill-conditioned matrix. The pseudoinverse transformation is a very powerful method in dealing with ill-conditioned matrix equations. The solution obtained is a minimum norm least square solution. Coarsi et al [27]-[31] and [13] have further developed the method and applied it to two and three-dimensional electromagnetic imaging problems. To obtain acceptable result, the method employs the use of multi-illumination together with the constraint that the number of measurement points is larger than the number of discrertized cells.

As there are no iterations involved in this method, the computation time is small compared to that of the iterative methods, which is the main advantage of the method. To improve the quality of the reconstructed image, a priori information, regarding the geometry and the dielectric properties, have been lately utilized in the reconstruction process. Yet, the filtering effect inherent in this method limits the resolution of the reconstruction especially for high noise levels in the measured scattered field.

2.3.3 Born and Distorted Born Iterative Methods:

Iterative methods with regularization in the space domain have become popular in recent years. Wang and Chew [32] proposed the Born iterative method in which the total electric field and the distribution of the electric parameters are updated by solving the direct and inverse problem separately in each iteration. The outline of the approach can be summarized as follows:

(1) The linearized inverse scattering problem is solved using the Born approximation.

(2) The scattering problem is solved for the field in the object and at the measuring points using the object function obtained in the first step.

(3) The calculated fields in step (2) are used to solve the inverse problem and obtain the next order object function.

(4) Repeat step (2) comparing the scattered field at the observation points, obtained using the reconstructed object function, with measured fields at the same observation points. When the difference is acceptable, the iteration terminates.

It should be noted that the Green's function remains unchanged during the iteration procedure (only the field in the scatterer is updated). One immediate extension of this method is to update the Green's function in each iteration together with the field in the scatterer. This is known as the distorted Born iteration method [33]. The outline of this method is almost the same as that of Born iterative method, except that in the second step an updated Green's function should be calculated using the last reconstructed permittivity distribution. Both methods have been tested with two-dimensional object only.

The results obtained using these two methods show that, for noiseless cases, the distorted Born iterative method is superior to the Born iterative method because of its faster convergent speed. While for noisy cases, the Born iterative method is more robust than the distorted Born iterative method. Also, it was shown [32] that The Born iterative method could handle electrically large scatterer with low permittivity contrast.

2.3.4 The Newton Iterative Methods:

Joachimowicz et al [33] proposed a Newton iterative method to construct the

complex dielectric permittivity distribution. In this method, the integral equations are first transformed into matrix equations using the method of Moments (MoM). Then an iterative procedure is developed as follows:

(1) Starting from an initial guess of the permittivity distribution and hence the object function, the total field inside the body is calculated.

(2) The forward scattering problem is then solved for the field at the measuring points.

(3) The error between the scattered field computed in (2) and the measured field (obtained through solving the forward scattering problem using the exact permittivity distribution) is calculated.

(4) The first order estimation of the object function error is obtained and the object function is updated using those errors.

The iterations go on until the error in the calculated scattered field is acceptable. In this procedure, step (4) involves obtaining the inverse of an ill-conditioned matrix, so standard Tikhonov regularization [34] is used to stabilize the results. Yet, the regularization factor used in this process involves a parameter that can only be determined empirically.

The main advantage of this technique is its flexibilities in considering a priori information. It provides quantitative imaging even with strong diffraction effects. However, it requires the use of a multi-illumination technique in order to obtain accurate reconstructions. Also, the required computational time is extensive.

2.3.5 An Adaptive Iteration Algorithm:

Liu et al [35], [36] proposed an adaptive algorithm that optimizes the iterative process by using, selectively, a different iterative technique for each iteration. The iterative techniques involved are the Born iterative technique and the Newton iterative technique. A decreasing ratio of error in the scattered field is used as a criterion for selecting more suitable technique for each iteration. This algorithm requires the use of multi-view illumination and Tikhonov regularization. It has been applied successfully to two-dimension objects in the presence of noise in the measured field data.

2.3.6 Levenberg-Marquardt Method:

This method has been proposed lately by Franchois et al [37] to obtain a quantitative reconstruction of the complex dielectric property distribution of biological objects. The method is a modification of the Gauss-Newton iterative method and is equivalent to the distorted Born iterative method. The method of Moment is applied to discretize the nonlinear integral equation relating the scattered field data and the complex permittivity. The resulting system of nonlinear equations is linearized in each iteration, regularized, via Tikhonov regularization, and then solved for an updating correction of the complex permittivity in the iterative procedure. The regularization parameter used can either be obtained empirically, or using a generalized cross validation (GCV) method. In fact, this method is very similar to Newton iterative method and its main modification and advantage is using the GCV method to get the regularization parameter.

The Levenberg-Marquardt method requires the use of the multi-view illumination and

imposes a priori bounds on the complex permittivity in order to accelerate the convergence. The method has only been applied to two-dimensional objects immersed in water. The use of the regularized cross validation method for choosing the regularization parameter has proven to be successful in the case of weak homogeneous scatterers and strong homogeneous scattterers with an initial guess in the neighborhood of the solution. For strong scattering inhomogeneities, the reconstruction is of lesser quality.

2.3.7 Conjugate Gradient Method:

The conjugate gradient method was discussed in [38] as a tool to handle ill-posed matrix equations resulting from the method of moments. This iterative method is similar to the steepest descent method that involves the search for the minimum of a function in a direction suggested by its negative gradient. It starts with an initial guess that generates the first residual vector and the direction vector. Then, the system is solved iteratively. The conjugate gradient method has the advantage of having a rate of convergence practically insensitive to the initial guess, although a good initial guess reduces the number of iterations. The method has been applied to two and three-dimensional microwave imaging problems [38]-[39], and good reconstruction were obtained.

2.3.8 The Hybrid Element Method:

Meaney et al [40] proposed this method for two-dimensional image reconstruction problems. The used computational methodology is a hybrid coupling of the finite element and the boundary element methods. In calculating the electric fields from the current estimates of the electrical properties, it seeks to take advantage of the strong points of the

finite element method in the regions where the electrical properties are inhomogeneous or not known. It also utilizes the strengths of the boundary element method in the region where the medium is homogeneous, unbounded in nature and the electrical properties are known. Coupling of these two methods occurs only at the boundary of the inhomogeneous dielectric object. The method employs a Newton iterative procedure together with multi-view excitation for image reconstruction. The reconstruction technique is very similar to that used by Jaochimowich et al [33]. The regularization employed is a blending of both Tikhonov and Marquardt approaches with regularization coefficients being determined empirically. One of the advantages of this method is the ability to use non-uniform meshing to handle available a priori information. The results obtained show that it operates best for smaller objects with low contrast. For the case of large objects and, or steep gradients, the method provides only qualitative images.

2.3.9 Stochastic Inversion Method:

The stochastic treatment of ill-posed problems has been successfully used in image processing and recognition techniques and seismology studies. Qin et al [41] applied the stochastic inversion of matrices to microwave imaging of two-dimensional dielectric bodies. The method requires an initial accurate guess, as inappropriate guesses can cause the algorithm to be slowly convergent or even divergent. The reconstruction process can be summarized in the following steps:

The linearized integral equation is discretized using the method of Moments.

The next step is to use the Tikhonov regularization to solve the inverse problem,

the solution obtained is used as a priori data.

Finally, using this a priori data, the stochastic inverse is applied to compute the equivalent current distribution within the body and hence the complex permittivity distribution.

The main advantage of this method is that it requires less computation time compared to other iterative techniques. Also, various criteria for choosing the regularization parameter [42]-[43] were proposed. Single-view illumination yields accurate reconstruction only for simple objects with very small inhomogeneities. As the number of inhomogeneities increases, this requires the use of multi-view illumination.

2.3.10 The Maximum Entropy Method:

Baribuad [44] applied the maximum entropy method to two-dimensional microwave imaging problems. The method, which belongs to stochastic techniques, is based on the information theory approach. It demands that one chooses from the available data the solution, which uses the maximum information from the available data. In this method, the method of moments is used to discretized the integral field equation. The entropy is defined in terms of the current density distribution. The aim of the method is to maximize the difference between the entropy and the Gaussian and excess noise. The problem of maximization has no explicit solution and has to be solved iteratively. The image obtained using this method uses more of the available data and is a regularized solution. Also, the effect of the noise can be easily included in this method. Yet, the main drawback is that although the method has only been applied to simple two-dimensional

dielectric scatterer, the computational time needed is very long.

2.3.11 Simulated Annealing Approach:

This approach is based on stochastic techniques to search for the optimum state of a system and to avoid iterative processes being trapped to a local minimum. The usage of simulated annealing technique can bypass the need to invert large matrices and enables one to obtain the solution using an iterative procedure. This approach has only been applied to simple two-dimensional problems [45]-[46] and its main disadvantage is the large computational time involved.

2.3.12 Time Domain Methods:

Moghaddam and Chew [32] proposed a method to solve a two-dimensional problem in time domain. In their method, the time domain problem is transformed by using Fourier transformation. The integral equation obtained in the time domain is transformed into a set of integral equations in the spatial domain with different frequencies and then solved using a Born iterative technique. In the computation, the dielectric distribution is assumed to be independent of frequency.

Batrakov et al [47] proposed an algorithm based on the Newton-Kantorovich iterative procedure and Tikhonov regularization for solving two-dimensional inverse problems in the time domain. In their algorithm, most of calculations are given in an explicit form, thus reducing the computational time and making the algorithm suitable for real time process. Yet, their analysis is restricted to cylindrical objects with permittivity varying in the radial direction only. Later, they expanded their work [48] to handle

objects with arbitrary complex permittivity distributions. In doing so, they introduced complexity to the calculations compared to their earlier work.

The advantage of the time domain methods is that more information is available. However, the computational cost is huge compared to spatial domain methods because the fields or their spectrum have to be calculated at different times.

CHAPTER-3

Formulation of Direct and Inverse Scattering Problems

3.1 Introduction:

In this chapter, the mathematical formulation of integral equation for electromagnetic scattering is described for TM and TE cases. Either TM or TE case has two parts: a direct and inverse scattering part. The scattering field is formulated in the direct scattering part. The permittivity profile is computed from the inverse scattering part. The mathematical formulation for Born approximation method is also briefly described.

3.2 Transverse Magnetic (TM) case:

3.2.1 Direct Scattering Formulation:

Let us consider a harmonic EM plane wave incident in free space on a dielectric cylinder of arbitrary cross section as shown in Fig. 3.1. The time harmonic $e^{j\omega t}$ is understood. It is assumed that the incident electric field intensity $\vec{E}^i$ has only a z component independent of z, where the z-axis is parallel with the cylinder axis. S is the investigated area in a plane orthogonal to Z. The incident electric field may be written as:

$$\vec{E}^i = \hat{z}E^i(x,y) = \hat{z}E_0 e^{-jk_0' \cdot r} = \hat{z}E_0 e^{jk_0'(x\cos\phi_i + y\sin\phi_i)} \tag{3.1}$$

Where ϕ_i is the angle of incidence measured from x-axis of the coordinate system.

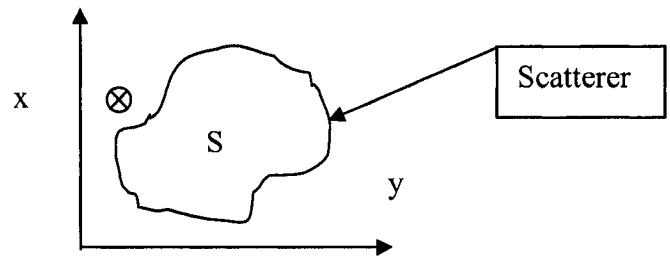

Fig.3.1 Cross section of a dielectric object with the coordinate system

The dielectric cylinder is assumed to have the same permeability as free-space ($\mu = \mu_0$). The dielectric material is assumed to be linear and isotropic, but it may be inhomogeneous with respect to the transverse coordinates as follows:

$$\tilde{\varepsilon} = \varepsilon(x,y) = \varepsilon_0 \varepsilon_r(x,y) - j\frac{\sigma(x,y)}{\omega} \tag{3.2}$$

$$\Rightarrow \varepsilon(x,y)/\varepsilon_0 = \varepsilon_r(x,y) - j\frac{\sigma(x,y)}{\omega\varepsilon_0} \tag{3.2.a}$$

Where $\tilde{\varepsilon}$ represents the complex permittivity and ω represents the angular frequency $2\pi f$.

Under this assumption, the total electric field vector and the scattered electric field vector are parallel to and uniform along the cylinder axis. Therefore, the vectorial problem is transformed into a scalar one. The following scalar Helmholtz equations hold:

$$\left[\nabla^2 + \gamma_s^2(x,y)\right]\vec{E}(x,y) = 0 \qquad (x,y) \in S \tag{3.3.a}$$

$$\left[\nabla^2 + k_0^2(x,y)\right]\vec{E}(x,y) = 0 \qquad (x,y) \notin S \tag{3.3.b}$$

where $\gamma_s = \omega\sqrt{\mu_0 \tilde{\varepsilon}(x,y)}$

Let $\vec{E}$ represents the total field; i.e, the field set up by the source in the presence of the dielectric cylinder. The scattered field is defined to be the difference between the total and incident fields. Thus,

$$\vec{E} = \vec{E}^i + \vec{E}^s \tag{3.3.c}$$

The scattered field $\vec{E}^s$ may be generated by an equivalent electric current $\vec{J}$ that is induced in the dielectric body. This field is radiating in unbounded free space, where

$$\vec{J}(x,y) = j\omega(\varepsilon - \varepsilon_0)\vec{E} = j\omega\varepsilon_0(\varepsilon_r - 1)\vec{E} = \frac{j}{\omega\mu_0}\left[\gamma_s^2 - k_0^2\right]\vec{E} = [O(x,y)]\vec{E} \tag{3.4}$$

where, $\gamma_s^2 = \omega^2\mu_0\varepsilon_0\varepsilon_r(x,y) - j\omega\mu_0\sigma(x,y)$ *and* $k_0 = \omega\sqrt{\mu_0\varepsilon_0} = 2\pi/\lambda_0$. The free-space wavelength is given by λ_0. O (x,y) is called the objective function. This equivalent current density is often called the "polarization current". The electric field due to an electric current filament dI parallel with the z-axis in free space is given by,

$$d\vec{E}^s = -\hat{z}(\omega\mu/4)H_0^{(2)}(k_0\rho)dI \tag{3.5}$$

Where $H_0^{(2)}(k_0\rho)$ is the Hankel function of order zero, ρ is the distance from the current filament to the observation point. The increment of electric current, which generates the scattered field, is given by,

$$d\vec{I} = \vec{J}ds = j\omega(\varepsilon - \varepsilon_0)\vec{E}ds \tag{3.6}$$

Where 'ds' is the increment of surface area on the cross section of the dielectric cylinder. From (3.5) and (3.6), the scattered field is given by

$$\vec{E}^s(x,y) = -(jk_0^2/4)\iint(\varepsilon_r - 1)\vec{E}(x',y')H_0^{(2)}(k_0\rho)dx'dy'$$

$$= -(jk_0^2/4)\iint\frac{\vec{J}(x',y')}{j\omega\varepsilon_0}H_0^{(2)}(k_0\rho)dx'dy' \qquad (3.7)$$

where (x, y) and (x', y') are the coordinates of the observation point and the source point, respectively, ε_r is the complex relative dielectric constant ($\varepsilon_r = \varepsilon/\varepsilon_0$) and

$$\rho = \sqrt{(x-x')^2 + (y-y')^2} \qquad (3.8)$$

The integration in (3.7) is to be performed over the cross section of the dielectric cylinder. In the inhomogeneous case, the relative dielectric constant is considered to be a function of the source coordinates $\varepsilon_r = \varepsilon_r(x', y')$. Equation (3.7) is valid for the scattered field at any point inside or outside the dielectric region. The integral equation for the total field $\vec{E}$ is obtained from (3.3.c) and (3.7) in the following form:

$$\vec{E}(x,y) + (jk_0^2/4)\iint(\varepsilon_r - 1)\vec{E}(x',y')H_0^{(2)}(k_0\rho)dx'dy'$$

$$= \vec{E}(x,y) + \frac{\omega\mu_0}{4}\iint\vec{J}(x',y')H_0^{(2)}(k_0\rho)dx'dy' = \vec{E}^i(x,y) \qquad (3.9)$$

Let us divide the cross section of the dielectric cylinder into small cells so that the dielectric constant and the electric field intensity are essentially constant over each cell. The division into cells is indicated in Fig.3.2.

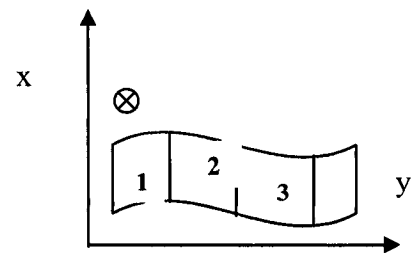

Fig.3.2: The cross section of the dielectric cylinder is divided into small cells

If (3.9) & (3.7) is enforced at the center of cell m, the following expression is obtained

$$\vec{E}_m + (jk_0^{\,2}/4)\sum_{n=1}^{N}(\varepsilon_n - 1)\vec{E}_n \iint_{cell\,n} H_0^{(2)}(k_0\rho_{mn})dx'dy' = \vec{E}_m^{\,i} \tag{3.10}$$

$$(-jk_0^{\,2}/4)\sum_{n=1}^{N}(\varepsilon_n - 1)\vec{E}_n \iint_{cell\,n} H_0^{(2)}(k_0\rho_{mn})dx'dy' = -\frac{\omega\mu_0}{4}\sum_{n=1}^{N}\vec{J}_n(x',y')\iint_{cell-n} H_0^{(2)}(k_0\rho_{mn})dx'dy' = \vec{E}_m^{\,s} \tag{3.11}$$

Where ε_n, $\vec{J}_n$ and $\vec{E}_n$ represent the complex dielectric constant, surface current and the total electric field intensity at the center of cell n, respectively, and

$$\rho = \sqrt{(x'-x_m)^2 + (y'-y_m)^2} \tag{3.12}$$

By taking m = 1,2,3...N, equation (3.10) yields a system of N linear equations, where N represents the total number of cells. These can be solved to determine the total electric field intensity at the center of each cell $(\vec{E}_1, \vec{E}_2, \vec{E}_3, ..., \vec{E}_N)$. Having thus determined the total field $\vec{E}(x,y)$ in the dielectric region, it is then possible to calculate the scattered field of the dielectric cylinder at any point in the space by means of (3.11). The details of the solution are described in the following section.

3.2.1.1 Formulation of the matrix equation:

The integration of (3.10) & (3.11) can be avoided using Dirac delta for both the basis and testing functions [9]. A simple solution is available for the integral of the zero-order Hankel function over a circular region. So, the discretized square cell can be

replaced by a circular cell as shown in Fig.3.3.

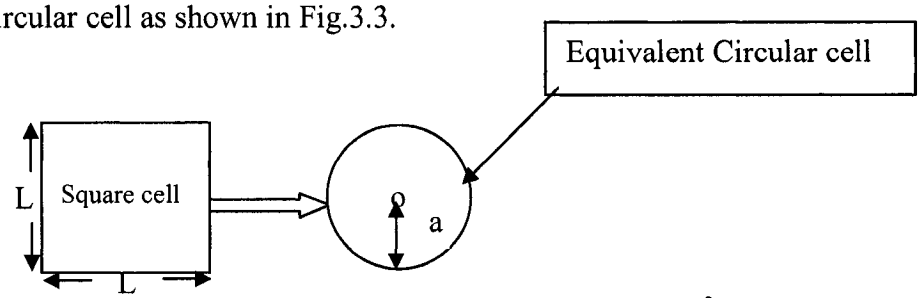

For Hangkel function, L x L = πa^2

Fig.3.3 Discretized square cell is converted into small circle having equal area

The simple solution of Hankel function is given by

$$\int_0^{2\pi}{}_{cell\ n}\int_0^{a} H_0^{(2)}(k_0\rho)\rho' d\rho' d\varphi'$$

$$= (2/k_0^2)[\pi k_0 a H_1^{(2)}(k_0 a) - 2j] \quad if \quad m = n \qquad (3.13.a)$$

$$= (2a\pi/k_0)J_1(k_0 a)H_0^{(2)}(k_0\rho_{mn}) \quad if \quad m \neq n \qquad (3.13.b)$$

A small error is incurred in approximating square cells with circular cells with same cross section area to take an advantage of the simple expressions given in (3.13) .The distance between the centers of the mth and nth cells is given by

$$\rho_{mn} = \sqrt{(x_m - x_n)^2 + (y_m - y_n)^2} \qquad (3.14)$$

(3.10) can be written in the following form:

$$\vec{E}_m + \sum_{n=1}^{N}(\varepsilon_n - 1)\vec{E}_n\left(j/2\right)\left[\pi k_0 a \mathrm{H}_1^{(2)}\left(k_0 a\right) - 2j\right] = \vec{E}_m^{\,i} \quad if \quad m = n \qquad (3.10.a)$$

$$\sum_{n=1}^{N}(\varepsilon_n - 1)\vec{E}_n\left(j\pi k_0 a/2\right)J_1\left(k_0 a\right)\mathrm{H}_0^{(2)}\left(k_0\rho_{mn}\right) = \vec{E}_m^{\,i} \quad if \quad m \neq n \qquad (3.10.b)$$

The above two expressions are written in the general form:

$$\sum_{n=1}^{N} C_{mn}\vec{E}_n = \vec{E}_m{}^i \qquad \text{where m = 1,2,3,4...N} \tag{3.15}$$

Details derivation of equation (3.15) and all relevant terms are given in appendix A.

If a_n represents the radius of the equivalent nth circular cell, the coefficients C_{mn} are given by,

$$C_{mn} = 1 + (\varepsilon_m - 1)(\frac{j}{2})\left[\pi k_0 a_m \mathrm{H}_1^{(2)}(k_0 a_m) - 2j\right] \quad \text{if } n = m \tag{3.15.a}$$

$$C_{mn} = (\varepsilon_n - 1)(j\pi k_0 a_n / 2) J_1(k_0 a_n) H_0{}^{(2)}(k_0 \rho_{mn}) \quad \text{if } n \neq m \tag{3.15.b}$$

(3.15) can be represented in a matrix form:

$$[C]\ [\vec{E}] = [\vec{E}^i] \tag{3.16.a}$$

$$[\vec{E}] = -[C]^{-1}[\vec{E}^i] \tag{3.16.b}$$

Where,

$$[C] = \begin{bmatrix} C_{11} & . & . & C_{1N} \\ . & . & . & . \\ . & . & . & . \\ C_{M1} & . & . & C_{MN} \end{bmatrix}, \qquad [\vec{E}] = \begin{bmatrix} \vec{E}(x_{c1}, y_{c1}) \\ . \\ \vec{E}(x_{cn}, y_{cn}) \\ . \\ \vec{E}(x_{cN}, y_{cN}) \end{bmatrix} \quad \text{and} \quad [\vec{E}^i] = \begin{bmatrix} \vec{E}^i(x_1, y_1) \\ . \\ \vec{E}^i(x_m, y_m) \\ . \\ \vec{E}^i(x_M, y_M) \end{bmatrix}.$$

The scattered field can be found out using (3.16.b) and (3.3.c). Similarly, the system of linear equations represented by (3.11) can be written in the following form:

$$\sum_{n=1}^{N} D_{mn}\vec{J}_n = \vec{E}_m^{\,s} \quad \text{with m=1,2,3,4.....N} \tag{3.17}$$

Details derivation of (3.17) are given in appendix B. The coefficients D_{mn} are given by,

$$D_{mn} = -(\pi\eta_0 a_n / 2) J_1(k_0 a_n) H_0^{(2)}(k_0 \rho_{mn}) \quad \text{if m}\neq\text{n} \qquad (3.18.a)$$

$$D_{mn} = -(\frac{1}{2\omega\varepsilon_0})\left[\pi k_0 a_m \mathrm{H}_1^{(2)}(k_0 a_m) - 2j\right] \quad \text{if m=n} \qquad (3.18.b)$$

In a matrix form,

$$[D]\ [\vec{J}] = [\vec{E}^s] \qquad (3.19.a)$$

$$[\vec{J}] = -[D]^{-1}[\vec{E}^s] \qquad (3.19.b)$$

Where,

$$[D] = \begin{bmatrix} D_{11} & \cdots & D_{1N} \\ \vdots & \cdots & \vdots \\ D_{M1} & \cdots & D_{MN} \end{bmatrix}, \quad [\vec{J}] = \begin{bmatrix} \vec{J}(x_{c1}, y_{c1}) \\ \vdots \\ \vec{J}(x_{cn}, y_{cn}) \\ \vdots \\ \vec{J}(x_{cN}, y_{cN}) \end{bmatrix} \quad \textit{and} \quad [\vec{E}^s] = \begin{bmatrix} \vec{E}^s(x_1, y_1) \\ \vdots \\ \vec{E}^s(x_m, y_m) \\ \vdots \\ \vec{E}^s(x_M, y_M) \end{bmatrix}.$$

We can then find out the equivalent surface current from the corresponding scattered field using (3.19.b).

3.2.2 Inverse Scattering:

In this section, the procedure to reconstruct the complex permittivity profile of a cylindrical object is outlined. Assuming that the scattered field is known, either through measurements or analysis, one can discretize (3.4) and re-write in the matrix form:

$$[\vec{J}] = [O]\ [\vec{E}] \qquad (3.20.a)$$

$$[O]=[\vec{J}]\ [\vec{E}]^{-1} \tag{3.20.b}$$

where,

$$[O]=\begin{bmatrix} O_{11} & . & . & 0 \\ . & . & . & . \\ . & . & . & . \\ 0 & . & . & O_{MN} \end{bmatrix},\quad [\vec{J}]=\begin{bmatrix} \vec{J}(x_{c1},y_{c1}) \\ . \\ \vec{J}(x_{cn},y_{cn}) \\ . \\ \vec{J}(x_{cN},y_{cN}) \end{bmatrix}\quad and\quad [\vec{E}\ ]=\begin{bmatrix} \vec{E}\ (x_{c1},y_{c1}) \\ . \\ \vec{E}\ (x_{cn},y_{cn}) \\ . \\ \vec{E}\ (x_{cN},y_{cN}) \end{bmatrix}.$$

[O] represents a diagonal matrix whose nontrivial elements, according to (3.4), are given by

$$O_{nn} = O\ (x_{cn}, y_{cn}) = \frac{j}{\omega\mu_0}\left[\gamma_s^2(x_{cn},y_{cn}) - k_0^2\right],\ n = 1,2,3\ldots N. \tag{3.21}$$

At this point, the dielectric parameters of any cell can be obtained using (3.22)

$$Onn = \frac{\vec{J}(x_{cn},y_{cn})}{\vec{E}(x_{cn},y_{cn})},\qquad n = 1,2,3,\ldots\ldots\ldots\ldots,N \tag{3.22}$$

In the above relation, $\vec{E}$ and $\vec{J}$ can be solved by means of the pseudoinverse algorithm from (3.16.b) and (3.19.b) respectively, which allows one to obtain, in a straightforward way, the values of the dielectric characteristics for any sub-area of the region of interest.

The dielectric parameter can be written in the following form:

$$\begin{aligned} O(x_{cn},y_{cn}) &= \frac{j}{\omega\mu_0}\left[\gamma_s^2(x_{cn},y_{cn}) - k_0^2\right] \\ &= \frac{j}{\omega\mu_0}[\omega^2\mu_0\varepsilon_0\varepsilon_r(x_{cn},y_{cn}) - j\omega\mu_0\sigma(x_{cn},y_{cn}) - \omega^2\mu_0\varepsilon_0] \\ &= -j[\omega\ \varepsilon_0\varepsilon_r(x_{cn},y_{cn}) - j\sigma(x_{cn},y_{cn}) - \omega\ \varepsilon_0] \end{aligned} \tag{3.23}$$

If the dielectric is lossless then $\sigma(x_{cn},y_{cn}) = 0$ and (3.23) can re-written in the following:

$$O(x_{cn}, y_{cn}) = -j[\omega\ \varepsilon_0 \varepsilon_r(x_{cn}, y_{cn}) - \omega\ \varepsilon_0] \tag{3.24}$$

For a lossless dielectric, one can get the permittivity profile in the following:

$$\varepsilon_r(x_{cn}, y_{cn}) = 1 + j\frac{O(x_{cn}, y_{cn})}{\omega\ \varepsilon_0} \tag{3.24.a}$$

If the dielectric is lossy, then the dielectric permittivity is complex.

For lossy dielectric, the permittivity profile can be written in the following:

$$\varepsilon_r(x_{cn}, y_{cn}) - \frac{j\sigma(x_{cn}, y_{cn})}{\omega\varepsilon_0} = 1 + j\frac{O(x_{cn}, y_{cn})}{\omega\ \varepsilon_0} \tag{3.24.b}$$

$$\varepsilon_r(x_{cn}, y_{cn}) = \mathrm{Re}[\varepsilon\ / \varepsilon_0] = \mathrm{Re}\left[1 + j\frac{O(x_{cn}, y_{cn})}{\omega\ \varepsilon_0}\right] \tag{3.25.a}$$

$$\sigma(x_{cn}, y_{cn}) = \mathrm{Im}\left[1 + j\frac{O(x_{cn}, y_{cn})}{\omega\ \varepsilon_0}\right] \tag{3.25.b}$$

Note that if both $J(x_{cn}, y_{cn})$ and $E(x_{cn}, y_{cn})$ are too small, consequently *Onn* becomes inaccurate.

3.2.3 Integral Equation with Born Approximation:

In this section, the formulation of the integral equation for Born approximation method is outlined in order to measure the strength of Pseudoinverse algorithm. The Born approximation is a widely accepted approximation for weak scatrterers and usually applied in microwave tomography. For low contrast inhomogeneous scatterers, the magnitude of the transmitted field in the object is very small compared to that of the incident field. Thus the transmitted field inside the object can be neglected and the total

field can be approximated by the incident field. Based on this approximation, the scattered field (3.7) can be written as:

$$\vec{E}^s(x,y) = \int G(x,y,x',y')O(x',y')\vec{E}^i(x',y')dx'dy'$$
$$= -\frac{\omega\mu_0}{4}\iint O(x',y')\vec{E}^i(x',y')H_0^2(k_0\rho)dx'dy' \qquad (3.26)$$

If (3.26) is enforced at the center of cell m and discretized by moment method along with Galerkin's method using the available solution of integral of the zero-order Hankel function over circular region, (3.26) can be expressed in a matrix form. If a_n represents the radius of the equivalent nth circular cell and for m=1,2,3...N then,

$$\sum_{n=1}^{N}\frac{-j}{2}(\varepsilon_m - 1)\left[\pi k_0 a_m \mathrm{H}_1^2(k_0 a_m) - 2j\right]\vec{E}_m^i = \vec{E}_m^{\,s} \quad if \quad m = n \qquad (3.27.a)$$

$$\sum_{n=1}^{N}(\varepsilon_n - 1)\frac{-j\pi k_0 a_n}{2}J_1(k_0 a_n)\mathrm{H}_0^{(2)}(k_0\rho_{mn})\vec{E}_n^i = \vec{E}_m^{\,s} \quad if \quad m \neq n \qquad (3.27.b)$$

The above expressions are written in general form like appendix A:

$$\sum_{n=1}^{N} D_{mn}^b \vec{E}_n^i = \vec{E}_m^{\,s} \quad \text{with m = 1, 2, 3... N,} \qquad (3.28)$$

The coefficients D_{mn}^b are given by,

$$D_{mn}^b = (\varepsilon_m - 1)\left(\frac{-j}{2}\right)\left[\pi k_0 a_m \mathrm{H}_1^{(2)}(k_0 a_m) - 2j\right] \quad if \ n = m \qquad (3.29.a)$$

$$D_{mn}^b = (\varepsilon_n - 1)(-j\pi k_0 a_n / 2)J_1(k_0 a_n)H_0^{(2)}(k_0\rho_{mn}) \ if \ n \neq m \qquad (3.29.b)$$

In matrix form,

$$[D^b]\ [\vec{E}^i] = [\vec{E}^s] \qquad (3.30)$$

Where $D^b = D_{mm}{}^b + D_{mn}{}^b$

3.2.4 Ill-posed Problems of the algorithm:

The integral equation for nonlinear inverse-scattering problem of the proposed method has been discretized by the method of moment and has been resulted an ill condition matrix of the integral equation. A pseudoinversion algorithm has been applied to address the problems related to the system's ill condition. In this section, the general characteristic of a well-posed problem is described briefly and also explained at a glance how to overcome the ill-posed problem of the microwave imaging. Usually, many problems of mathematical physics can be formulated in terms of an operator equation

$$Ax = y \tag{3.31}$$

Generally, y denotes the system output, x denotes the unknown being sought and A is the system operator. Given A and y, the objective is to determine x. According to the Hadamard definitions [51], the problem is well posed if the following conditions are satisfied:

1) For each element y, there is solution x: That is the *existence* condition.
2) The solution x is unique for a given y: that is the *uniqueness* condition.
3) For small perturbations in y, there are small perturbations in x: that is the *stability* condition.

The problem is said to be ill-posed if at lest one of the above conditions is violated. There are three main reasons that cause this ill-posedness, namely, incompleteness of the input data, numerical errors in the input data and /or the nature of

the system operator A. In order to solve an ill-posed problem, special techniques have to be employed to regularize the problem [52]. The solution to the regularized problem will be well-behaved and will offer a reasonable approximation to the solution of the ill-posed problem. In particular, an ill-posed problem may be regularized by:

a) Changing the definition of what is meant by an acceptable solution,

b) Changing the space to which the acceptable solution belongs,

c) Revising the problem statement,

d) Introducing regularization operator and

e) Using statistical techniques.

3.3 Transverse Electric (TE) case:

3.3.1 Direct and Inverse Scattering Formulation:

Consider a harmonic wave incident in free space on a dielectric cylinder of arbitrary cross-section shape as indicated in Fig.3.4. For TE^z case, the incident electric field intensity E^i has no z component and it may be written as:

$$\vec{E}^i = \hat{x}E_x^i(x,y) + \hat{y}E_y^i(x,y) = E_0(\hat{y}\cos\phi_i - \hat{x}\sin\phi_i)e^{jk_0'(x\cos\phi_i + y\sin\phi_i)} \qquad (3.32)$$

Where $\hat{x}$ and $\hat{y}$ represent unit vectors parallel with the x and y-axis and ϕ_i is the angle of incidence with x-axis of the coordinate system. Similarly, The total field, Scattered field and the electric current have x and y component. The total field ($\vec{E}$) is generated by the source ($\vec{E}^i$) in presence of the dielectric object and it can be written in the following:

$$\vec{E} = \hat{x}E_x(x,y) + \hat{y}E_y(x,y) = \vec{E}^i + \vec{E}^s = \hat{x}[E_x^i + E_x^s] + \hat{y}[E_y^i + E_y^s] \qquad (3.33)$$

The equivalent electric current ($\vec{J}$) is induced due to incident field ($\vec{E}^i$) in the dielectric object. The equivalent electric current is given by,

$$\vec{J} = \hat{x}J_x(x,y) + \hat{y}J_y(x,y) = j\omega(\varepsilon - \varepsilon_0)[\hat{x}E_x(x,y) + \hat{y}E_y(x,y)] \qquad (3.34)$$

The field due to an electric current filament dI in free space is given by,

$$d\vec{E}^s = -(\hat{x} + \hat{y})\frac{\omega\mu}{4}H_0^{(2)}(k_0\rho)dI \qquad (3.35)$$

Where ρ is the distance from the current filament to the observation point.

The increment of electric current which generate the scattered field is given by,

$$d\vec{I} = j\omega(\varepsilon - \varepsilon_0)[\hat{x}E_x(x,y) + \hat{y}E_y(x,y)]ds \qquad (3.36)$$

Where ds is the increment of the surface area on the cross section of the dielectric object.

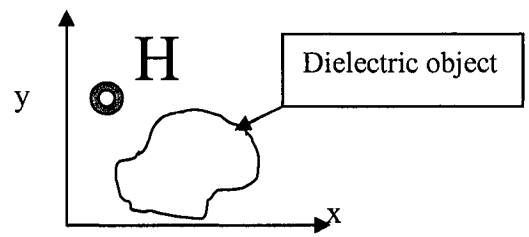

Fig.3.4 The Cross-section of a dielectric object

From (3.35) and (3.36), one can find out the scattered field by integration over cross sectional area. The integral equation of the scattered field is enforced at the center of cell and discretized by moment method along with Galerkin's method using the available solution of integral of the zero-order Hankel function over circular region like TM case (section-3.2.1.1). If harmonic electric current densities J_x and J_y are distributed uniformly in circular cylinder of radius "a", these currents generate a field in free space. The

scattered field due to a single cell n from one circular cell centered at the origin with the observation point located outside the cell is given by,

$$E_x^s(x,y) = K\begin{Bmatrix}\left[k_0\rho y^2 H^{(2)}{}_0(k_0\rho) + (x^2 - y^2)H^{(2)}{}_1(k_0\rho)\right]J_x \\ + xy[2H^{(2)}{}_1(k_0\rho) - k_0\rho H^{(2)}{}_0(k_0\rho)]J_y\end{Bmatrix} \tag{3.37}$$

$$E_y^s(x,y) = K\begin{Bmatrix}\left[k_0\rho x^2 H^{(2)}{}_0(k_0\rho) + (y^2 - x^2)H^{(2)}{}_1(k_0\rho)\right]J_y \\ + xy[2H^{(2)}{}_1(k_0\rho) - k_0\rho H^{(2)}{}_0(k_0\rho)]J_x\end{Bmatrix} \tag{3.38}$$

$$\text{K= -} \quad \frac{\pi a J_1(k_0 a)}{2\omega\varepsilon_0\rho^3} \tag{3.39}$$

The scattered field of the entire cylinder is, according to the superposition theorem, given by a summation of such terms with x and y replaced by $(x - x_n)$ and $(y - y_n)$ in (3.37) and (3.38) where x_n and y_n denote the coordinates of the center of cell n. If (3.33) is enforced at the center of cell m, we obtain two scalar equations for entire cylinder in the following:

$$E_{xm} + \frac{\pi}{2\omega\varepsilon_0}\sum_{n=1}^{N}\frac{a_n J_1(k_0 a_n)}{\rho_{mn}^3}\begin{Bmatrix}\left[k_0\rho_{mn}(y_m - y_n)^2 H^{(2)}{}_0(k_0\rho_{mn}) + \right. \\ \left.((x_m - x_n)^2 - (y_m - y_n)^2)H^{(2)}{}_1(k_0\rho_{mn})\right]J_x \\ + (x_m - x_n)(y_m - y_n)[2H^{(2)}{}_1(k_0\rho_{mn}) - \\ k_0\rho_{mn}H^{(2)}{}_0(k_0\rho_{mn})]J_y\end{Bmatrix} = E_{xm}^i \tag{3.40}$$

$$E_{ym} + \frac{\pi}{2\omega\varepsilon_0}\sum_{n=1}^{N}\frac{a_n J_1(k_0 a_n)}{\rho_{mn}^3}\begin{Bmatrix}\left[k_0\rho_{mn}(x_m - x_n)^2 H^{(2)}{}_0(k_0\rho_{mn}) + \right. \\ \left.((y_m - y_n)^2 - (x_m - x_n)^2)H^{(2)}{}_1(k_0\rho_{mn})\right]J_y \\ + (x_m - x_n)(y_m - y_n)[2H^{(2)}{}_1(k_0\rho_{mn}) - \\ k_0\rho_{mn}H^{(2)}{}_0(k_0\rho_{mn})]J_x\end{Bmatrix} = E_{ym}^i \tag{3.41}$$

With m=1,2,3...N and $\rho_{mn} = \sqrt{(y_m - y_n)^2 + (x_m - x_n)^2}$.

Equations (3.33), (3.34), (3.40) and (3.41) can be combined to obtain two linear relations among the total fields in the various cells (similar to appendix A):

$$\sum_{n=1}^{N}(A_{mn}E_{xn} + B_{mn}E_{yn}) = E_{xm}^{i} \tag{3.42}$$

$$\sum_{n=1}^{N}(C_{mn}E_{xn} + D_{mn}E_{yn}) = E_{ym}^{i} \tag{3.43}$$

where Off diagonal element of coefficient of the above matrix,

$$A_{mn} = K'[k_0\rho_{mn}(y_m - y_n)^2 H_0^{(2)}(k_0\rho_{mn}) + \{(x_m - x_n)^2 - (y_m - y_n)^2\}H_1^{(2)}(k_0\rho_{mn})]$$

$$B_{mn} = C_{mn} = K'(y_m - y_n)(x_m - x_n)[2H_1^{(2)}(k_0\rho_{mn}) - k_0\rho H_0^{(2)}(k_0\rho_{mn})]$$

$$D_{mn} = K'[k_0\rho_{mn}(x_m - x_n)^2 H_0^{(2)}(k_0\rho_{mn}) + \{(y_m - y_n)^2 - (x_m - x_n)^2\}H_1^{(2)}(k_0\rho_{mn})]$$

$$K' = \frac{j\pi a_n J_1(k_0 a_n)(\varepsilon_n - 1)}{2\rho_{mn}^{\ 3}}$$

The diagonal elements are found putting x = 0 and y = 0 in (3.37) and (3.38).

$$A_{mm} = D_{mm} = 1 + (\varepsilon_m - 1)[0.25j\pi k_0 a_m H_1^{(2)}(k_0 a_m) + 1]$$

$$B_{mm} = C_{mm} = 0$$

N represents the total number of cells and a_n represents the radius of the circular cell n.

From equation (3.42) & (3.43), the following matrix can be written:

$$\begin{bmatrix} E^i_{x1} \\ E^i_{x2} \\ . \\ . \\ . \\ E^i_{xN} \\ E^i_{y1} \\ E^i_{y2} \\ . \\ . \\ . \\ E^i_{yN} \end{bmatrix} = \begin{bmatrix} A_{11} & A_{12} & . & . & . & A_{1N} & B_{11} & B_{12} & . & . & . & B_{1N} \\ A_{21} & A_{22} & . & . & . & A_{2N} & B_{21} & B_{22} & . & . & . & B_{2N} \\ . & . & . & . & . & . & . & . & . & . & . & . \\ . & . & . & . & . & . & . & . & . & . & . & . \\ . & . & . & . & . & . & . & . & . & . & . & . \\ A_{N1} & A_{N2} & . & . & . & A_{NN} & B_{N1} & B_{N2} & . & . & . & B_{NN} \\ C_{11} & C_{12} & . & . & . & C_{1N} & D_{11} & D_{12} & . & . & . & D_{1N} \\ C_{21} & C_{22} & . & . & . & C_{2N} & D_{21} & D_{22} & . & . & . & D_{2N} \\ . & . & . & . & . & . & . & . & . & . & . & . \\ . & . & . & . & . & . & . & . & . & . & . & . \\ . & . & . & . & . & . & . & . & . & . & . & . \\ C_{N1} & C_{N2} & . & . & . & C_{NN} & D_{N1} & D_{N2} & . & . & . & D_{NN} \end{bmatrix} \begin{bmatrix} E_{x1} \\ E_{x2} \\ . \\ . \\ . \\ E_{xN} \\ E_{y1} \\ E_{y2} \\ . \\ . \\ . \\ E_{yN} \end{bmatrix}$$

Equations (3.42) and (3.43) represent a system of 2N linear equations.

CHAPTER - 4

Validation and Accuracy Analysis

4.1 Introduction:

In this chapter, the numerical simulation for various geometrical dielectric objects is validated with some journals and well-established Born Approximation due to measure the strength of the proposed algorithm. The following formulas are used:

$$\% \text{ Error of permittivity for nth cell, } \Delta_{\varepsilon_n} = \frac{\varepsilon_{rn}(x_{cn}, y_{cn}) - \varepsilon_{rn}'(x_{cn}, y_{cn})}{\varepsilon_{rn}(x_{cn}, y_{cn})} x \ 100 \quad (4.1)$$

$$\% \text{ Error of permittivity for nth cell, } \Delta_{\sigma_n} = \frac{\sigma_n(x_{cn}, y_{cn}) - \sigma_n'(x_{cn}, y_{cn})}{\sigma_n'(x_{cn}, y_{cn})} x \ 100 \quad (4.2)$$

Where $\varepsilon_{rn}(x_{cn}, y_{cn})$ *and* $\sigma_{rn}(x_{cn}, y_{cn})$ are the original relative dielectric permittivity and conductivity of nth cell having coordinate (x_{cn}.y_{cn}) respectively. On the other hand, $\varepsilon'_{rn}(x_{cn}, y_{cn})$ *and* $\sigma'_{rn}(x_{cn}, y_{cn})$ are the numerically simulated relative dielectric permittivity and conductivity of nth cell having the respective coordinate (x_{cn}.y_{cn}). In some simulations, the relative mean square error formula [13] is used to measure the error of the reconstruction of the relative permittivity and conductivity; these are given in below:

$$\text{Relative mean square error of relative permittivity, } \delta\varepsilon_r = \frac{\left[\sum_{n=1}^{N}(\varepsilon_{rn}-\varepsilon'_{rn})^2\right]^{1/2}}{\left[\sum_{n=1}^{N}\varepsilon_{rn}{}^2\right]^{1/2}} \quad (4.3)$$

$$\text{Relative mean square error of conductivity, } \delta\sigma = \frac{\left[\sum_{n=1}^{N}(\sigma_n-\sigma'_n)^2\right]^{1/2}}{\left[\sum_{n=1}^{N}\sigma_n{}^2\right]^{1/2}} \quad (4.4)$$

4.2 Flow Chart of Numerical Technique:

The numerical technique is divided into two main parts, which are forward/ direct scattering and inverse scattering problems. In the direct scattering part, the dielectric object under investigation is illuminated by the known incident field that may either be plane wave or a set of unrelated [54] plane waves. The method of moment (MoM) is applied to discretize the desired problem having known complex permittivity using Pseudoinverse algorithm. The total as well as scattered fields are calculated at each measuring point in matrix form. The equivalent surface current due to the incident field is computed from the scattered field by some mathematical operations.

In the inverse scattering problem, knowing the scattered field and respective surface current obtained from direct scattering problem or by measurements, we use matrix operations to arrive at a system that can be solved easily to obtain the required objective function-diagonal matrix. From the diagonal matrix of the object function "O", we can calculate the permittivity as well as the conductivity by some simple mathematical

operations. The following figure summarizes the steps used in the reconstruction process of this algorithm.

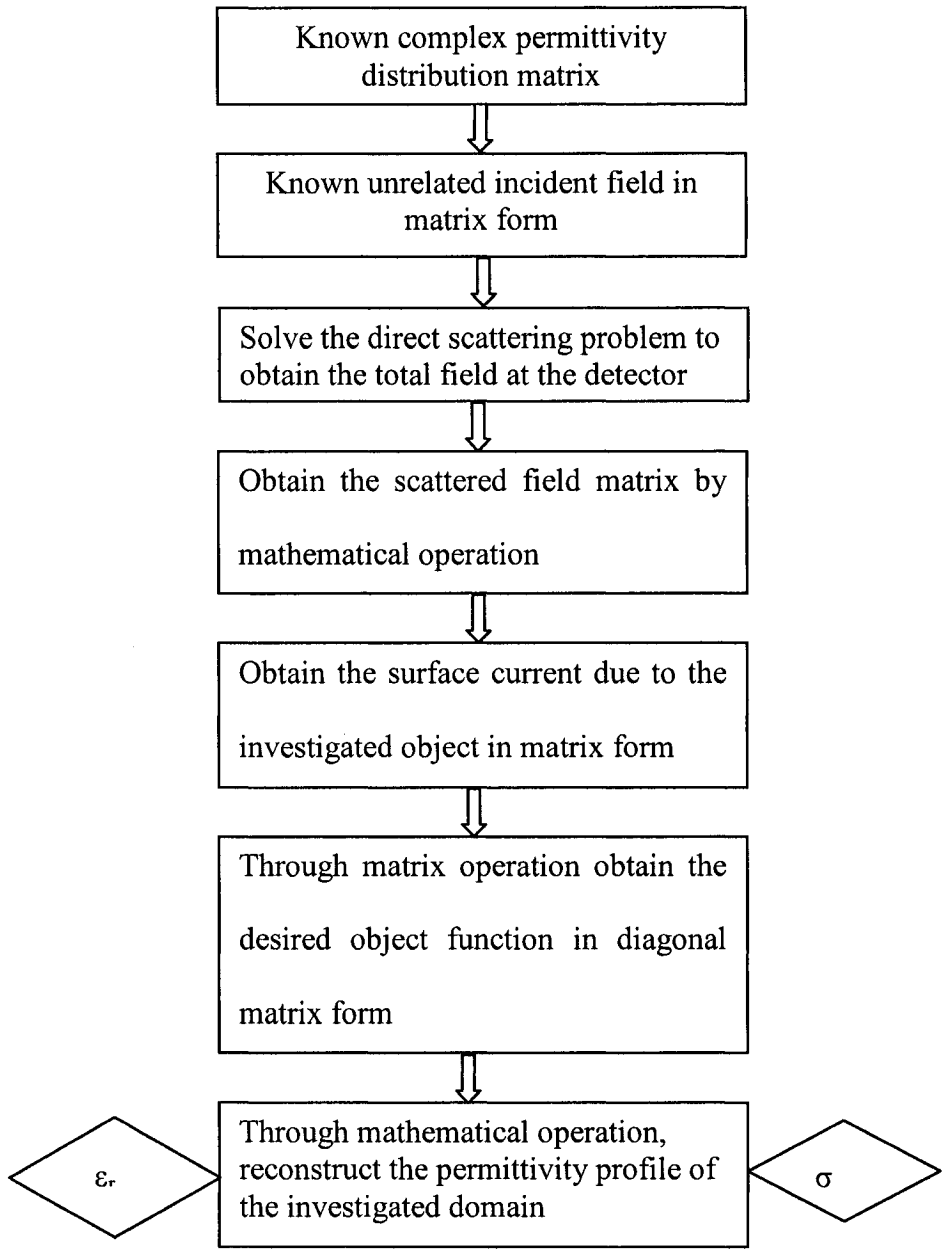

Fig.4.1 Flow chart of the reconstruction process of complex permittivity profile

4.3 Discretization Technique:

The cross section of the layered circular cylindrical scatterer is shown in Fig.4.2. Usually a cylinder can be approximated by equal discretization along the x and y-axes (having square size cell). Such a cell can again be replaced by an elementary circle one that has the same area of the discretized square cell to calculate the Green's function. But the conventional discretization technique is not adopted throughout the following simulations.

For simplicity, we consider a circular dielectric cylinder. The dielectric circular cylinder is divided into many layered circular cylindrical shells (shown in Fig.4.3) whose radius is n x Δ where n =1,2,3,4.....and n is the number of the layered circular cylindrical shell. Each circular cylindrical shell is divided into many square cells whose area is Δ x Δ. The size of the cell near the center of the object is erroneous instead of the square size. The number of square cells for each layered circular shell, N =(2π (n x Δ - 0.5Δ)/Δ) and each square cell makes an angle "θ" at the center of the object where $\theta = 2\pi$ / N. A sample of discretization is shown in Fig.4.3. For the same size of a cylindrical shaped dielectric scatterer, several discretization samples are shown in Fig.4.3 and Fig.4.5. The proposed technique has a great advantage for cylindrical scatterer having different types of layered dielectric (human head/body having skin, bone, Fate, Brain etc.) to ease handling the Green's function as well as the matrix of direct/ forward and inverse methods. In this case, the radius of the cylinder is $\lambda_0/2$ and each side of the small

cell is $\lambda_0/18$ and the number of the layered circular shells, n = 9. The number of the cells for the discretization technique in [13] is 256; whereas this number is 254 for the proposed technique used throughout the following simulations shown in Fig.4.5.

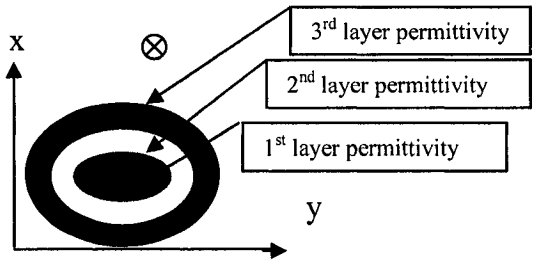

Fig.4.2 The Cross-section of layered dielectric cylinder showing the coordinate system

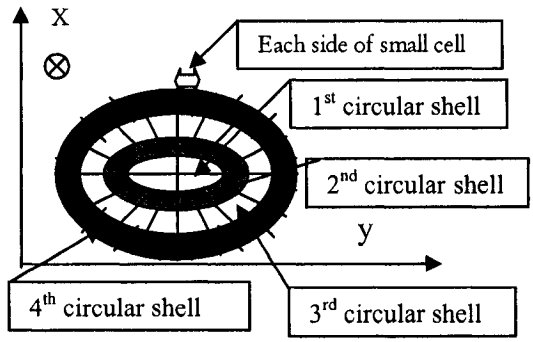

Fig.4.3 The cell for layered discretization of the dielectric

The proposed discretization technique gives us more degree of linearity of the reconstructed permittivity profile of the desired scatterer and gives less spiky values of permittivity that can give false triggered reconstruction. The circular cylindrical scatterer is assumed lossy homogeneous having the permittivity of 4-3i. The reconstructing permittivity profile is shown in Fig.4.6 by the proposed algorithm using the above mentioned both discretization techniques. In this simulation, there is no noise.

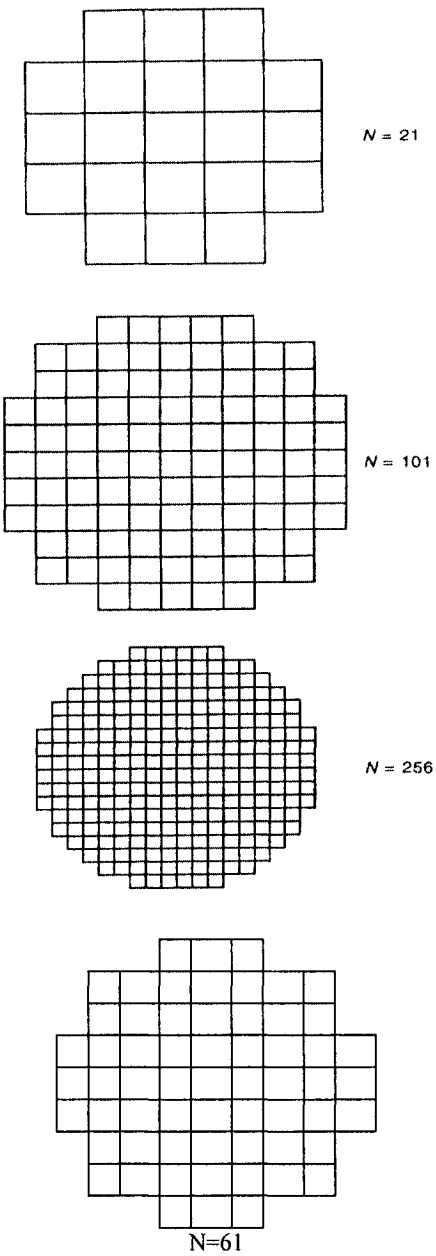

Fig.4.4 Rectangular discretization of a cylinder by conventional method

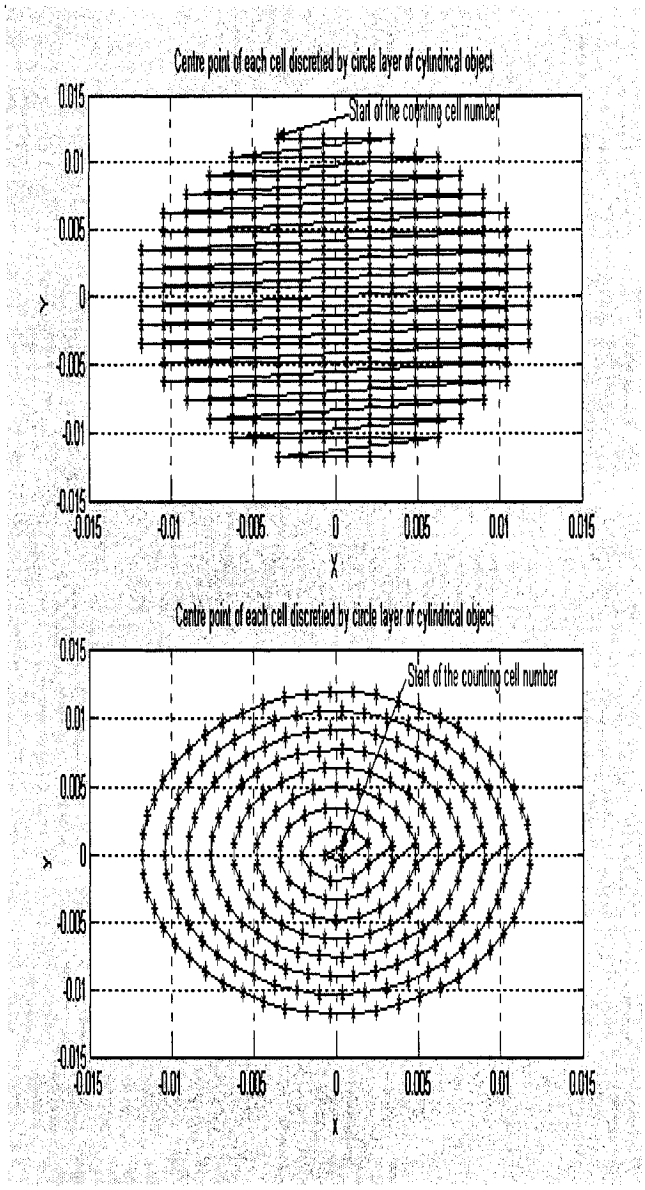

Fig.4.5 Cell number for both discretization methods

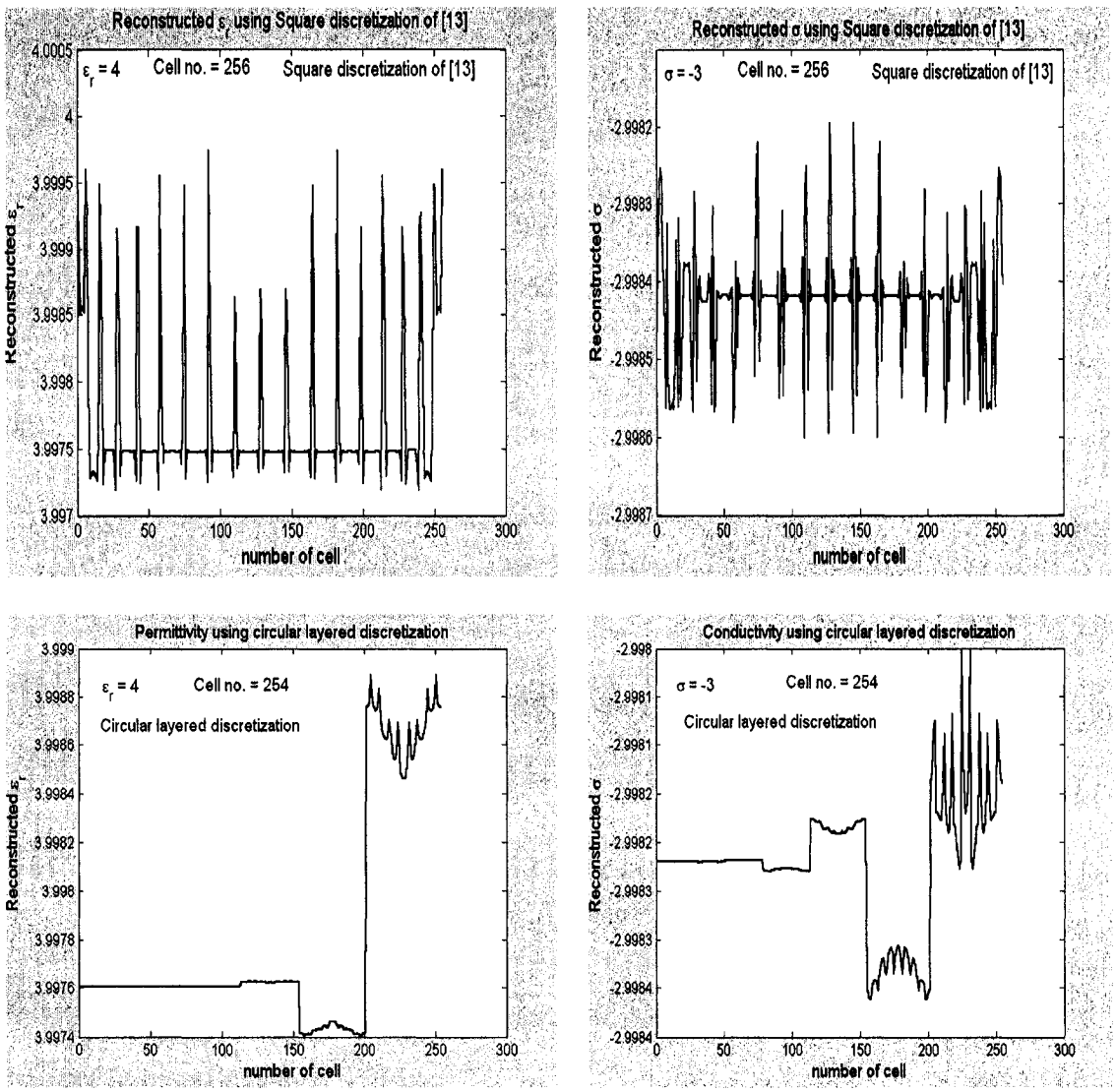

Fig.4.6 Reconstructed profile of permittivity using the above both discretization techniques

4.4 Validation of total field:

The accuracy of the direct scattering procedure of this algorithm is established by comparing the near field data to [12] and to its analytical solution. These field data are obtained from simulating the dielectric cylinder having $1.0\lambda_0$ circumference. In this simulation, we consider cross sectional shape of homogeneous cylindrical dielectric object divided into 256 sub areas (small square cell) shown in Fig.4.7. We use TM wave illumination, in the sense of Richmond's statement [9], the interrogating electromagnetic wave has been assumed to be a uniform plane wave propagating along the x axis and with the electric field polarized along the z axis, which is taken to be parallel to the scatterer axis. The cylindrical scatterer has been assumed to be lossless homogeneous with relative permittivity ε_r =2.56. The values of total electric field at all measurement points have been obtained by the use of a numerical program and as well as scattering electric field. This circular cylindrical dielectric can be approximated by equal discretization along x and y axis (small square cells shown in Fig.4.7).

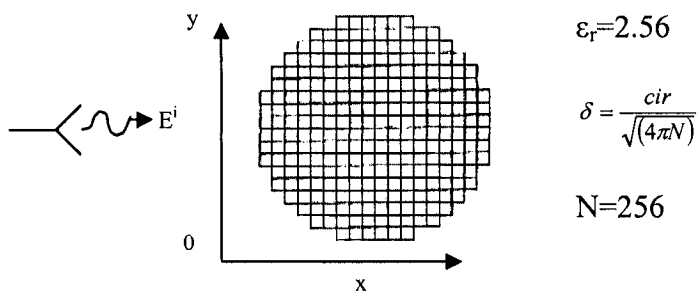

Fig.4.7 The cross-section of the cylindrical dielectric having 256 cells

Such a cell can again be replaced by an elementary circle that has the same area of the small square cell to calculate Bessel and Hankel functions. Relationship among radius, wave-length and step size (delta, 256 cells) have been adopted as followings: Circumference of the cylindrical object, cir= $2\pi a = 1.0\lambda_0$ where 'a' is radius. Operating frequency for this simulation, f =230.84 MHz. 18 steps along x-axis central cut and 18 steps along y-axis central cut are shown in Fig.4.1. Let the number of cell, N=21, 101, 256.....etc. Generally,

$$\delta^2 x \quad N = \pi \quad x \quad a^2 = \pi \quad x \quad (\frac{cir}{2\pi})^2 \text{ i.e. } \delta = \frac{cir}{\sqrt{(4\pi N)}}$$

e.g. for 21 cells, $\delta_{21} = cir/\sqrt{}(\pi \times 84) = \lambda_0/\sqrt{}(\pi \times 84)$,

For 101 cells, $\delta_{101} = cir/\sqrt{}(\pi \times 404) = \lambda_0/\sqrt{}(\pi \times 404)$ and

For 256 cells, $\delta_{256} = cir/\sqrt{}(\pi \times 1024) = \lambda_0/\sqrt{}(\pi \times 1024)$.

For numerical solution, the equivalent radius 'a' of the elementary circle which has the same area of a discretized cell, is 'a' = $\delta/\sqrt{}(\pi)$.

Unlike inverse scattering, the direct scattering has the analytical solution as well as the numerical solution. The numerical solution is also validating with the exact/analytical one. Magnitude of Et (total electric field) on the dielectric from [12] and from analytical and numerical simulation is shown in Fig. 4.8 and 4.9 respectively.

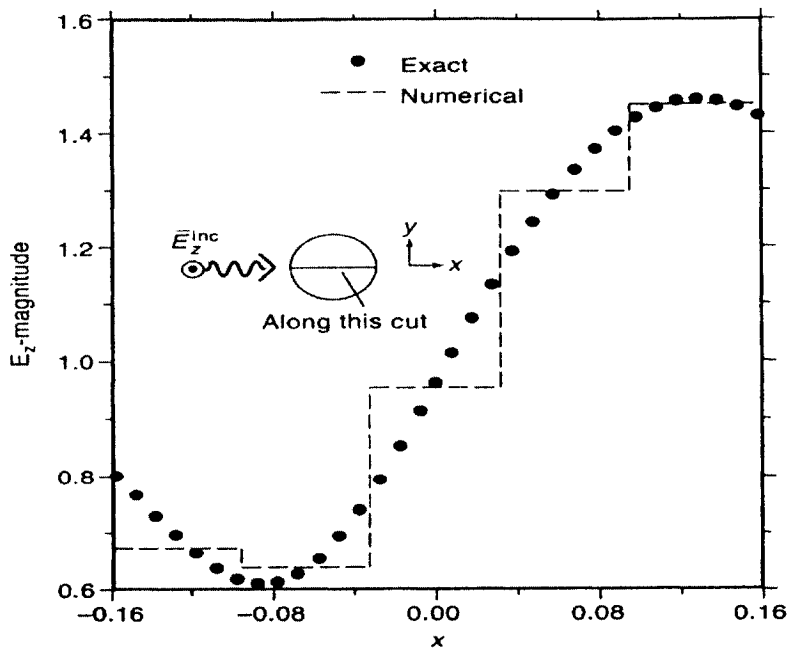

Fig. 4.8 The value of Et along central cut (along y =0) for [12]

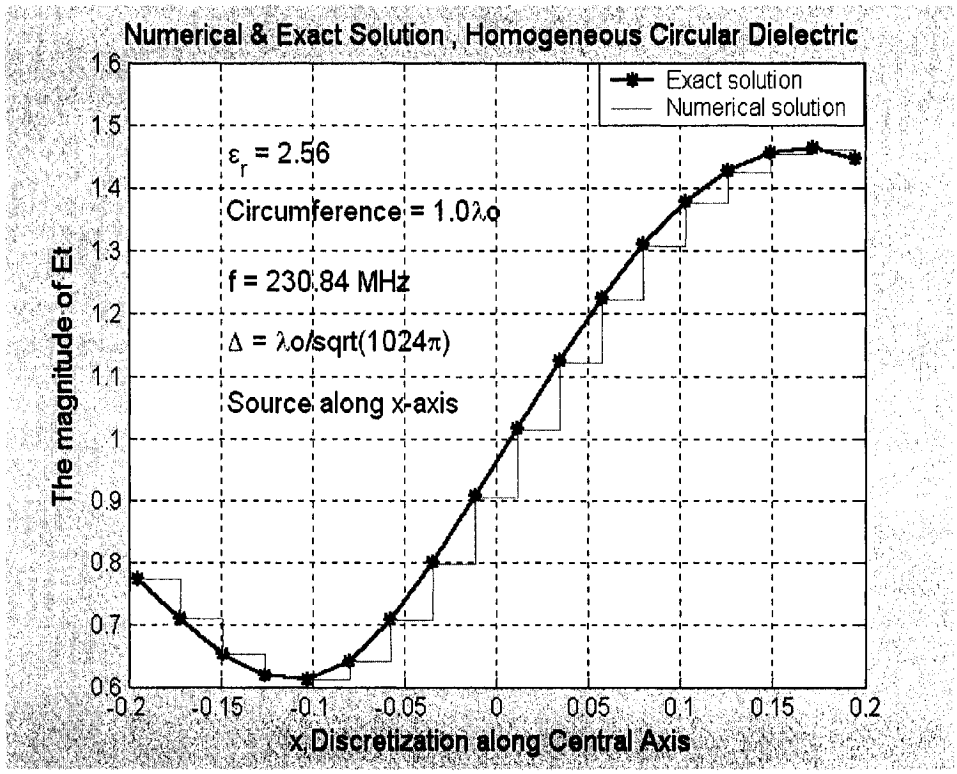

Fig.4.9 Et along central cut (along y =0) for analytical and numerical solution

Being insignificantly different in magnitude, both numerical solution and exact equation solution follow the same pattern of plots of E_t as given in [12]. But numerical solution and exact equation solution between themselves produce fantastically matched results. Numerical technique involves calculation over discrete values and the discretization errors in dielectric or in the near field region are not balanced out. So the difference in magnitude may occur. And the 'exact' equation solution adopted here does not involve analog integration. Rather it contains summation over some finite numbers (-Nmax to Nmax, truncation no.) for Bessel and Hankel functions. This is why the results deviate very slightly from [12].

Total field due to different sizes of the cell are also computed in this simulation. Table-I gives total field at the center of the homogeneous circular cylinder with circumference of $0.5137\lambda_0$ and relative permittivity ε_r =10 for 21, 61, and 101 cell numbers of this cylinder. The frequency is 230.84 MHz. Plane wave with unity magnitude incident on the circular cylinder. The numerical results from these simulations due to the mentioned cell size of $\lambda_0/5$, $\lambda_0/9$ and $\lambda_0/11$ are compared with the exact/analytical solution and also with table-2.11 of [12]. The cross-sectional area of the models is scaled in order to equal that of the desired circular geometries. The phase and magnitude of the total field at the center of this cylinder for the above mentioned discretized cell numbers have good agreement with the exact solution and also with all results of table-2.11 of [12] and accuracy of the numerical simulation is excellent. For exact solution, the truncation number N_{max}= round ($3*k_d*r+10$) where k_d is the wave number in dielectric and "r" is the radius of the dielectric cylinder and the summation of the equation of the exact solution is done over range ($-N_{max}$ to $+N_{max}$) instead of

(– ∞ to +∞).

Total Cell no.	From Simulation				Table 2.11 of [12]			
	Exact		Simulation		Exact		Simulation	
	$\|E_t\|$	φ_{Et}	$\|E_t\|$	φ_{Et}	$\|E_t\|$	φ_{Et}	$\|E_t\|$	φ_{Et}
21	0.7798	-94.8121	0.7688	-94.7448	0.780	-94.82	0.770	-94.75
61	0.7798	-94.8121	0.7785	-94.6494	0.780	-94.82	0.779	-94.66
101	0.7798	-94.8121	0.7785	-94.7420	0.780	-94.82	0.780	-94.82

Table-4.I: Total field for different discretization at the center of the cylinder

From Table-4.I, we can see that higher discretization produces a more accurate result for total field. However, computation time and memory requirement put a restriction on the maximum number of discretization that can be used.

4.5 Validation with Born Approximation method:

This simulation is involved the use of the layered inhomogeneous lossy weak scatterer. The near field distribution as well as the complex permittivity distribution is computed using the well-known "Born Approximation" method and the proposed algorithm. The diameter of the cylindrical cross section is λ/2 and the discretized cell number is 254. The object has three kinds of scatterer such as weak scatterer in the central position, medium weak scatterer in middle position and more weak scatterer in the out most position. There are 9 (nine) circular layers of the lossy dielectric cylindrical object. The inner 3(three) layers have actual complex permittivity, $\varepsilon = \varepsilon_0 \varepsilon_r - j\frac{\sigma}{\omega} = \varepsilon_0$

(3.5 -j0.9/$\varepsilon_0\omega$). The middle 3 (three) layers have actual complex permittivity, $\varepsilon = \varepsilon_0$ (2.5-j0.5/ $\varepsilon_0\omega$). And the outer 3 (three) layers have actual complex permittivity, $\varepsilon = \varepsilon_0$ (1.5-j0.2/ $\varepsilon_0\omega$). We use TM wave illumination, in the sense of Richmond's statement [9], the interrogating electromagnetic wave has been assumed to be a uniform plane wave propagating along the x axis and with the electric field polarized along the z axis, which is taken to be parallel to the scatterer axis. The discretized cells are as following Fig.4.10.

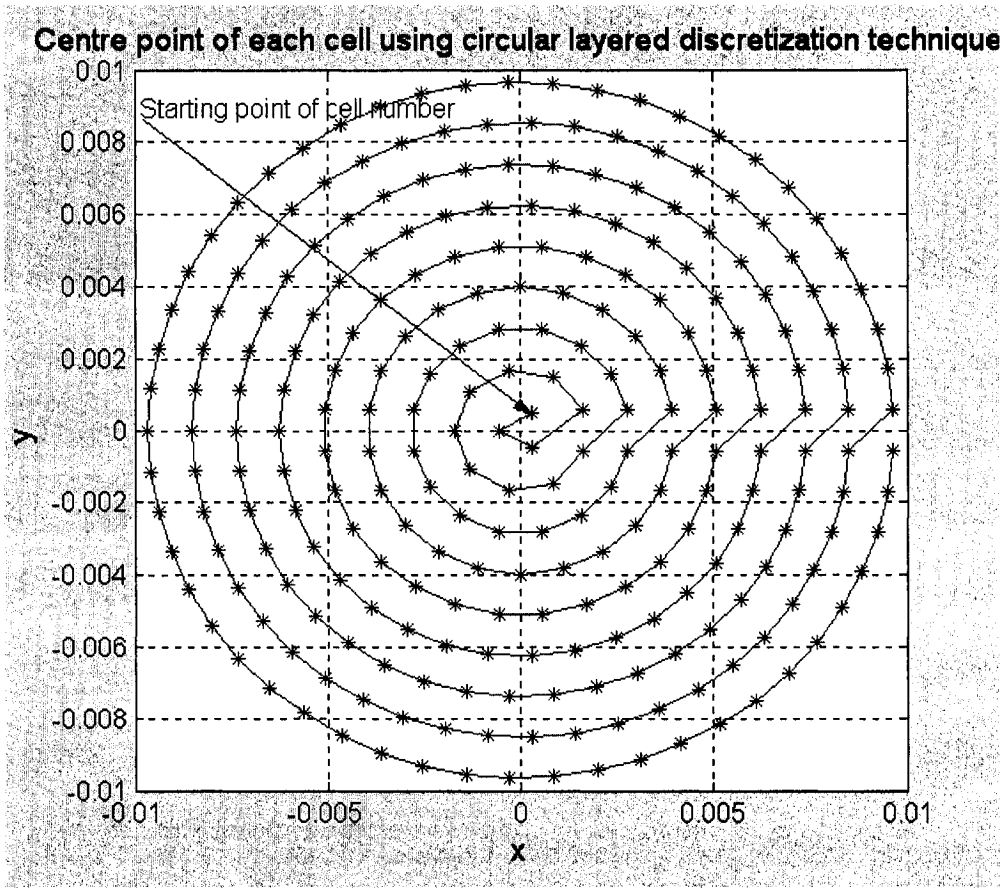

Fig.4.10 Total cells of 9 layers of the dielectric having size of each cell is (λ_0/18 x λ_0/18)

The permittivity of each cell obtained from simulation using "proposed algorithm" and "Born Approximation algorithm" are as following Fig.4.11 and Fig.4.12. The permittivities achieved from both algorithms have good agreement with the original value of the permittivity with some errors. The fluctuation of permittivity got from both algorithms with respect to the original/actual value of the permittivity is shown in following Fig.4.13. The inner 3 (three) layers contain cell no.1 to 28, the middle 3 (three) layers contain cell no. 29 to 113 and the rest layers contain cell no. 114 to 254. The inner layer, that contains high permittivity scatterer, has higher fluctuation of permittivity got from Born Approximation algorithm than Pseudo-inverse algorithm. The outer scatterer, that contains weak scatterer, has excellent agreement between Born Approximation algorithm and Pseudo-inverse algorithm with very very less fluctuation of permittivity with respect to the original value shown in Fig.4.13. Born Approximation gives worst value of permittivity for strong scatterer but on the other hand it gives good result for weak scatterer like Pseudo-inverse algorithm. Pseudo-inverse algorithm gives promising result for all kinds of scatterer in case of reconstructing permittivity profile of the complex dielectric object. For conductivity profile, there is different scenery discussed later.

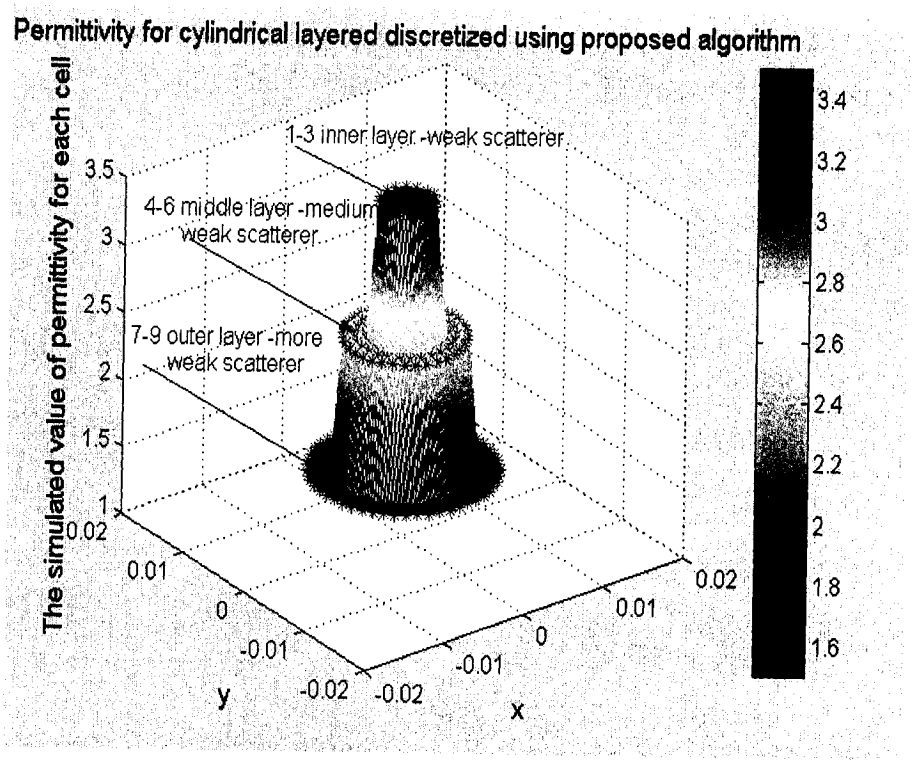

Fig.4.11 The simulated permittivity using proposed Psuedoinverse algorithm

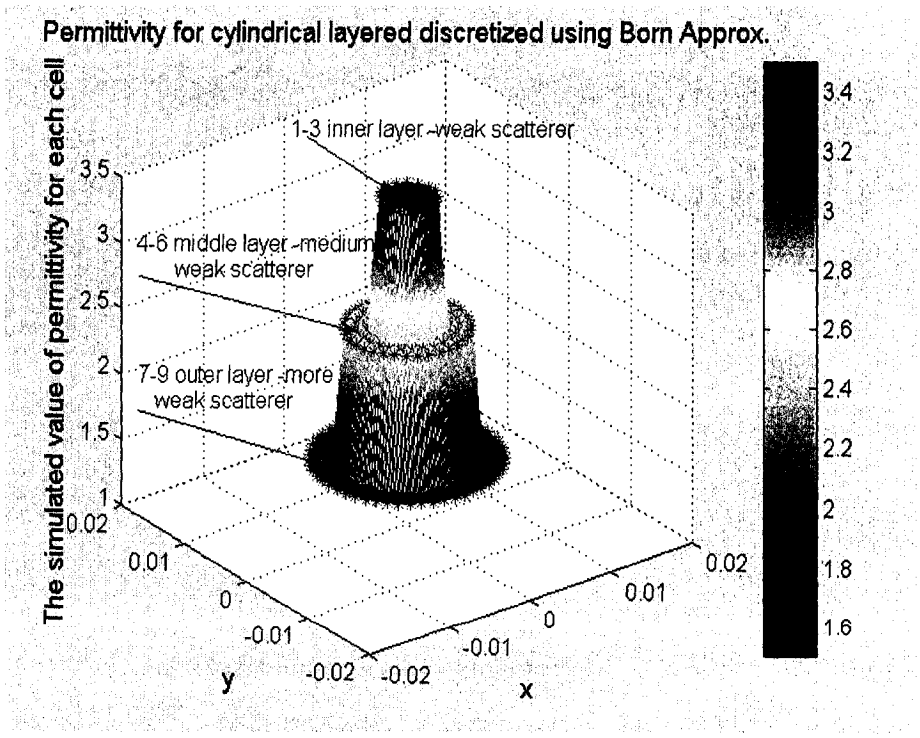

Fig.4.12 The simulated permittivity using Born Approximation method

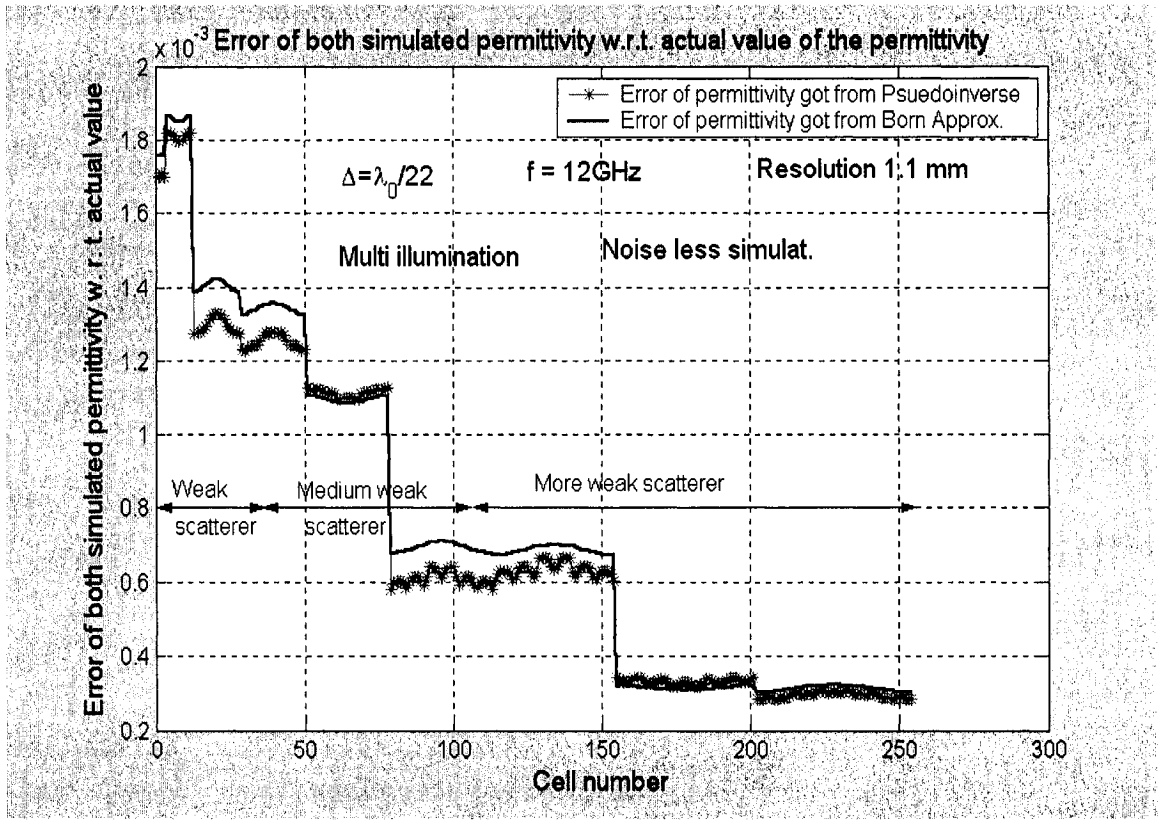

Fig.4.13 Fluctuation of permittivity w. r. to original value obtained from both algorithms

The conductivity of each cell got from simulation using "Pseudo-inverse algorithm" and "Born Approximation algorithm" are as following Fig.4.14 and Fig.4.15. The fluctuation of conductivity got from both algorithms with respect to the original / actual value of the conductivity is shown in following Fig.4.16. The reconstructed profiles follow the same pattern for both algorithms with some ±errors with respect to the actual/original value for conductivity.

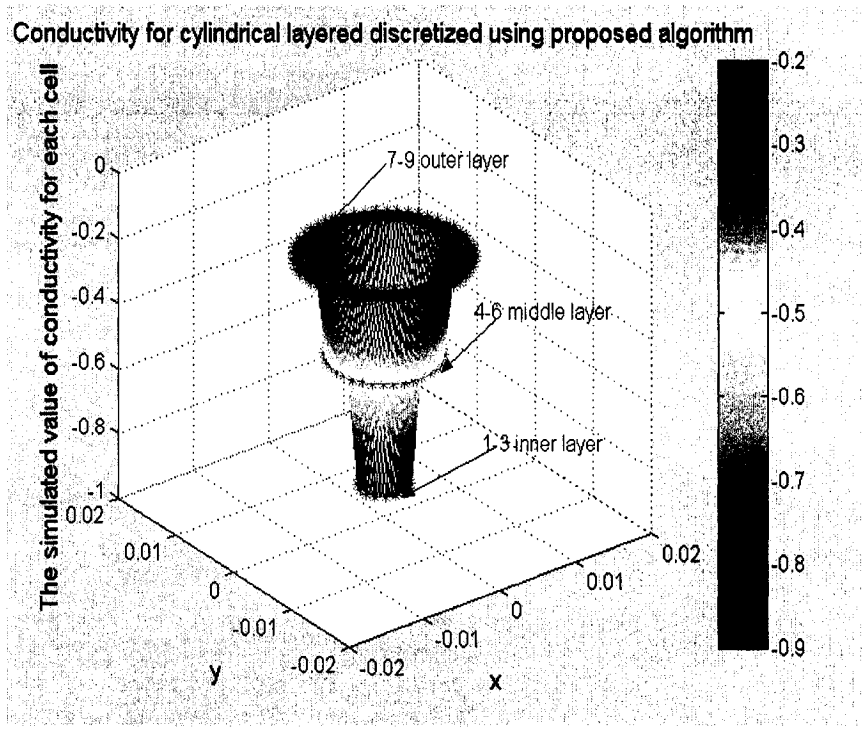

Fig.4.14 The simulated conductivity using Pseudoinverse algorithm

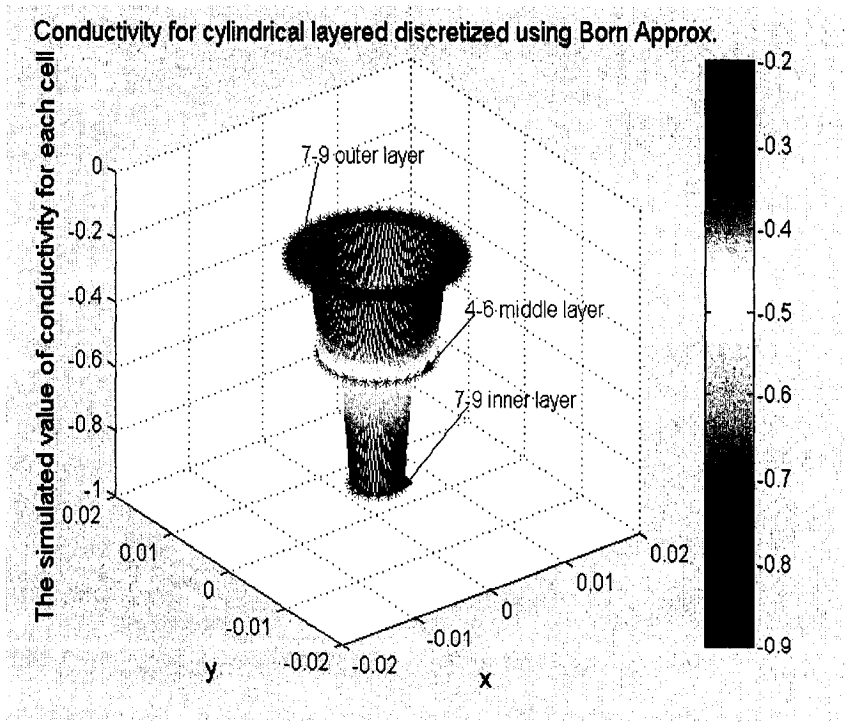

Fig.4.15 The simulated conductivity using Born Approximation method

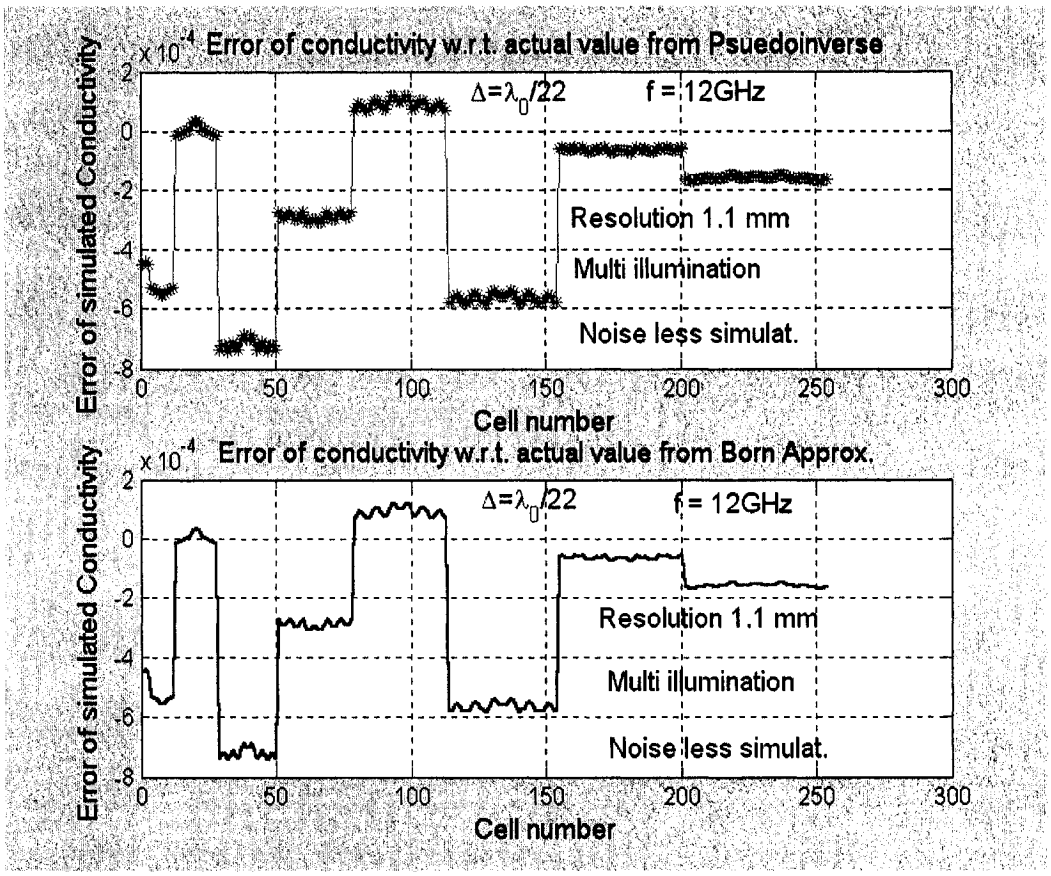

Fig.4.16 The fluctuation of the value of Permittivity got from "Pseudoinverse" and "Born Approximation method"

4.6 Validation of location of scatterer and the permittivity:

The next simulation is to explore the possibility of determining the location of scatterer with the error of the reconstruction of the permittivity of the investigated domain for big scatterer using the proposed algorithm and validate with [13]. TM, polarized along z-axis, plane wave having unity magnitude along x-axis is an incident wave. The area of the investigated region is $(5/3)\lambda_m$ X $(5/3)\lambda_m$ square size and divided

into 25 square cells having $(1/3)\lambda_m$ length of each side. We consider the rectangular scatterer having size of $(1/3)\lambda_m$ X $(2/3)\lambda_m$, which occupy two sub-area of the investigated domain. Here the investigated area contains scatterer in four (4) configurations. In these configurations, the sub-area of investigated domain contains scatterer in cell no. (17&18), (16&17), (17&22) and (17&12) separately for each simulation shown in Fig.4.17.

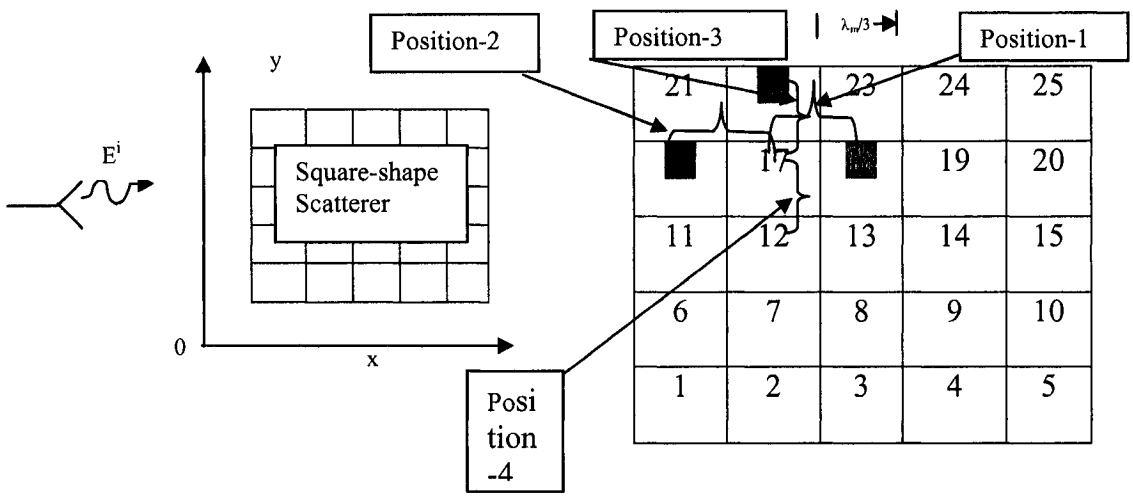

Fig.4.17 Four configurations due to changing the position of big scatterer

In all configurations, cell no. 17 occupied by the scatterer is common. The permittivity of scatterer is 3 and the investigated domain has unity permittivity. The simulated result for each configuration is picked up in table-4.II.

Confi -gura -tion	Cell p contained by the scatterer	Permittivity of scatterer in p cell, ε_{rp}		Relative mean square error, $\delta\varepsilon_r$	
		Simulated Value	table-III of [13]	Simulated Value	table-III of [13]
1	17	2.9985	2.01	3.313 x 10e-4	0.27
	18	2.9989	3.87		
2	16	2.9989	2.45	2.621 x 10e-4	0.19
	17	2.9990	2.24		
3	17	2.9986	2.51	2.900x 10e-4	0.13
	22	2.9989	2.75		
4	12	2.9986	1.87	3.106 x 10e-4	0.25
	17	2.9986	2.24		

Table-4.II: Dielectric permittivity-reconstruction for big scatterer.

Fig.4.18 shows the permittivity of the scatterer due to 4 (four) different positions in the investigated domain (shown in Fig.4.17) for table-III of [13] and the simulated value respectively. Hence the position of the scatterer is determined with great accuracy but the permittivity of the scatterer for each position have good agreement in magnitude between the simulated value and the original value but the difference in magnitude between the simulated permittivity and that of table-III of [13]. The reconstructed profile of the simulation is far better than that of table-III of [13].

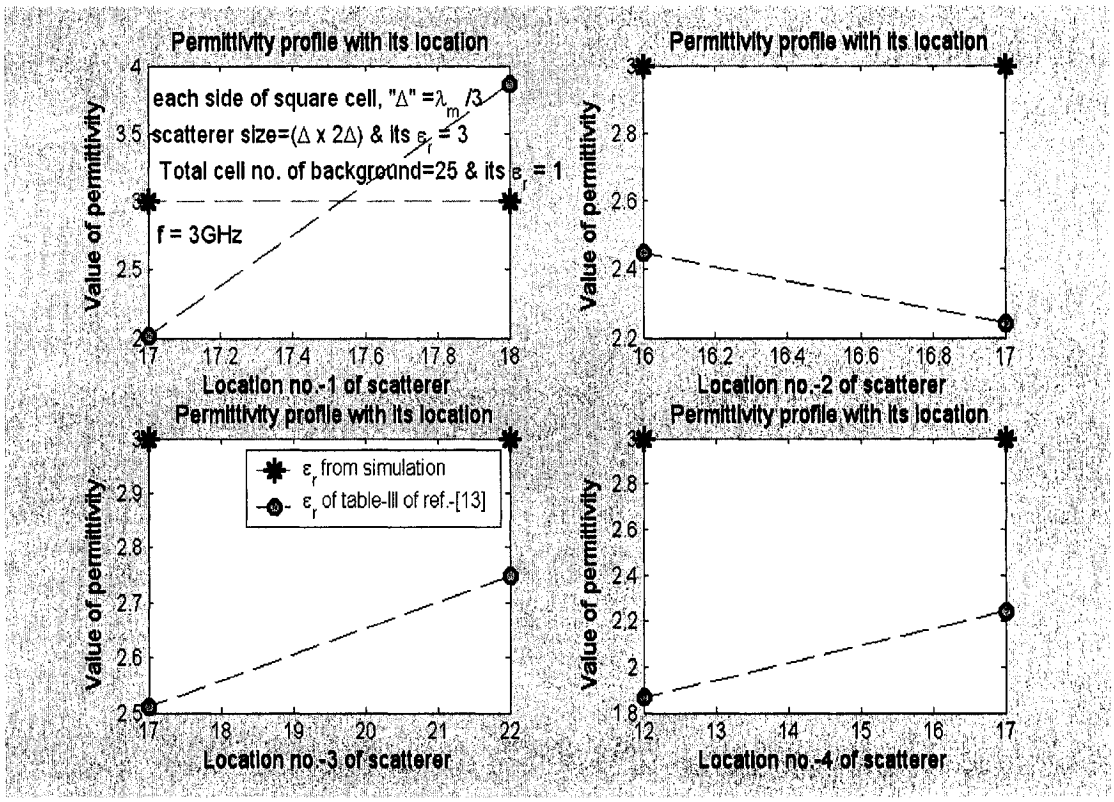

Fig.4.18 Permittivity of the scatterer due to 4 different positions in the investigated domain

It is needed to find the percentage-normalized error for measuring the particular error of the reconstruction of the scatterer. Fig.4.19 shows the percentage-normalized error of the constructed permittivity profile from the simulation and table-III of [13] for each position of the scatterer. The percentage-normalized error of the permittivity for each position of the scatterer from the simulation is far better than that of table-III of [13]. Being significantly different in magnitude of the percentage-normalized error of the permittivity for each position of the scatterer, the numerical solution follows the exactly same pattern of the plot of the percentage-normalized error of the permittivity for each position of the scatterer of table-III of the [13].

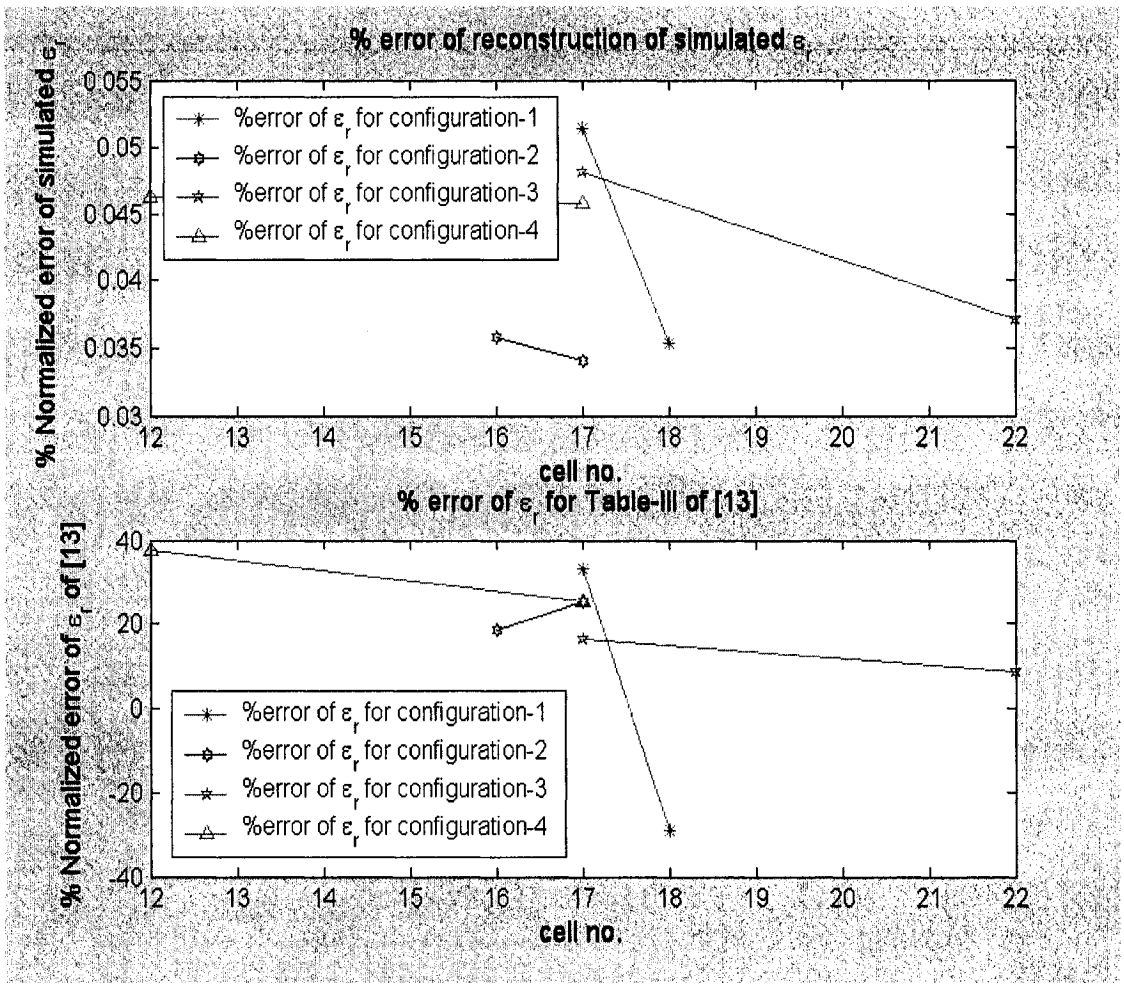

Fig.4.19 Normalized error of reconstructed permittivity from simulation and table-III of [13]

To further investigate the accuracy of the algorithm in handling small scatterer in lie of big scatterer, the permittivity profile with its location is obtained in below using [13] and the Pseudoinverse algorithm. We consider that a square area is $(5/3)\lambda_m$ x $(5/3)\lambda_m$ for the investigated domain and divided into 25 sub areas (small square cell). The investigated domain is made up o f 25 equally spaced measurement points. These points

are arranged in different way. We use TM wave illumination. Fig.4.20 shows the geometrical configuration of the background media adopted for these simulations. The scatterer has been assumed to be lossless homogeneous, with relative permittivity ε_r =3. The cross-sectional shape of the scatterer is a $\lambda_m/3$- sided square emerged in the background media having unity permittivity and its position is made to vary inside the investigated area. The values of scattering electric field at all measurement points have

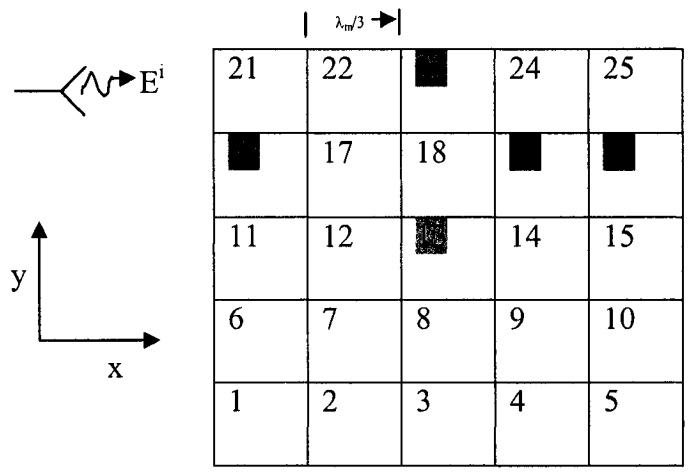

Fig.4.20 The geometrical configuration of small scatterer for simulation

been obtained by means of the numerical program through the well known "Richmond theory" [9]. Assume that the interested region contains scatterer at a position mentioned cell no. 13, 16, 19, 20 & 23 shown in Fig.4.20. These 5 positions of the scatterer are involved with 5 separate numerical simulations. Table-4.III gives the results of the reconstruction of the scatterer for a given number of the significant locations inside the investigated background media. The first column of this table indicates the numbers of the cells (according to the numbering in Fig.4.20) where the scatterer have been placed in the background media; the second column indicates the values of the reconstructed dielectric permittivity in sub-area (indicated by p) containing the scatterer; and the third

column gives relative mean square error, $\delta\varepsilon_r$ which has been used also to take into account the reconstruction errors related to all cells even where no scatterer is present and where one should expect unit values of the relative dielectric permittivities. Finally, the fourth column in the table gives the worst values of the reconstructed relative dielectric permittivities in the cell that does not contain the scatterer.

Cell p contain scatterer	Permittivity of the scatterer in p cell, ε_{rp}	Relative mean square error, $\delta\varepsilon_r$	The worst value of reconstructed dielectric permittivity ε_{rq}
13	2.9987	2.270 x 10-e4	1.0001
16	2.9991	1.639 x 10-e4	1.0001
19	2.9987	2.219 x 10-e4	1.0001
20	2.9991	1.644 x 10-e4	1.0001
23	2.9990	1.693 x 10-e4	1.0001

Table-4.III: Dielectric permittivity-reconstruction from numerical simulation.

For the validation of the code of the numerical simulation with table-I of [13], the Fig.4.21 shows the value of the reconstructed permittivity of the scatterer placing in different 5 positions in the background domain. The value of permittivity of the numerical simulation gives the better-reconstructed profile compared to that of table-I of the [13] but the determination of the position of the scatterer is exactly same as that of table-I of the [13] with excellent accuracy.

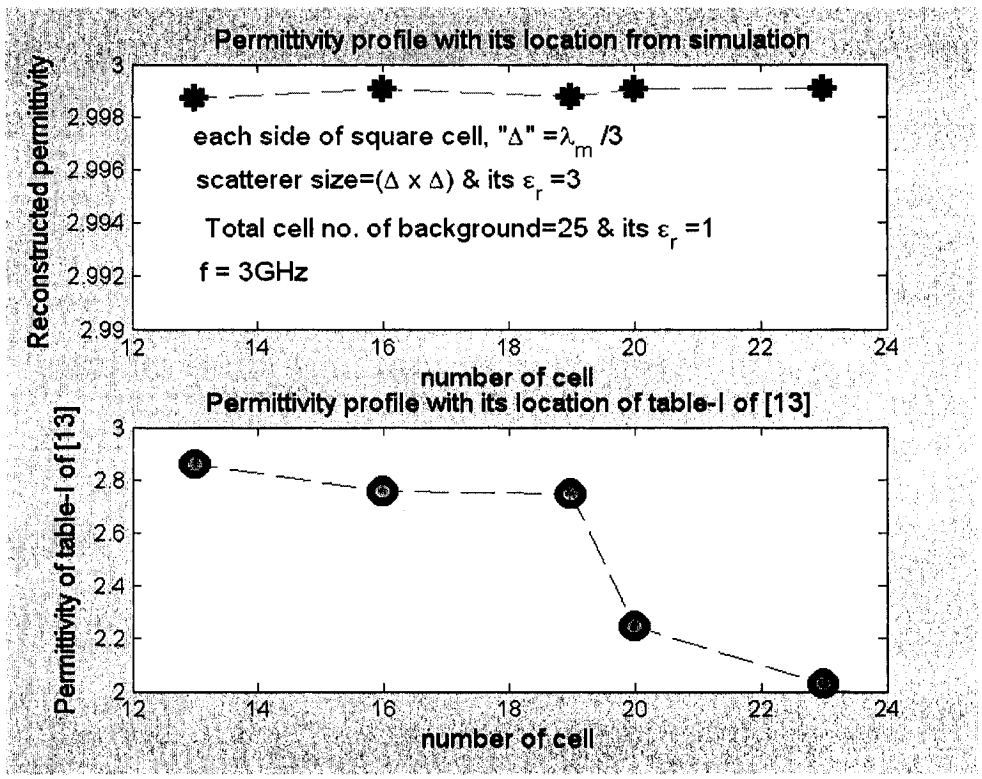

Fig.4.21 The value of permittivity of reconstruction compared to table-I of [13]

Here there is a scatterer having size ($(1/3)\lambda_m$ x $(1/3)\lambda_m$) in the 17^{th} cell of the investigated domain. The other cells have unity permittivity. Fig. 4.22 shows the values of permittivitties of all cells for numerical simulation and for the values of table-II of [13]. It seems that the reconstructed permittivitties have the promising agreement with the original value of permittivitties but the permittivities of table-II of [13] have more erroneous values.

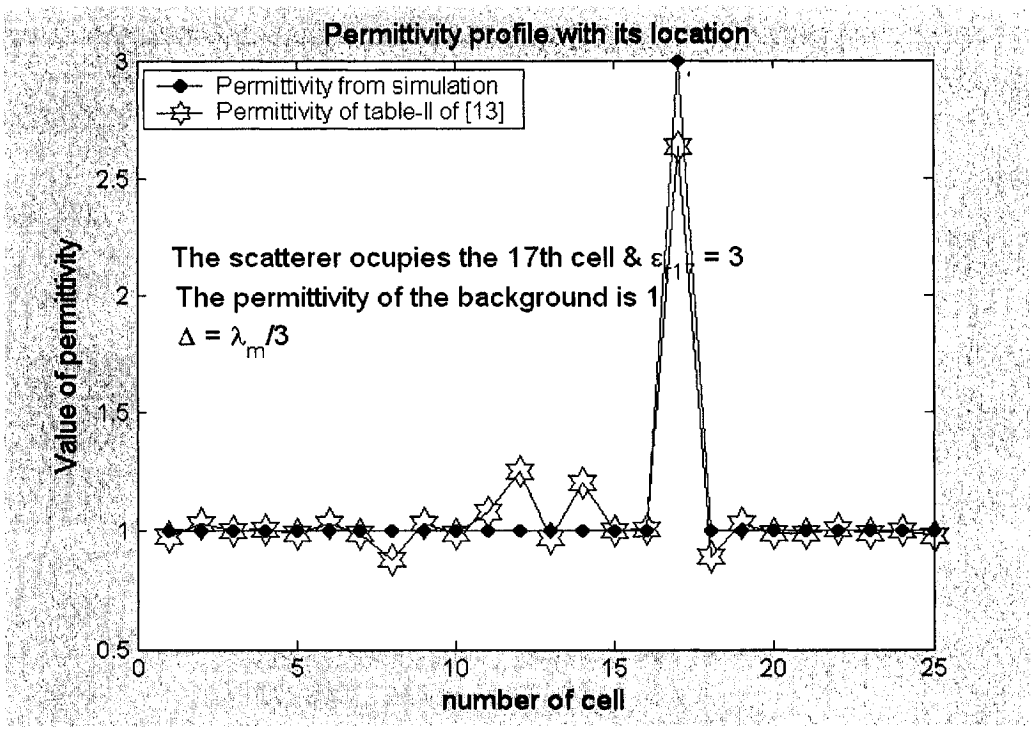

Fig.4.22 Permittivity profile of the simulation and table-II of [13]

4.7 Measurement of the uncertainty of the algorithm:

It is desirable to have independent methods for estimating the accuracy of the simulated numerical solution got from this algorithm. Since the boundary condition embodied in the integral equation is enforced only at the match points, one way of studying the accuracy is to compute the electric field at other points within the cylindrical dielectric object. The boundary condition embodied in the relationship

$$E_{inc}^{z} = E_{t}^{z} - E_{s}^{z}$$

will be satisfied exactly by the true solution and thus we do not expect perfect agreement from approximate result. The amount of deviation is an indicative of the overall accuracy of the numerical simulation. In this simulation, the dielectric circular cylinder have

3(three) layered scatterer whose permittivity, ε_r = 8, 48 and 88 respectively. The radius of the multi layer circular cylinder is $\lambda_d/3$ and the size of each side of discretized square cell is λ_d /18. The operating frequency is 2GHz. The resolution of this simulation is 2.9mm to 0.9mm varying on the value of the permittivity, ε_r =8 and 88 respectively. Fig.4.23 shows the incident field at the boundary got from the known value and got from the total field of the simulation minus the scattered field of the simulation.

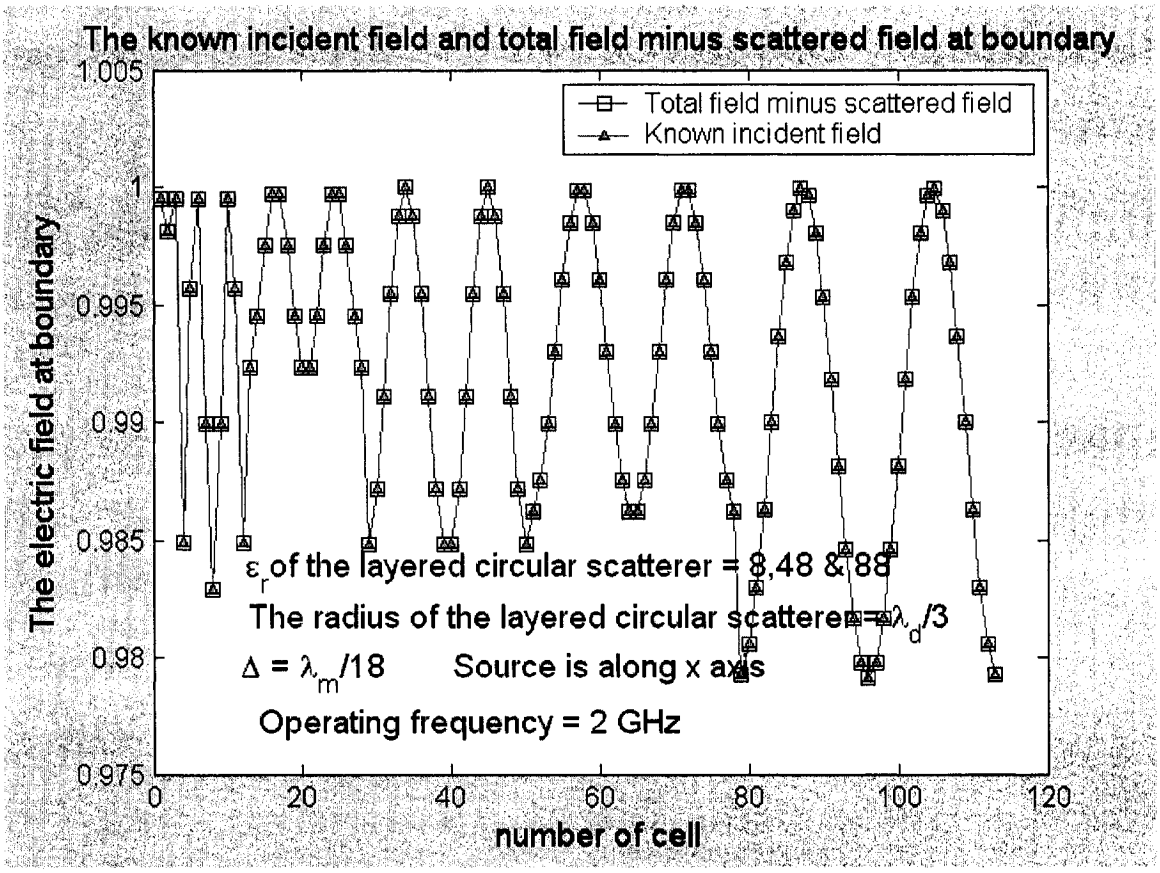

Fig.4.23 The electric incident field and total field minus scattered field at boundary

The deviation of the total field minus the scattered field of this simulation with respect to the known incident field is shown in Fig.4.24. The range of this deviation is ranging ± 1.2 x 10^{-16} that is very small. So the accuracy of the numerical simulation using the

proposed algorithm is very high.

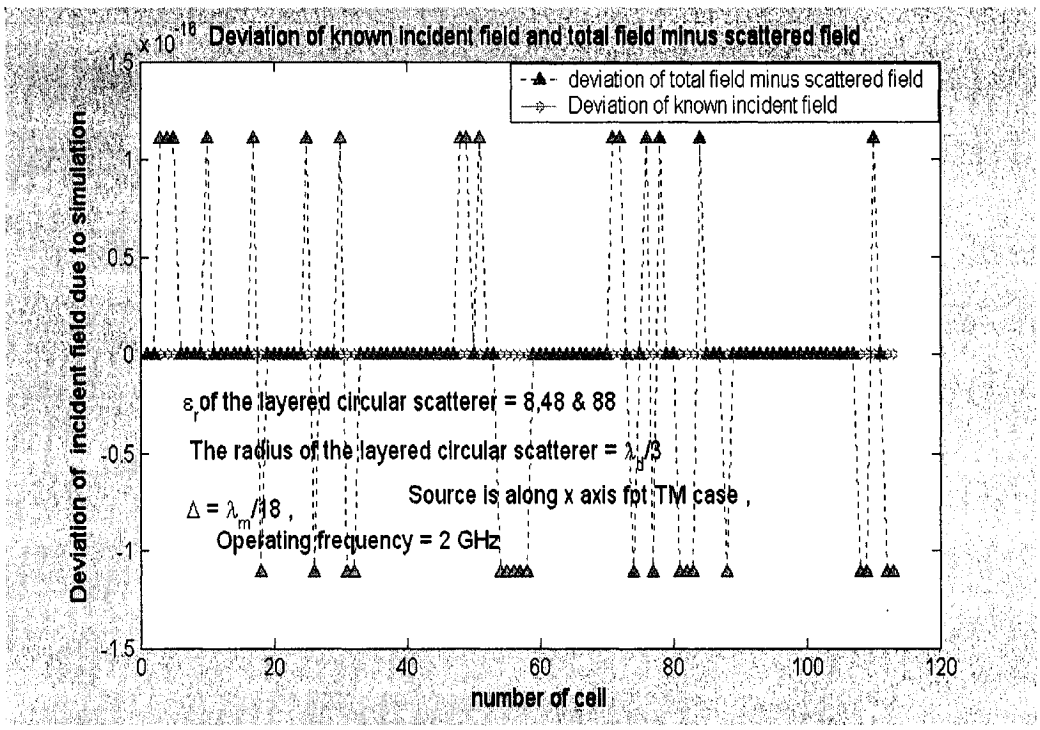

Fig.4.24 Deviation in satisfying the electric field boundary condition for TM case

CHAPTER - 5

Numerical Simulation and Results

5.1 Introduction:

The reconstruction methods, which were proposed, can be classified into two main categories, namely the spectral domain method and the spatial domain method. The spectral domain method has utilizes a well-developed theory and techniques. This method employs the Born and Rytov approximation in the reconstruction, which makes it only applicable in the presence of weak scatterers. On the other hand, the spatial domain method theoretically imposes no restrictions on the complex permittivity distribution of the dielectric bodies to be reconstructed. The main disadvantages of these methods are their great sensitivity to the noise.

In order to study the effect of the measured data uncertainty on the reconstruction process, we add the noise array to measured total field data. We then find the scattered field from this noisy total field. The noise is constituted by an independent sequence of random variables. These sequences have zero mean and a variance that can be varied to obtain different signal to noise ratios (SNR):

$$SNR = 10 \log \frac{\|E^s\|^2}{\|n\|^2} \text{ in dB.}$$

Various types of two-dimensional dielectric bodies have been investigated including simple homogeneous cylindrical objects, inhomogeneous cylindrical objects

and layered inhomogeneous cylindrical objects. A plane wave or a set of unrelated plane wave [54] are used to illuminate the investigated object for achieving a better-reconstructed complex permittivity profile. The cell-size of the discretization is some fraction of a wavelength (from $\lambda_0/3$ to $\lambda_0/22$ where λ_0 is the wave length in free space) in some numerical simulations but in other simulations, it is a function of the permittivity of the investigated inhomogeneous dielectric and as well as λ_0.

In the following numerical simulations, the proposed method cited in chapter 3 is applied to various geometrically complex inhomogeneous dielectric bodies within noisy or noiseless environment. The multi illumination method is presented for the reconstruction of the complex permittivity. Results of the simulations using the proposed algorithms are reported in the following sections. The objective of these simulations is to justify the capabilities of this method and to test the strength of this method with uncertainty.

5.2 Effect of multi illumination with high resolution:

TM wave illumination, according to Richmond's statement [9], is the interrogating electromagnetic wave. The field incidents on the dielectric scatterer having permittivity 4-3i with incident angle ϕ_i = 0°, 90°, 180°, 270° and 360° where ϕ_i is the angle with x-axis. Here Fig.5.1, 5.2, 5.3 and 5.4 show the reconstructed permittivity for ϕ_i = 0°, 90°, 180° & 270° but the reconstructed profile for the position of the source at 0° and 360° is exactly same because these indicate the same point. So, no needs to show the plot of the reconstructed profile for ϕ_i = 360°.

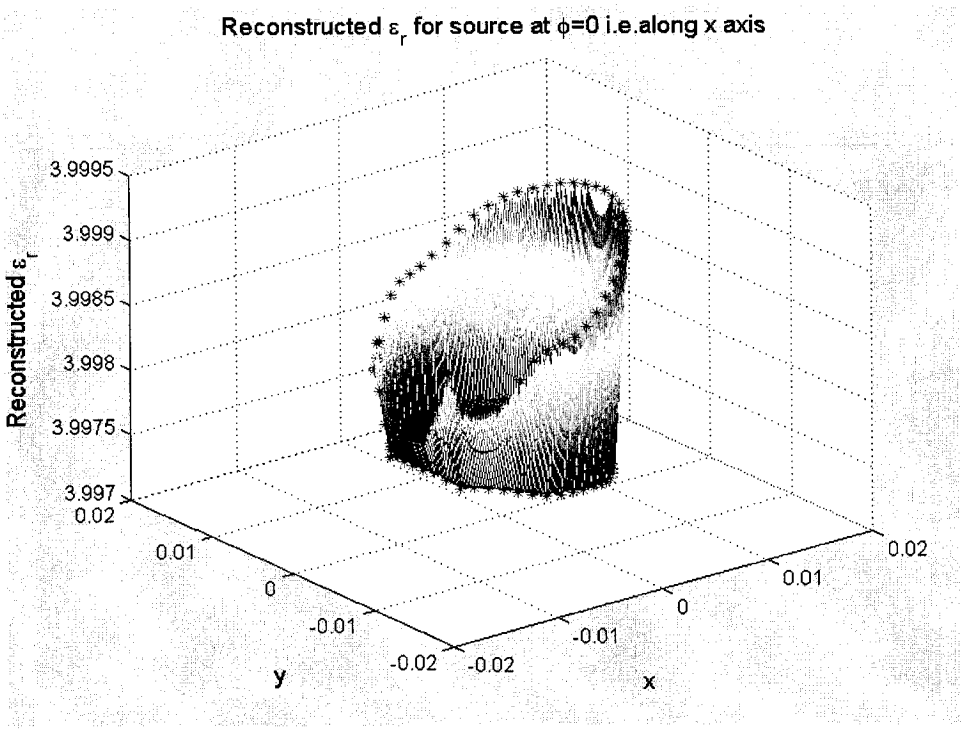

Fig.5.1 Reconstructed permittivity for source at $\phi_i = 0°$

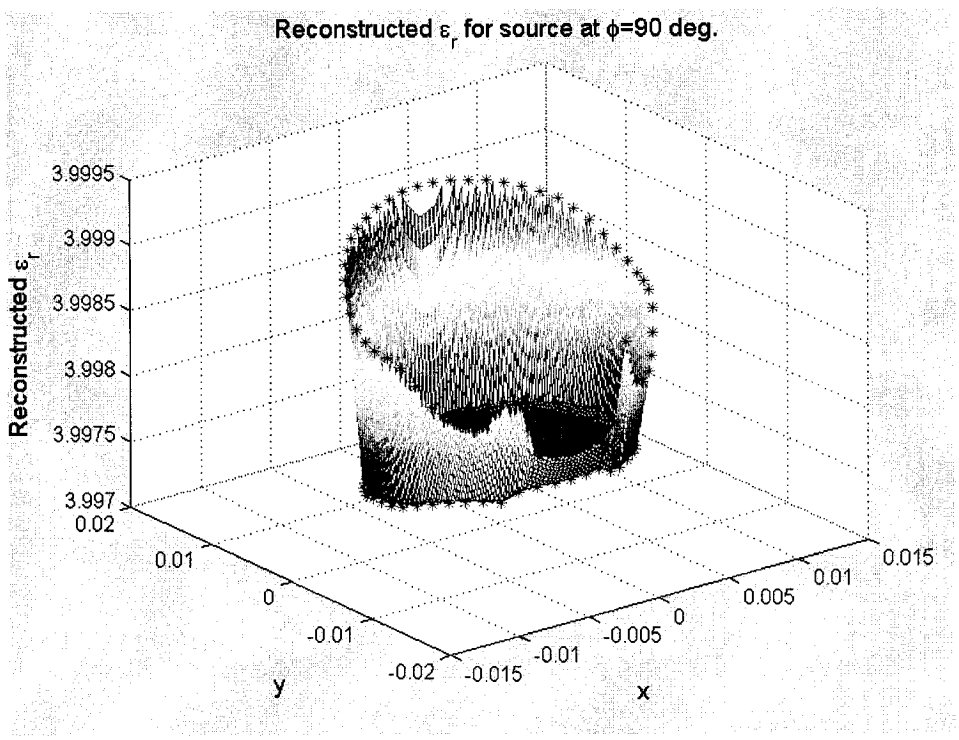

Fig.5.2 Reconstructed permittivity for source at $\phi_i = 90°$

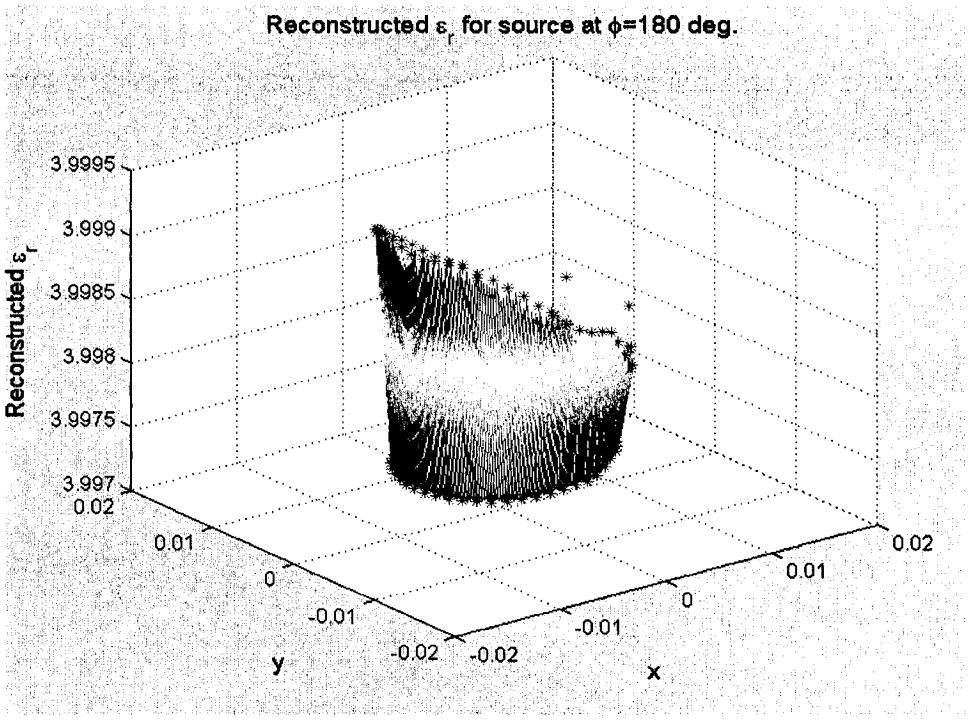

Fig.5.3 Reconstructed permittivity for source at ϕ_i =180°

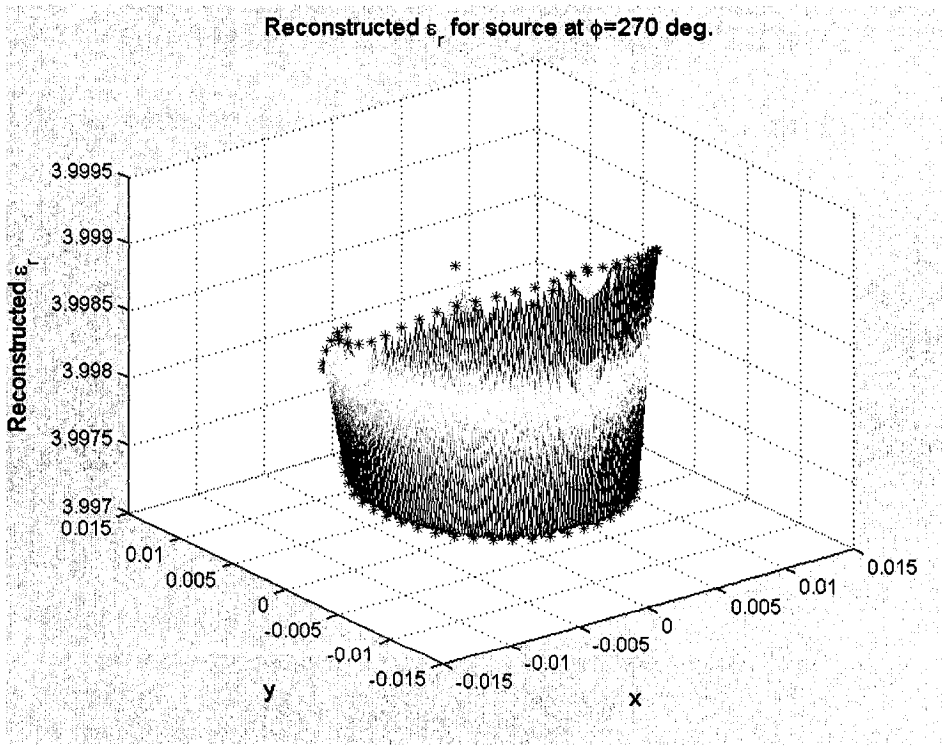

Fig.5.4 Reconstructed permittivity for source at ϕ_i =270°

Here each side of the square cell, $\Delta = \lambda/18$. The resolution in this simulation is **1.4** mm. The permittivity and conductivity profiles, that are the opposite of the source, have the better value because at the source side, the incident field and scattered field is in opposite polarity and at the opposite side of the source, the incident field and the scattered field is additive owing to having same polarity.

The error of the reconstructed permittivity and conductivity for each unrelated [54] illumination and average of illuminations is shown in Fig.5.5 and Fig.5.6 respectively. The fluctuation of the reconstructed value of permittivity and conductivity for the average of all illuminations is less than that for each unrelated illumination and average of all illuminations gives less erroneous value and more linear permittivity profile.

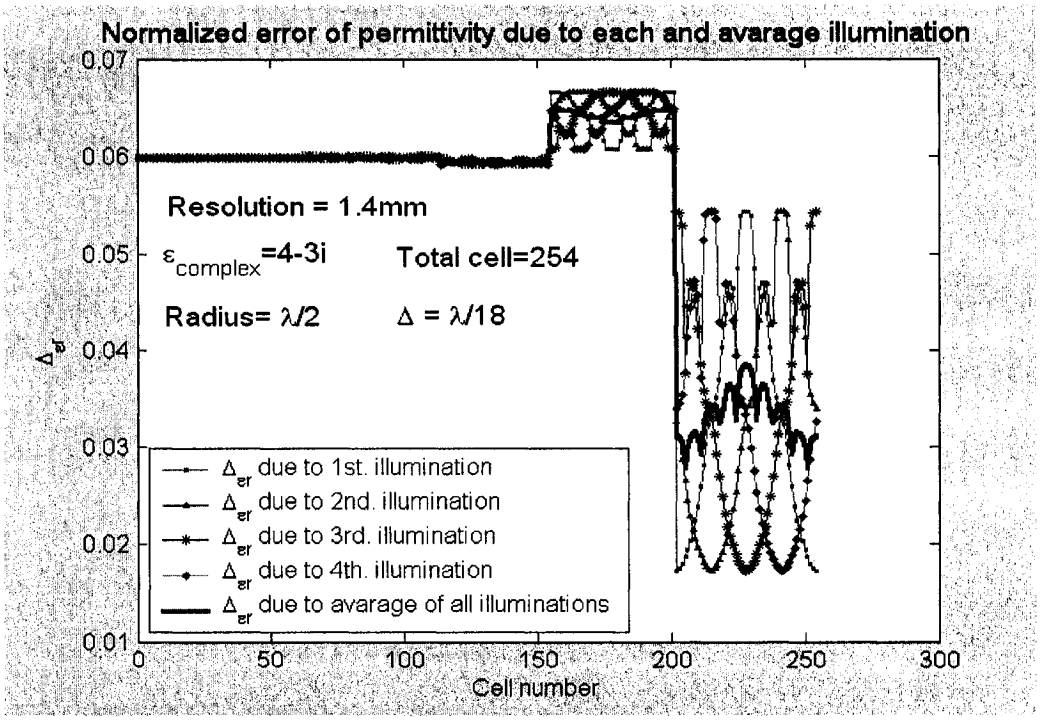

Fig.5.5 %error of reconstruction of permittivity due to each and average illumination

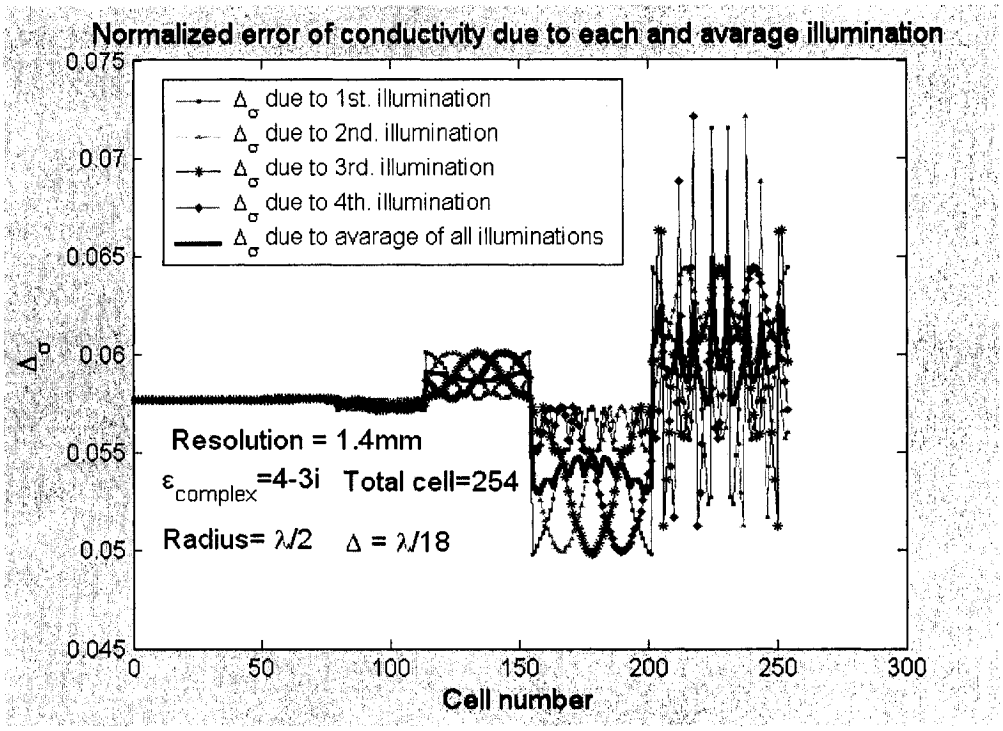

Fig.5.6 % error of reconstruction of conductivity due to each and average illumination

5.3 Effect of varying the cell size:

In this simulation, we attempt to study the effect of varying the cell size on the accuracy of the reconstruction of the relative permittivity for various scatterers. The diameter of the investigated domain of the circular cylinder is λ_0. Some researchers use ultra wideband (1-11 GHz) microwave sources [55]. Hence the operating frequency is 1GHz. This circular body is divided into 21, 61, 101 and 256 equal square cell (shown in Fig.4.4) with permittivity $\varepsilon_{\_complex} = 32 - j\ 0.8$. The cell size of the investigated circular cylinder is λ_0 /5, λ_0 /9, λ_0 /11 and λ_0 /18. Fig.5.7 shows that the smaller the cell size, the less the error and the better the reconstruction profile of dielectric permittivity for same SNR. According to [56], one important aspect in this approach is the appropriate

discretization of the surfaces. This can be done by rectangular-patches. In high frequency range, the relation between patches and wave length λ has also to be regarded as $\lambda/10$ that is suitable with respect to a highly accurate field resolution. The optimality properties may not apply for too small patches. For these cell sizes, the cell density having the value of $101/\lambda_0^2$ is optimum where as the standard cell density is $100/\lambda_0^2$ [56]. Here cell size having value of $\lambda_0/11$ gives the best linear result. But the cell size $\lambda_0/18$ gives the better result except optimum one. For all cell sizes, the relative mean square error is very low with values ranging from 0.004 to 0.02 only.

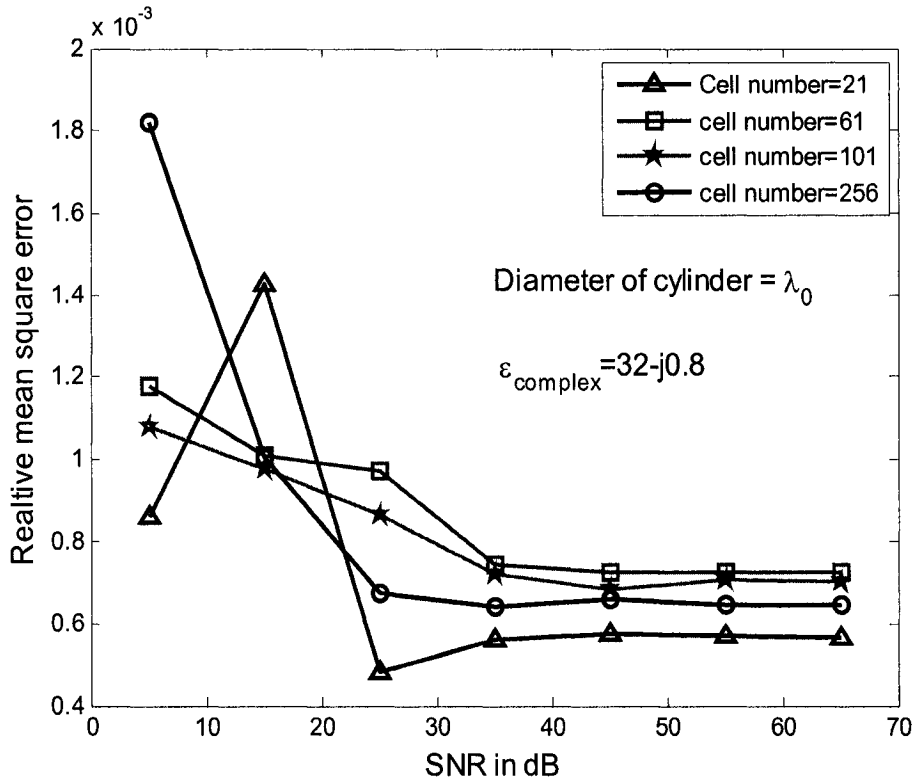

Fig.5.7 Relative mean square error of reconstructed permittivity vs. SNR for $\lambda_0/5$, $\lambda_0/9$, $\lambda_0/11$ and $\lambda_0/18$

5.4 Effect of multi contrast:

In this simulation, the multi-layered inhomogeneous scatterer (6 layers with 3 different complex permittivity distribution) to simulate a human body is illuminated by a TM incident wave in multi directions (here is 4 directions) and shown in Fig.5.8.

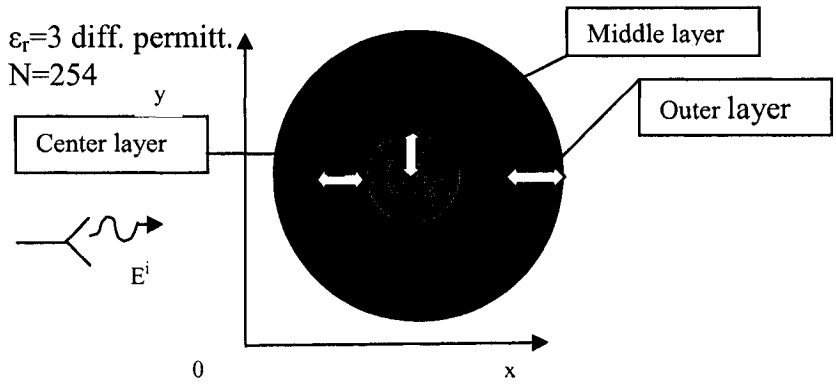

Fig.5.8 Multi contrast dielectric having 254 cells

The direction of the incident wave with x-axis is 0°, 90°, 180° and 270°. The cylindrical dielectric has 6 different layers. The center 2 layer contain the 1st scatterer having the same complex permittivity and the middle 2 layers contain the 2nd scatterer having the same permittivity and the rest of them (outer most 2 layers) contain the 3rd scatterer having the same complex permittivity. The original values of the complex permittivity of these scatterers are given in table-5.IV. For each permittivity distribution, there is a different kind of value of signal to noise ratio (SNR). Unrelated multi illumination source are used to get better-reconstructed permittivity profile. The diameter of the circular cylinder is 0.6 λ_d and the cell-size of all layers varies with its wavelength in its respective permittivity. These cells are discretized as functions of their permittivities and as well as the wavelength at the operating frequency. The operating frequency is 3GHz. The size of each cell is given in table-5. V.

	έ of 2 centre layers (cell no. 1- 12)	έ of 2 middle layer (cell no.13- 50)	έ of 2 outer most layer (cell no. 51- 113)
1st kind-complex permittivity distribution of 3 scatterers (No contrast)	$8+0.96i/\omega\varepsilon_0$	$8+0.89i/\omega\varepsilon_0$	$8+0.82i/\omega\varepsilon_0$
2nd type-complex permittivity distribution of 3 scatterers (Medium cont.)	$8+0.96i/\omega\varepsilon_0$	$28+0.89i/\omega\varepsilon_0$	$48+082i/\omega\varepsilon_0$
3rd kind-complex permittivity distribution of 3 scatterers (high contrast)	$8+0.96i/\omega\varepsilon_0$	$48+0.96i/\omega\varepsilon_0$	$88+0.82i/\omega\varepsilon_0$

Table-5.IV: Permittivity distribution of 3 different layers of the inhomogeneous dielectric object.

Cell no.		01	02	35	50	51	82	112	113
Distrib. –1 of ε_r	ε_r	8.0	8.0	8.0	8.0	8.0	8.0	8.0	8.0
	Cell size	0.0018	0.0018	0.0018	0.0018	0.0018	0.0018	0.0018	0.0018
Distrib. –2 of ε_r	ε_r	8.0	8.0	28.0	28.0	48.0	48.0	48.0	48.0
	Cell size	0.0018	0.0018	0.0009	0.0009	0.0007	0.0007	0.0007	0.0007
Distrib. –3 of ε_r	ε_r	8.0	8.0	48.0	48.0	88.0	88.0	88.0	88.0
	Cell size	0.0018	0.0018	0.0007	0.0007	0.0005	0.0005	0.0005	0.0005

Table-5.V: The cell-size of the arbitrary shape dielectric with the permittivity distribution

The resolution of this simulation varies from 1.8 mm to 0.5mm according to the permittivity of different layers. The reconstructed permittivity for each distribution of the scatterer is shown in Fig.5.9, Fig.5.11 and Fig.5.13.

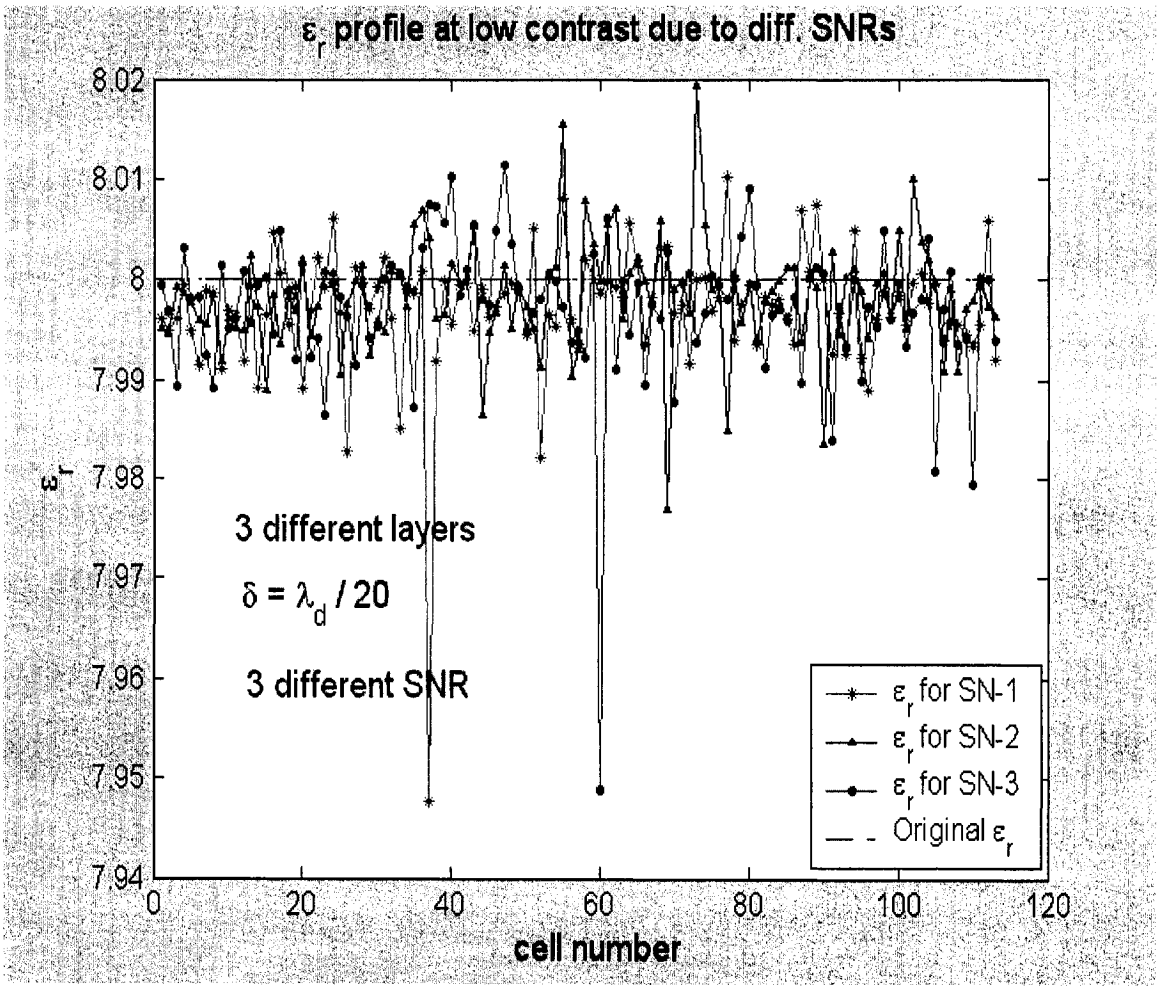

Fig.5.9 The reconstructed permittivities at low contrast for 3 SNRs

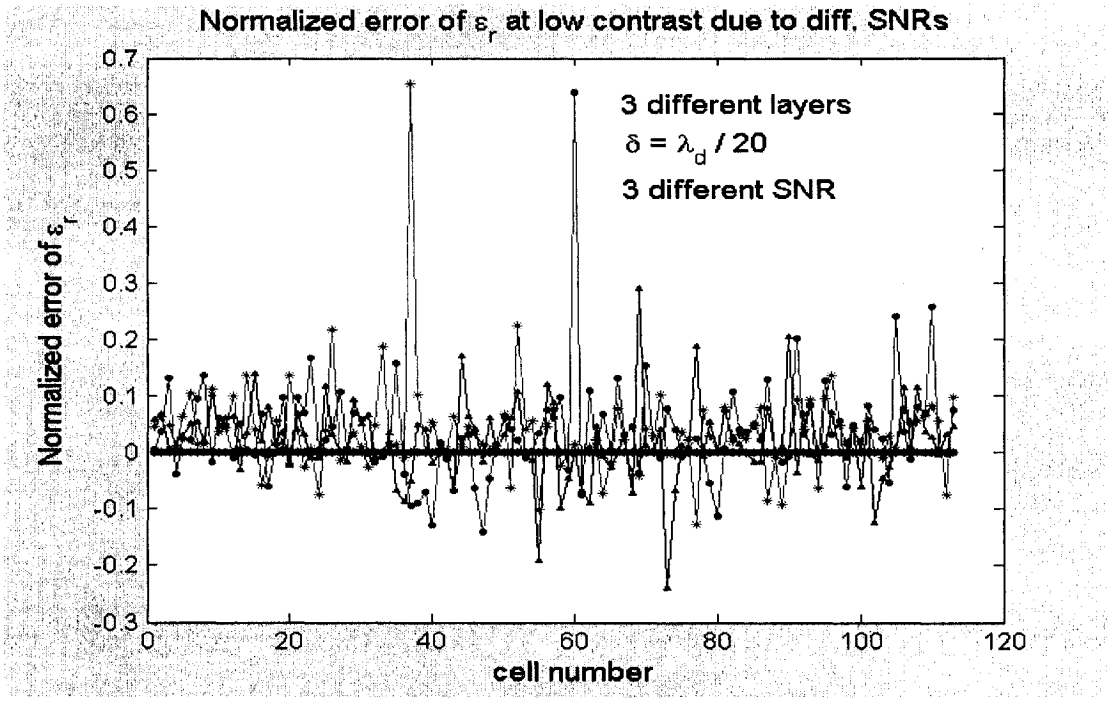

Fig.5.10 %error of permittivities at low contrast for 3 SNRs

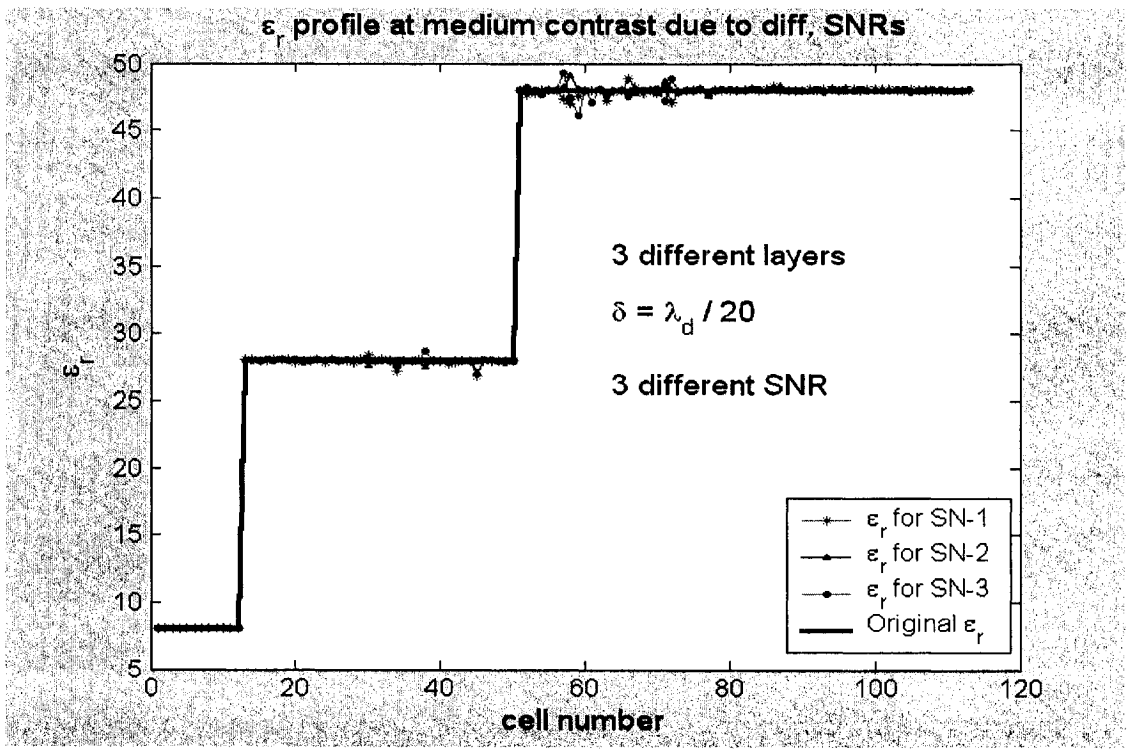

Fig.5.11 The reconstructed permittivities at medium contrast for 3 SNRs

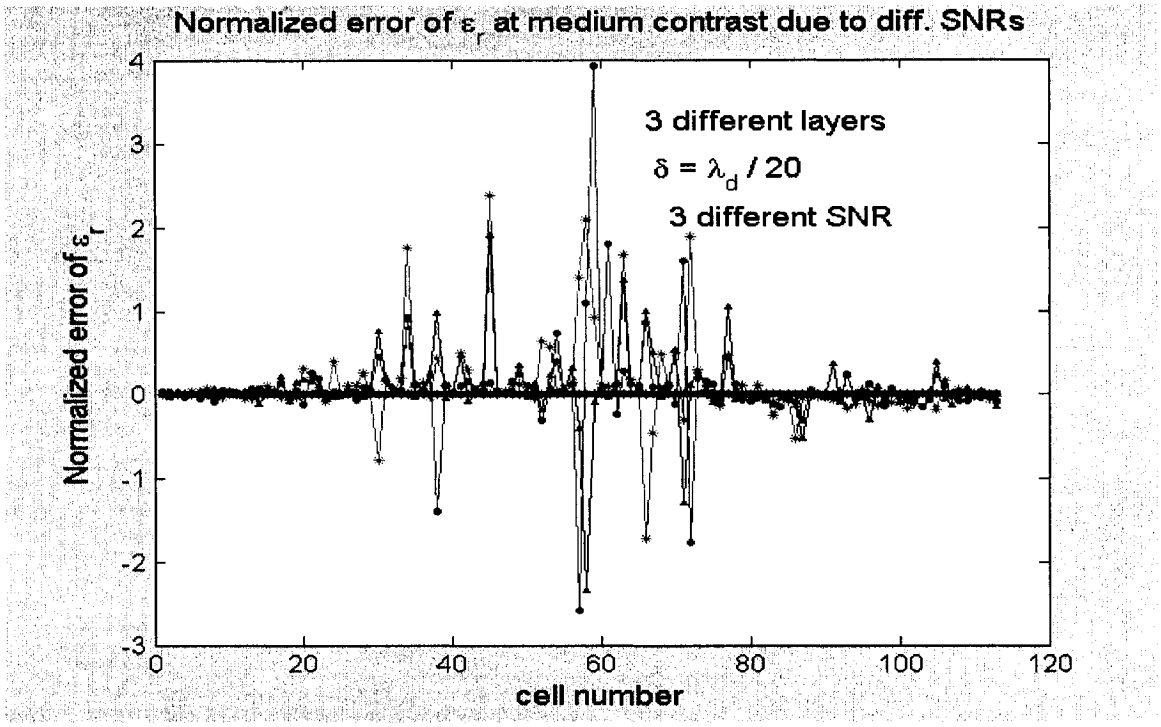

Fig.5.12 %error of permittivities at medium contrast for 3 SNRs

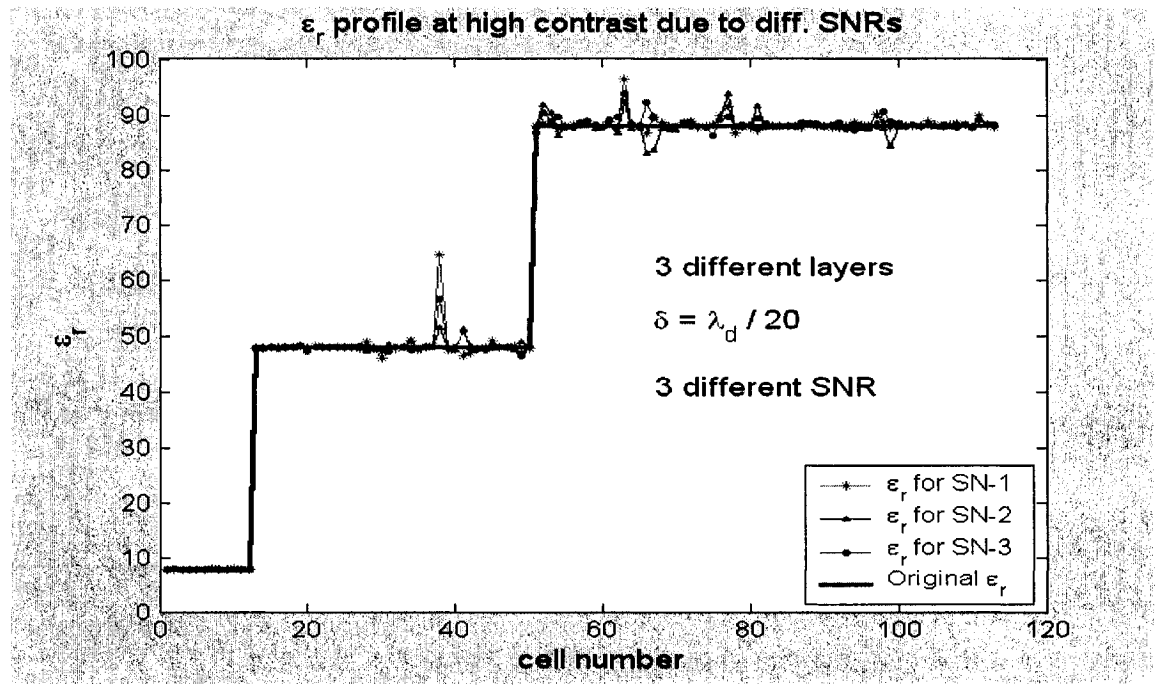

Fig.5.13 The reconstructed permittivities at high contrast for 3 SNRs

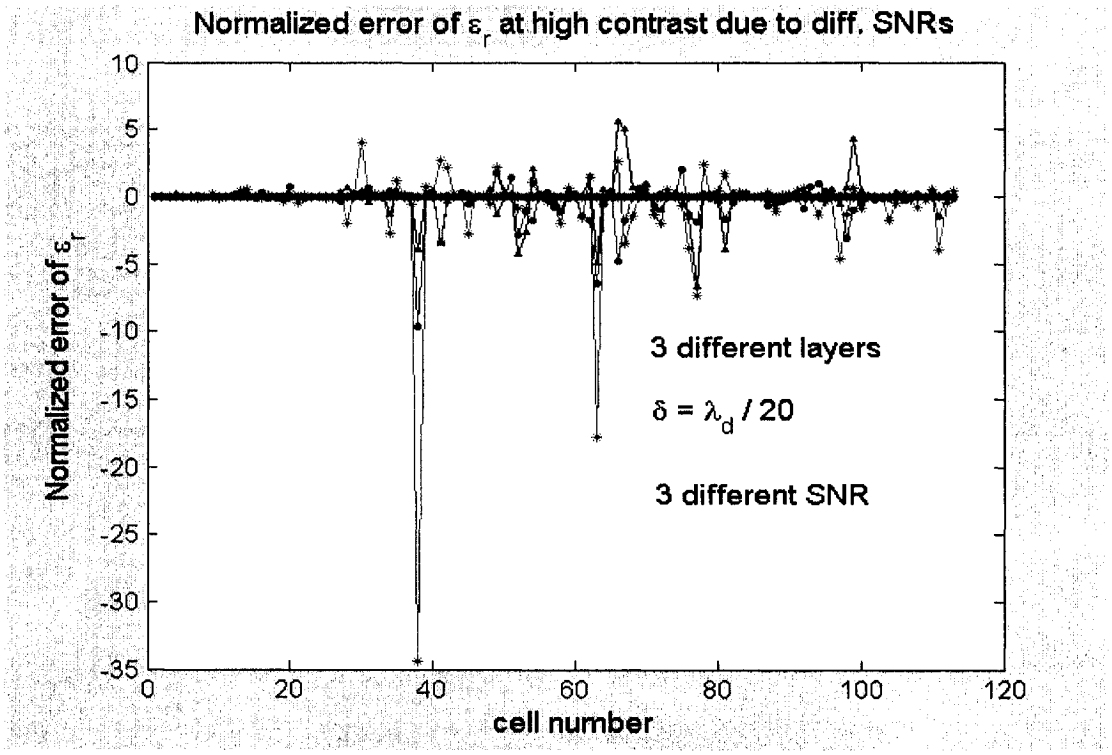

Fig.5.14 %error of permittivities at high contrast for 3 SNRs

It is seen from Fig.5.9, 5.11 and 5.13 that the reconstructed permittivities for 3 different SNRs have excellent agreement among themselves and with the original value of the permittivity. The normalized errors of these reconstructed permittivities reported in Fig.5.10, 5.12 and 5.14 are only ±0.2%, ±2% and ±4% except some spiky points.

At low contrast, the reconstructed permittivity profile achieved from different types of the numerical simulation presents itself to be quite promising but at high contrast the normalized error of the reconstructed permittivity is high with respect to that error of the permittivity got from low contrast. It is undoughty said that the error of the reconstructed permittivity at high contrast is very low with respect to the original value of the permittivity. It is concluded that the reconstructed permittivity is tremendously promising at all contrasts.

5.5 Effect of varying the strength of scatterers:

In this simulation, three scatterers are investigated, the first scatterer has $\varepsilon_r = 8$, the second has $\varepsilon_r = 32$ and the third has $\varepsilon_r = 56$. The simulation is carried out for 2mm x 2mm square, which is divided into 113 square cells of the circular homogeneous dielectric cylinder having diameter $0.6\lambda_d$ at 1GHz. The resolution of this simulation is very high. Fig.5.15, Fig.5.16 and Fig.5.17 show the normalized error in the reconstruction of the dielectric permittivity for these scatterers at noisy environment having 3(three) different noise distributions: 15dB, 20 dB and 25 dB. Fig.5.18 shows the normalized error in the reconstruction of the dielectric permittivity for these scatterers at noiseless environment. It is said from these figures of this simulation that the normalized error of the strong scatterer is high compared to weak scatterer at all SNRs or for noise free simulation. It is concluded that strong scatterer produces more the error of the reconstructed profile.

For noise distribution-1, distribution-2 and distribution-3, the normalized error of the reconstructed permittivity for 3(three) scatterers is approximately ±0.2%, ±0.15%, and ±0.12% respectively. These are very small with respect to their original values. But in the case of a noise free simulation, the reconstruction error of the 3(three) scatteres is ranging from 0.04 to .085. So the reconstruction of permittivity (weak or strong) of the homogeneous dielectric at either noisy environment or noise free environment is more accurate. From the above simulations, it is said that the error of the reconstruction is minimum at high SNR.

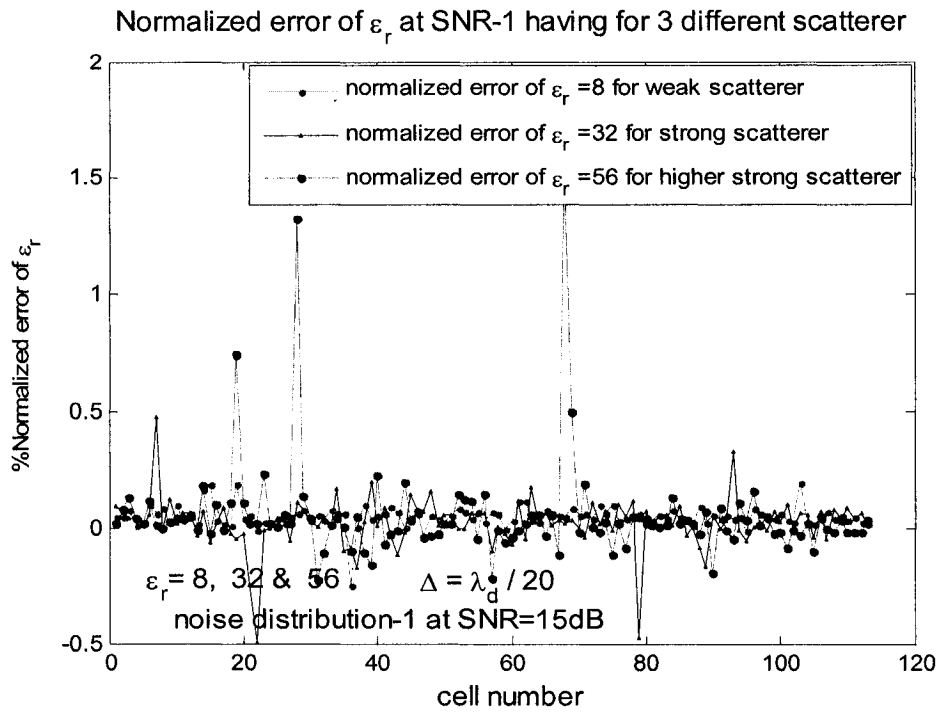

Fig.5.15 Normalized error of 3(three) scatterers at noise distribution-1

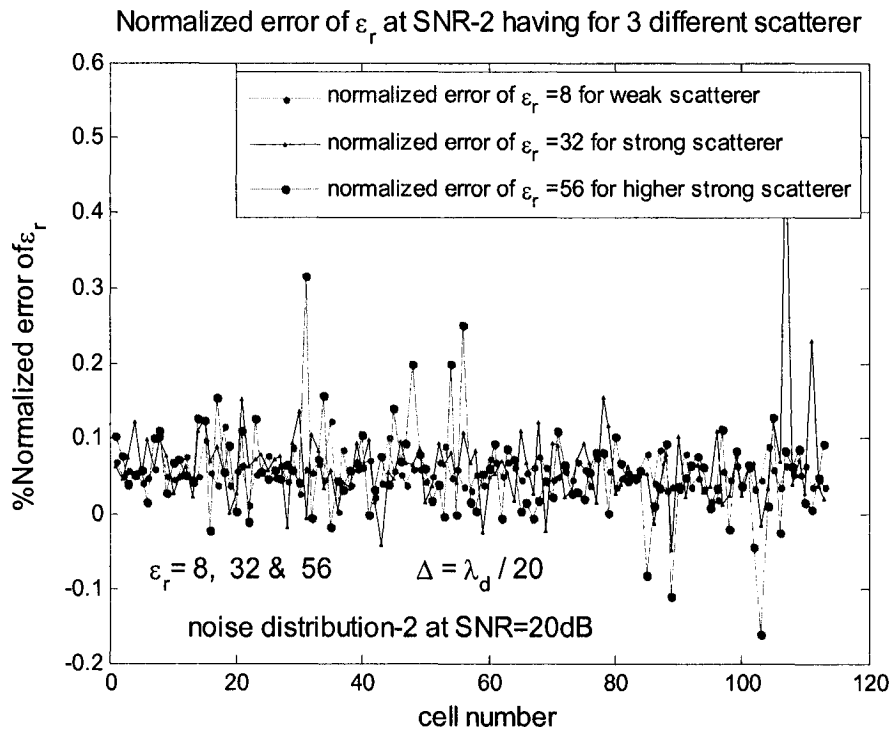

Fig.5.16 Normalized error of 3(three) scatterers at noise distribution-2

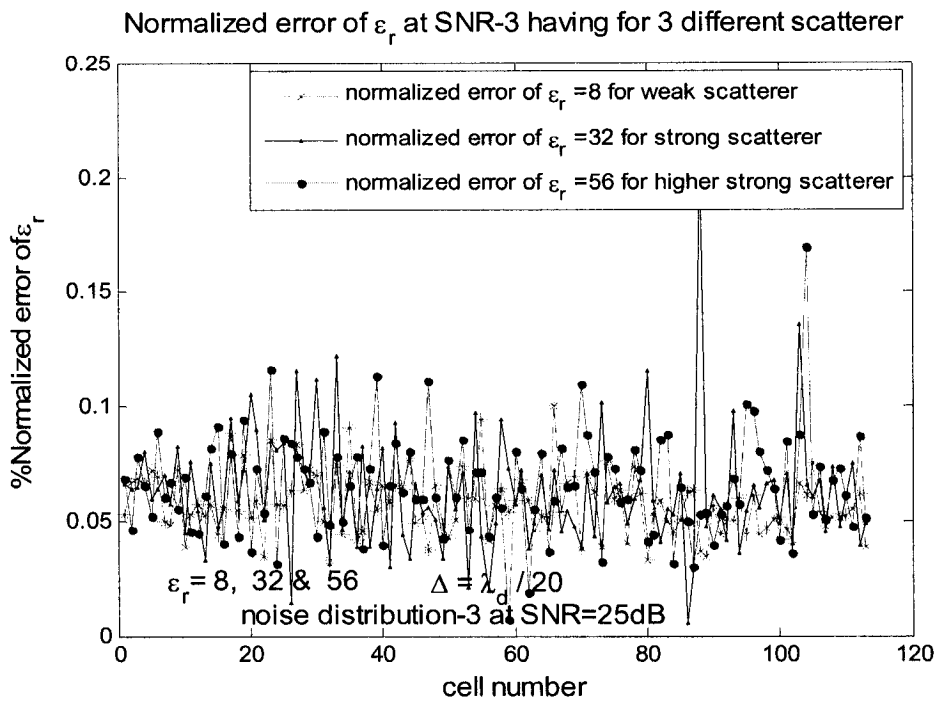

Fig.5.17 Normalized error of 3(three) scatterers at noise distribution-3

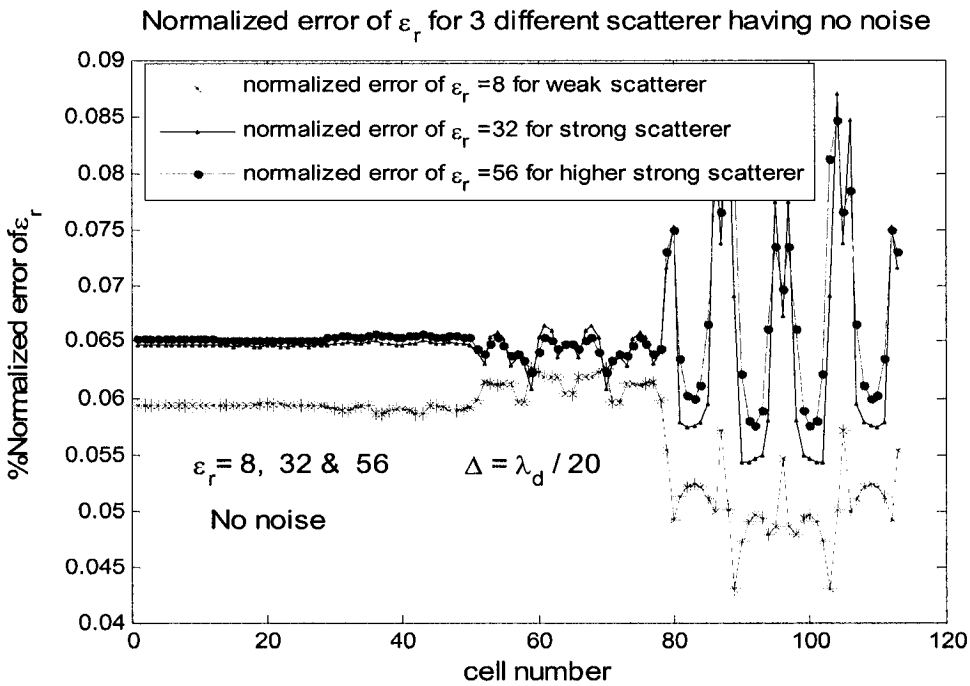

Fig.5.18 Normalized error of 3(three) scatterers due to noise free simulation

5.6 Effect of varying operating frequency:

In each simulation, the dielectric properties of the scatterer are kept constant for the three frequencies studied such as 300MHz, 900MHz and 1.5GHz. Two types of scatterer having ε_r of 8 and 32 and σ of 0.96s/m are used in this simulation. The size of the discretized square cell is $\lambda_d/20$ in each simulation. Fig.5.19, Fig.5.20 and Fig.5.21 show the relative mean square error in the reconstructed relative dielectric permittivity and conductivity at the above frequencies. As shown, the error in the reconstruction increases with increasing the operating frequency for the relative permittivity but vice versa for the conductivity the error in the reconstruction increases with increasing the operating frequency for the relative permittivity but vice versa for the conductivity. The reason for this increase is that the incident matrix is not totally diagonally dominant. This is mainly because as the frequency increases, the physical size of the array, that produces the plane electric wave, decreases. This in turn decreases the beam width of the incident wave. Thus, the incident field is not totally focused on the desired cell of the circular dielectric cylinder. For the conductivity, this is a different scenario. If the dielectric scatterer is lossless then due to numerical simulations there are few conductive effects added to the reconstruction process. This is the cause that the error of the reconstructed conductivity is always higher than that of the relative permittivity in all simulations. Due to this reason, the conductivity does not behave like the permittivity for relative mean square errors. From the figures, the relative mean square error of $\varepsilon_r = 8$ for all frequencies

at all SNRs is ranging from 0.06% to 0.11% where as this error of $\varepsilon_r = 32$ is ranging from 0.08% to 0.18%. On the other hand for the conductivity, this error is ranging from 0.1% to 0.8% at all frequencies and at all SNRs. The reconstructed error of the two scatterers at all mentioned frequencies and at all mentioned SNRs is acceptable for the relative permittivity as well as the conductivity.

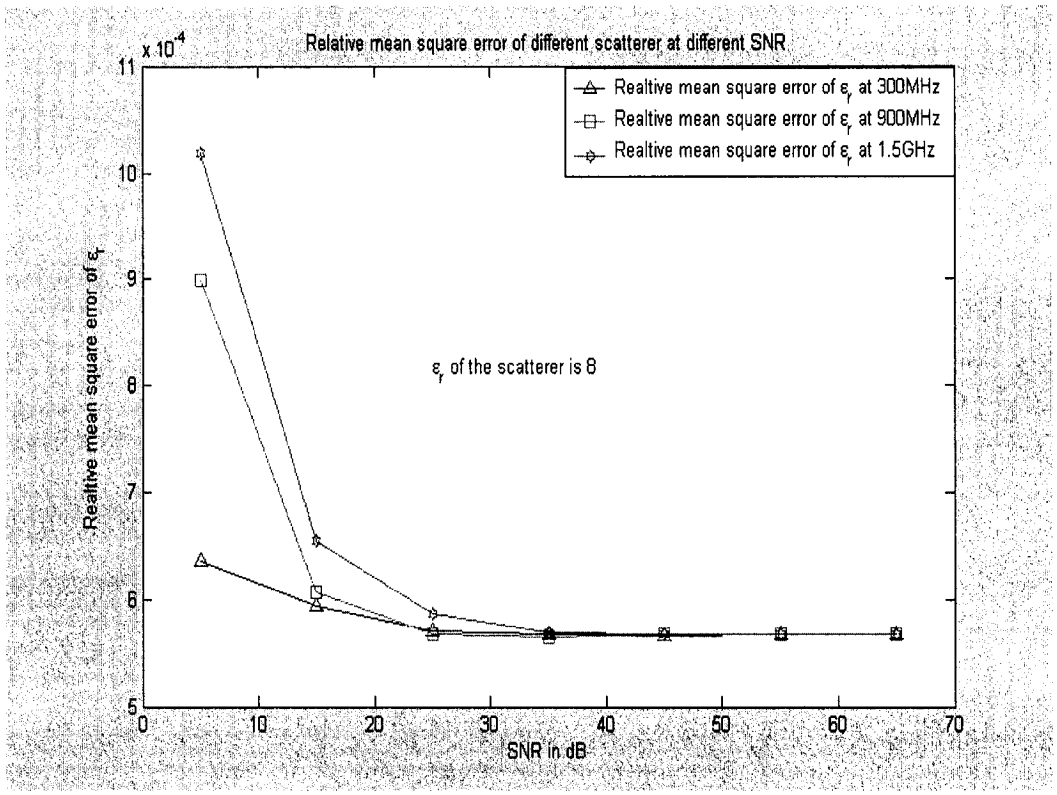

Fig.5.19 Relative mean square error of the reconstructed relative permittivity for $\varepsilon_r = 8$ at 3 frequencies

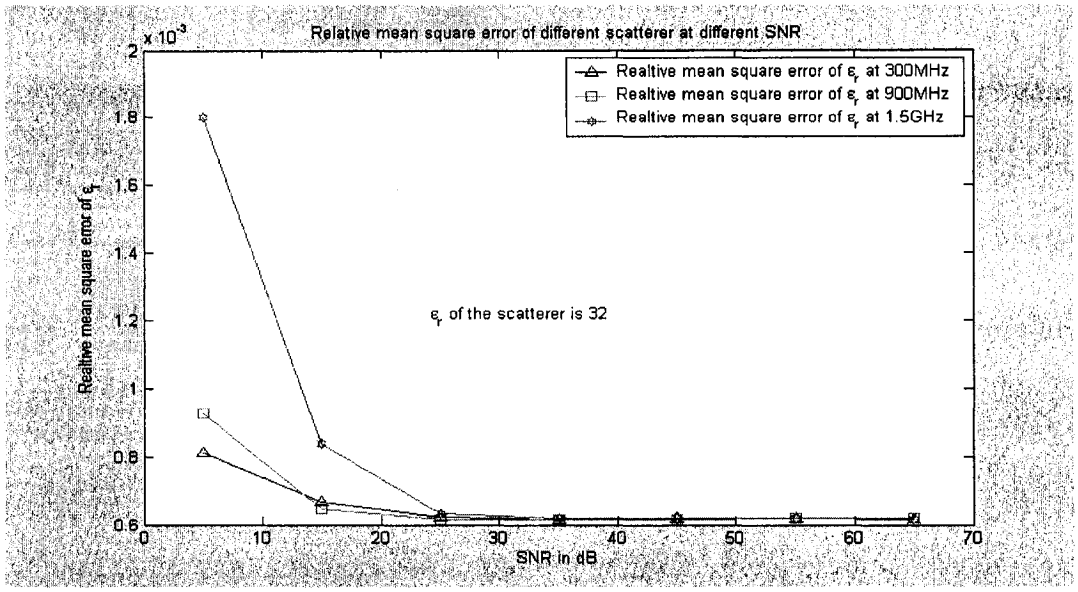

Fig.5.20 Relative mean square error in the reconstructed relative permittivity for $\varepsilon_r = 32$ at 3 frequencies

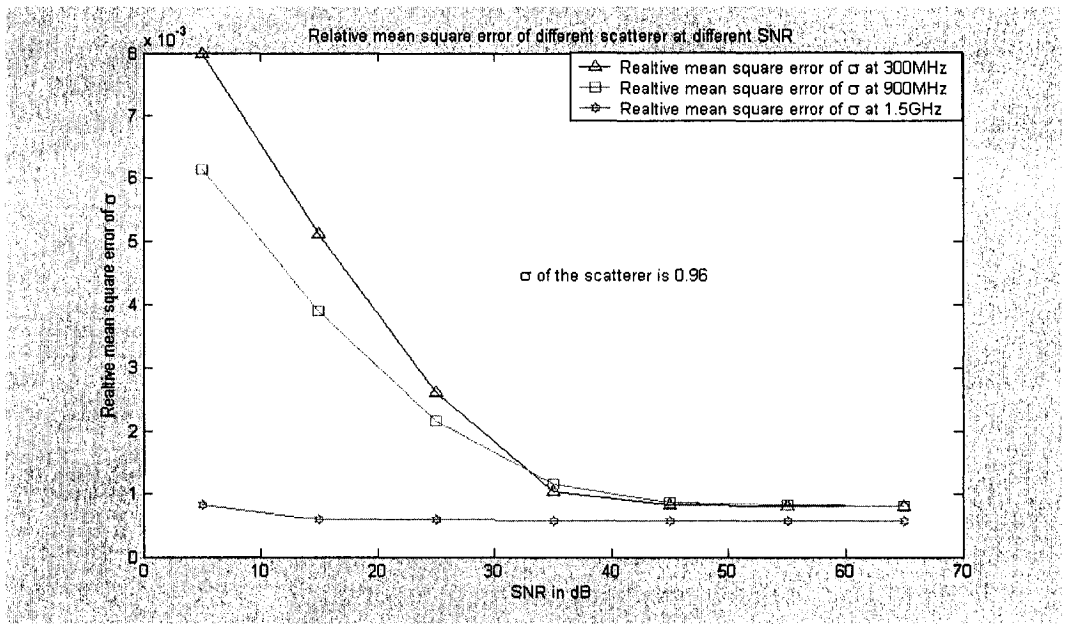

Fig.5.21 Relative mean square error in the reconstructed conductivity at 3 frequencies

5.7 Reconstruction of scatterer using TE case:

Again, the dielectric material is assumed to be linear and isotropic but it is inhomogeneous with respect to the transverse coordinate i.e. $\varepsilon = \varepsilon(x, y)$. The investigated circular cylindrical dielectric has 5 layers having 3 different permittivity distributions for different contrast as shown in table-5.VI.

Three (3) ε-distributions including layer number	Very low contrast E-distribution	Medium contrast ε-distribution	High contrast ε-distribution
Inner ε (layer-1)	8.82 + 0.82i	48.82 + 0.82i	88.82 + 0.82i
Middle ε (layer-2,3)	8.82+0.89i	28.82+0.89i	48.82+0.89i
Outer ε (layer-4, 5)	8.82+0.96i	8.82+0.96i	8.82+0.96i

Table-5.VI: Permittivity distribution with 3 contrasts for 3 simulations.

The cell size of this example is $\lambda_d/20$. Each cell-size depends on the operating frequency and the permittivity of each cell. The reconstructed permittivity and conductivity at 6GHz due to low contrast and high contrast are shown in Fig.5.22 and 5.53 respectively. The percentage of normalized error of the reconstructed permittivity is ranging from 1×10^{-12} to -6×10^{-12} for all simulations. These errors are very small. The reconstructed conductivity at 6GHz due to low contrast and high contrast are shown in Fig.5.24 and 5.25. The percentage of normalized error of the reconstructed conductivity is ranging from 15×10^{-11} to -20×10^{-11} for all simulations. These errors are also very small. Though the TE case provides accurate results but this method requires two times CPU memory of and running time for the same size of the dielectric object of arbitrary shape. This is a disadvantage of TE case.

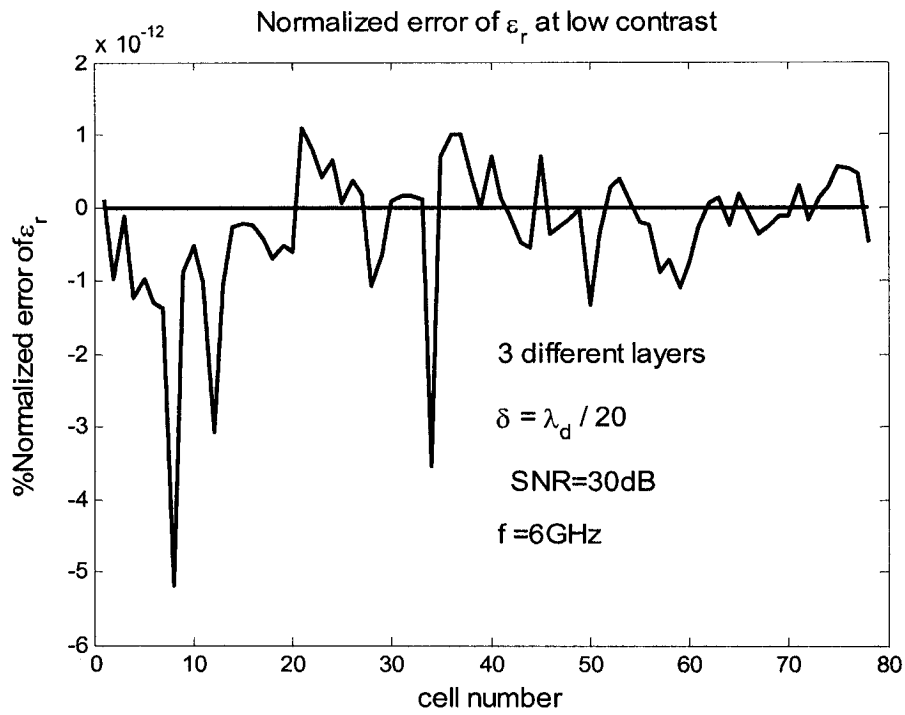

Fig.5.22 %error of reconstructed permittivity at 6GHz for low contrast

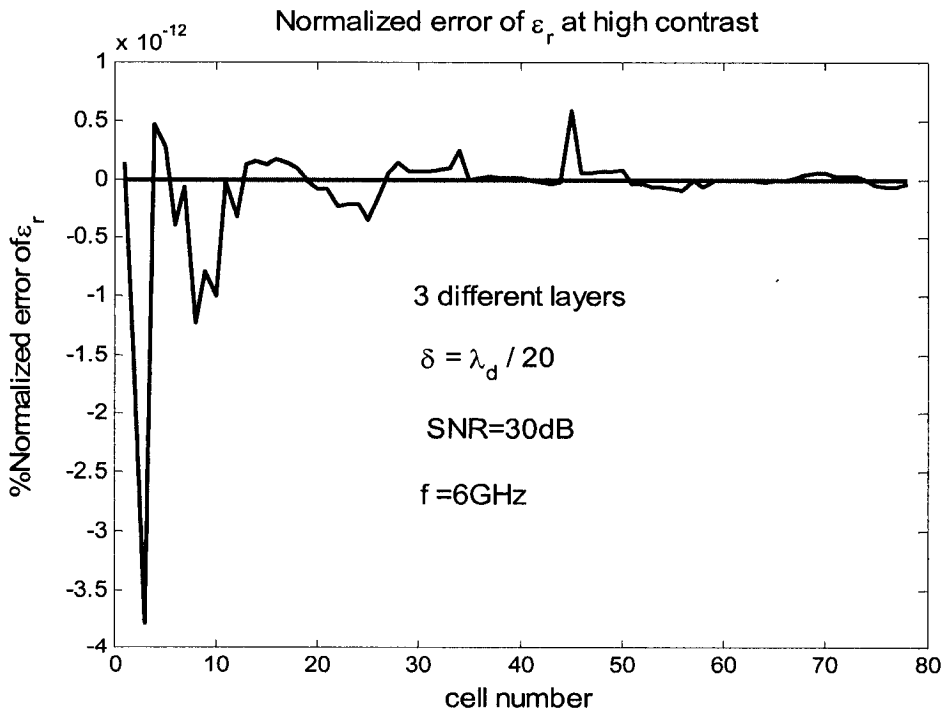

Fig.5.23 %error of simulated permittivity at 6GHz for high contrast

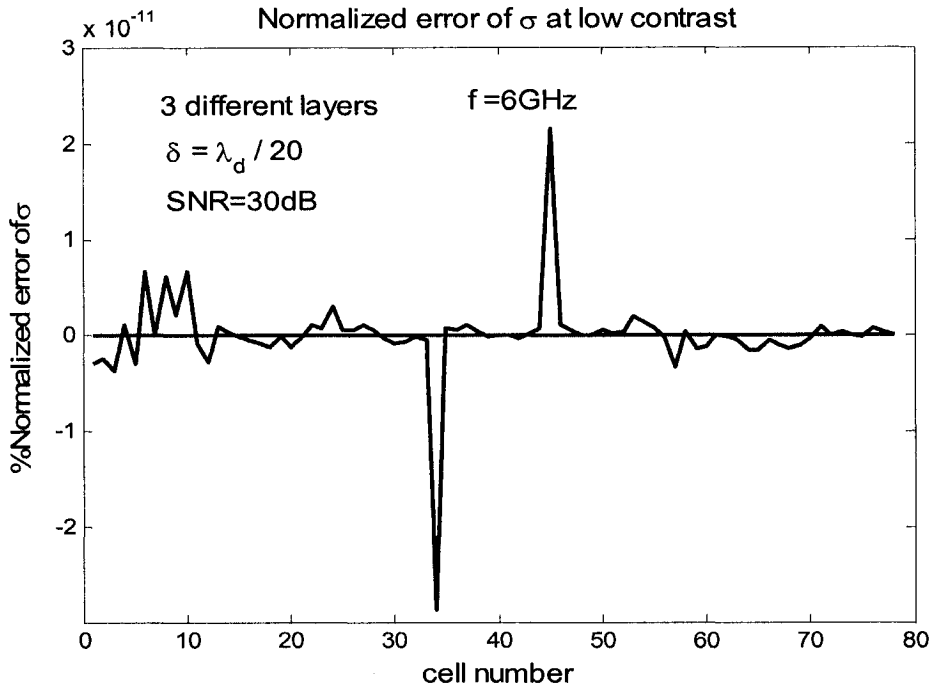

Fig.5.24 %error of reconstructed conductivity at 6GHz for low contrast

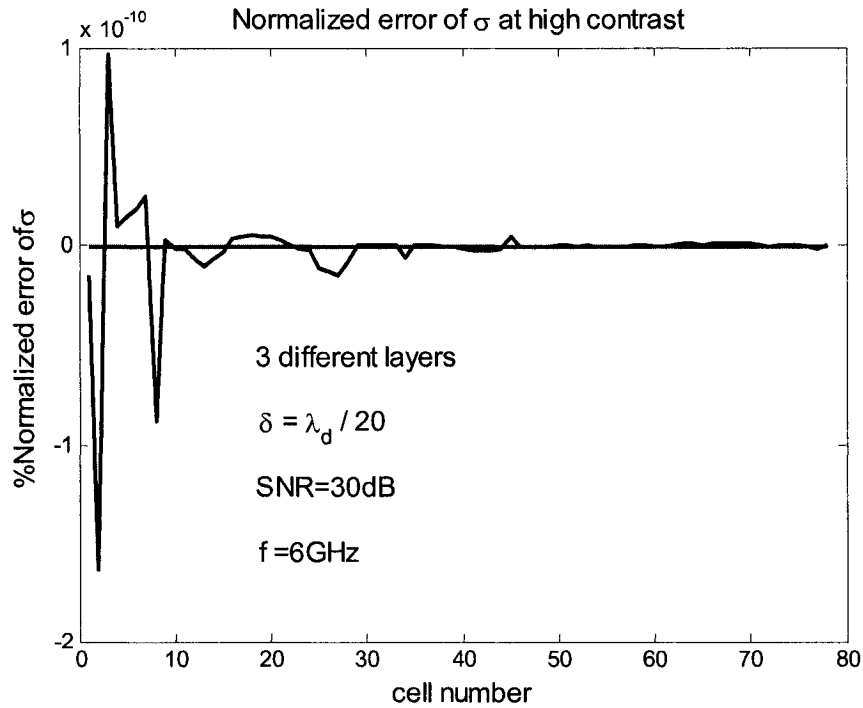

Fig.5.25 %error of simulated conductivity at 6GHz for high contrast

CHAPTER 6

Conclusion

6.1 Conclusion:

In this thesis, we have attempted to study different aspects of interaction of electromagnetic waves with 2D arbitrary shaped objects of complex dielectric permittivity. Mainly, two types of dielectric objects were investigated. The first is a homogeneous dielectric object to study forward scattering of electromagnetic waves. The other is a layered inhomogeneous dielectric object to study both forward and inverse scattering of electromagnetic waves. The total and the scattered fields are measured due to the interaction of a known incident field with the dielectric body in the forward scattering while in the inverse scattering, the complex permittivity profiles have been reconstructed from the known scattered field. The scattering electric field is directly related to the permittivity and conductivity of the dielectric body. Pseudoinverse algorithm and Born approximation method have been used to obtain the scattered field and to reconstruct the complex permittivity profile. The method utilizes the method of moment (MoM) to discretize the nonlinear integral equation, which relates the scattered field data and the complex permittivity distribution of the body. It is a frequency domain technique. Both numerical methods are used to investigate single and multi layer dielectric scatterers excited by either TM or TE polarized electromagnetic plan wave. Circular layered square discretization technique is introduced and used thorough out this thesis. This discretization gives more degree of linear values of the reconstructed profile

of the complex permittivity than the conventional square discretization of [13].

To investigate the possibility of the reconstruction of the arbitrary shaped dielectric bodies from the near scattered field data, the unrelated illumination method has been used. Using the Pseudoinverse algorithm and Galerkin's method, the result is a system of linear equation in a matrix form with unknown expansion coefficients. Through performing some simple matrix operations, the scattered field as well as the permittivity distribution profile have been computed numerically.

The total field due to the interaction of the known incident electromagnetic wave with the investigated dielectric domain in the forward scattering problem is validated with results reported in [12]. The numerical results agree well with the published results. Also, the numerical solution agrees well with the exact analytical solution for the circular cylinder case. This numerical technique involves calculation over discrete values.

In both the forward and inverse scattering parts of the proposed method, the reconstructed permittivity profile is also validated by comparing the numerical results of the simulation to the results published in [13]. Due to using different algorithms and discretization techniques, there is a little difference in the magnitude of the permittivity but the computed results are better than those of [13]. The relative mean square error at all positions of the scatterer follows similar pattern as in [13].

The possibility of determining the location of scatterer with the error of the reconstruction in the investigated domain is compared to the results reported in [13]. The determination of the location of the scatterer in the investigated domain is most important for surgical operation purpose. The determination of location of the scatterer has excellent accuracy. Meanwhile, as mentioned earlier, the proposed method gives less

erroneous value of the reconstructed permittivity.

The proposed method of reconstruction of the permittivity profile is compared to that of the 'Born Approximation' for weak scatterers. The error of reconstruction of the permittivity profile increases as the value of the permittivity increases. The error of the reconstruction of the conductivity follows the same pattern with same magnitude for both methods.

Finally, the uncertainty of the proposed method is measured to satisfy the boundary condition at the circumference of the cross section of the scatterer where the known incident field and simulated total field minus simulated scattered field is exactly the same on the boundary.

In the simulation, the direction of the incident electric field affects the reconstruction of the complex permittivity profile of the investigated dielectric object. The permittivity and conductivity profiles on the opposite of the source have more accurate value than the other portion of the object. Because the incident field and scattered field are in opposite polarity at the source side and the incident field and the scattered field are additive owing to having same polarity at the opposite side of the source. As a result, multi illuminations by a group of unrelated [54] electromagnetic wave give better accurate results of the reconstructed complex permittivity and more linear profile with respect to single illumination.

The value of the reconstructed complex permittivity varies with the discretized cell size. Generally, the smaller the cell size, the less the error and the better the reconstruction profile of dielectric permittivity for same SNR but there is an optimum value of discretized cell size: λ_0 /11. In a noiseless simulation, the fluctuation of the

value of reconstructed permittivity is negligible irrespective of the complex permittivity distribution at all cell sizes.

It has been shown that this method is well capable to handle multi contrast inhomogeneous scatterer (either low or high contrast) with a low error of reconstruction for the permittivity and with acceptable error of reconstruction for the conductivity due to a very high contrast at realistic measurement condition i.e. at noise.

To show the strength of this method, weak and very strong scatterers are considered and simulated. It is noticed from simulations that the relative mean square error of high scatterer is high compared to low scatterer at all SNR. The error of the reconstruction of the permittivity profile is small at high SNR compared to low SNR for all scaterers. It is shown that the error of reconstruction is very low at various SNR for each scatterer. Multi frequency effect is also considered in simulations where the relative mean square error of the reconstruction increases as the frequency increases.

The above simulations are carried out for the TM case only. This method is also capable to handle TE case. In simulations for the TE case, the error of reconstruction is also low but this method requires two times CPU memory and running time for the same size of the dielectric object. This is a disadvantage for the TE case.

6.2 Future Research

In this thesis, only two-dimensional scatterer is investigated and the interaction of electromagnetic scattering with various types of scatterer has been studied. Yet, research can still be done for three-dimensional scatterers. Also, research can be carried out to design the antenna array that can be used as a transmitter and receiver simultaneously. All simulations are done theoretically. The whole procedure should then be tested against measured data.

Array of slotted antenna can be made on the hollow cylinder having fixed radius. Antenna array can be excited in either TM or TE mode to generate the incident field. The human body goes through the cylinder at fixed speed to reconstruct three-dimensional microwave image with fixed resolution. Design of this type of medical instrument could also be done to reconstruct the permittivity distribution profile of the human body. The reconstructed permittivity profile makes a key role in diagnosing the cancer of human body at early stage.

APPENDIX A

Matrix Formulation of Total Field

Let $\vec{E}$ represent the total field; that is, the field set up by the source in the presence of the dielectric cylinder .The scattered field is defined to be the difference between the total and incident fields. Thus,

$$\vec{E} = \vec{E}^i + \vec{E}^s \tag{A. 1}$$

$\vec{E}^i$ and $\vec{E}^s$ represent the incident field and scattered field respectively.

Under the assumed conditions, the total and the scattered electric field intensities will have only z components. The field of an electric current filament dI parallel with the z-axis in free space is given by,

$$d\vec{E}^s = -\hat{z}(\omega\mu/4)H_0^{(2)}(k_0\rho)dI \tag{A. 2}$$

Where $H_0^{(2)}(k_0\rho)$ is the Hankel function of order zero, ρ is the distance from the current filament to the observation point and $k_0 = \omega\sqrt{\mu_0\varepsilon_0} = 2\pi/\lambda_0$. The free space wavelength is given by λ_0.

The increment of electric current which generates the scattered field, is given by

$$d\vec{I} = \vec{J}dS = j\omega(\varepsilon - \varepsilon_0)\vec{E}dS \tag{A. 3}$$

Where dS is the increment of surface area on the cross section of the dielectric cylinder. From (A.2) and (A.3), the scattered field is given by

$$\vec{E}^s(x,y) = -(jk_0^2/4)\iint(\varepsilon_r - 1)\vec{E}(x',y')H_0^{(2)}(k_0\rho)dx'dy'$$

$$= -(jk_0^2/4)\iint\frac{\vec{J}(x',y')}{j\omega\varepsilon_0}H_0^{(2)}(k_0\rho)dx'dy' \qquad (A.4)$$

where (x, y) and (x', y') are the coordinates of the observation point and the source point , respectively , ε_r is the complex relative dielectric constant ($\varepsilon_r = \varepsilon/\varepsilon_0$) and

$$\rho = \sqrt{(x-x')^2 + (y-y')^2} \qquad (A.5)$$

The integration in (A.4) is to be performed over the cross section of the dielectric cylinder. Equation (A.4) is valid for the scattered field at any point inside or outside the dielectric region. The integral equation for the total field $\vec{E}$ is obtained from (A.1) and (A.4) .

$$\vec{E}(x,y) + (jk_0^2/4)\iint(\varepsilon_r - 1)\vec{E}(x',y')H_0^{(2)}(k_0\rho)dx'dy'$$

$$= \vec{E}(x,y) + \frac{\omega\mu_0}{4}\iint\vec{J}(x',y')H_0^{(2)}(k_0\rho)dx'dy' = \vec{E}^i(x,y) \qquad (A.6)$$

Let us divide the cross section of the dielectric cylinder into cells sufficiently small so that the dielectric constant and the electric field intensity are essentially constant over each cell. If (A.6) & (A.4) is enforced at the center of cell m , the following expression is obtained

$$\vec{E}_m + (jk_0^2/4)\sum_{n=1}^{N}(\varepsilon_n - 1)\vec{E}_n\iint_{cell\,n} H_0^{(2)}(k_0\rho_{mn})dx'dy' = \vec{E}_m^{\,i} \qquad (A.7)$$

By taking m = 1,2,3, ...N, equation (A.7) yields a system of N linear equations, where N represents the total number of cells.

The surface integral in (A.7) can be evaluated by Method of Moment technique. Using

Dirac delta both for basis function and testing function (Galerkin's method), one can avoid the number of integrations required. Care must be exercised in integrating through the singularity that exists when the observation point is at the center of cell n. The region of integration (over cell n) is square of rectangular in the simplest case, and the closed form solution for this integral is not known. A simple solution is however available for the integral of the zero-order Hankel function over a circular region.

The system of linear equations (A.7) can be written in the following form using the solution for the integral of the zero-order Hankel function over a circular region:

$$\vec{E}_m + \sum_{n=1}^{N} (\varepsilon_n - 1)\vec{E}_n (j/2)\left[\pi \mathrm{K}_0 a \mathrm{H}_1^2 (\mathrm{K}_0 a) - 2j\right] = \vec{E}_m{}^i \quad if \quad m = n \qquad (A.7.a)$$

$$\sum_{n=1}^{N} (\varepsilon_n - 1)\vec{E}_n (j\pi \mathrm{K}_0 a/2) J_1 (\mathrm{K}_0 a) \mathrm{H}_0^{(2)} (\mathrm{K}_0 \rho_{mn}) = \vec{E}_m{}^i \quad if \quad m \neq n \qquad (A.7.b)$$

Putting m=1,2,3,.....N in eq.-(A.7.a) and (A.7.b).

For $m = 1$;

$$\vec{E}_1 + (\varepsilon_1 - 1)\vec{E}_1 \frac{jk_0^2}{4} \iint_{cell=1} \mathrm{H}_0^{(2)} (\mathrm{K}_0 \rho_{11}) \partial x' \partial y' + (\varepsilon_2 - 1)\vec{E}_2 \frac{jk_0^2}{4} \iint_{cell=2} \mathrm{H}_0^{(2)} (\mathrm{K}_0 \rho_{12}) \partial x' \partial y' + (\varepsilon_3 - 1)\vec{E}_3$$

$$\frac{jk_0^2}{4} \iint_{cell=3} \mathrm{H}_0^{(2)} (\mathrm{K}_0 \rho_{13}) \partial x' \partial y' + (\varepsilon_4 - 1)\vec{E}_4 \frac{jk_0^2}{4} \iint_{cell=4} \mathrm{H}_0^{(2)} (\mathrm{K}_0 \rho_{14}) \partial x' \partial y' + ...$$

$$+(\varepsilon_N - 1)\vec{E}_N \frac{jk_0^2}{4} \iint_{cell=N} \mathrm{H}_0^{(2)} (\mathrm{K}_0 \rho_{1N}) \partial x' \partial y' = \vec{E}_1^i$$

or, For $m = 1$;

$$\vec{E}_1 [1 + (\varepsilon_1 - 1)\frac{j}{2}\{\pi k_0 a \mathrm{H}_1^2 (k_0 a) - 2j\}] + (\varepsilon_2 - 1)\vec{E}_2 \frac{jk_0^2}{4} \iint_{cell=2} \mathrm{H}_0^{(2)} (\mathrm{K}_0 \rho_{12}) \partial x' \partial y' + (\varepsilon_3 - 1)\vec{E}_3$$

$$\frac{jk_0^2}{4} \iint_{cell=3} \mathrm{H}_0^{(2)} (\mathrm{K}_0 \rho_{13}) \partial x' \partial y' + (\varepsilon_4 - 1)\vec{E}_4 \frac{jk_0^2}{4} \iint_{cell=4} \mathrm{H}_0^{(2)} (\mathrm{K}_0 \rho_{14}) \partial x' \partial y' + ...$$

$$+(\varepsilon_N - 1)\vec{E}_N \frac{jk_0^2}{4} \iint_{cell=N} \mathrm{H}_0^{(2)} (\mathrm{K}_0 \rho_{1N}) \partial x' \partial y' = \vec{E}_1^i$$

or, *For* $m=1$;

$$\vec{E}_1[1+(\varepsilon_1-1)\frac{j}{2}\{\pi k_0 a \mathrm{H}_1^2(k_0 a)-2j\}]+(\varepsilon_2-1)\vec{E}_2\frac{j\pi k_0 a}{2}J_1(k_0 a)\mathrm{H}_0^{(2)}(\mathrm{K}_0\rho_{12})+(\varepsilon_3-1)\vec{E}_3$$

$$\frac{j\pi k_0 a}{2}J_1(k_0 a)\mathrm{H}_0^{(2)}(\mathrm{K}_0\rho_{13})+(\varepsilon_4-1)\vec{E}_4\frac{j\pi k_0 a}{2}J_1(k_0 a)\mathrm{H}_0^{(2)}(\mathrm{K}_0\rho_{14})+$$

$$\ldots\ldots+(\varepsilon_N-1)\vec{E}_N\frac{j\pi k_0 a}{2}J_1(k_0 a)\mathrm{H}_0^{(2)}(\mathrm{K}_0\rho_{1N})=\vec{E}_1^i$$

For $m=2$;

$$\vec{E}_2+(\varepsilon_1-1)\vec{E}_1\frac{jk_0^2}{4}\iint_{cell=1}\mathrm{H}_0^{(2)}(\mathrm{K}_0\rho_{21})\partial x'\partial y'+(\varepsilon_2-1)\vec{E}_2\frac{jk_0^2}{4}\iint_{cell=2}\mathrm{H}_0^{(2)}(\mathrm{K}_0\rho_{22})\partial x'\partial y'+(\varepsilon_3-1)\vec{E}_3$$

$$\frac{jk_0^2}{4}\iint_{cell=3}\mathrm{H}_0^{(2)}(\mathrm{K}_0\rho_{23})\partial x'\partial y'+(\varepsilon_4-1)\vec{E}_4\frac{jk_0^2}{4}\iint_{cell=4}\mathrm{H}_0^{(2)}(\mathrm{K}_0\rho_{24})\partial x'\partial y'+$$

$$\ldots\ldots+(\varepsilon_N-1)\vec{E}_N\frac{jk_0^2}{4}\iint_{cell=N}\mathrm{H}_0^{(2)}(\mathrm{K}_0\rho_{2N})\partial x'\partial y'=\vec{E}_2^i$$

or, *For* $m=2$;

$$(\varepsilon_1-1)\vec{E}_1\frac{jk_0^2}{4}\iint_{cell=1}\mathrm{H}_0^{(2)}(\mathrm{K}_0\rho_{21})\partial x'\partial y'+\vec{E}_2[1+(\varepsilon_2-1)\frac{jk_0^2}{4}\iint_{cell=2}\mathrm{H}_0^{(2)}(\mathrm{K}_0\rho_{22})\partial x'\partial y']+(\varepsilon_3-1)\vec{E}_3$$

$$\frac{jk_0^2}{4}\iint_{cell=3}\mathrm{H}_0^{(2)}(\mathrm{K}_0\rho_{23})\partial x'\partial y'+(\varepsilon_4-1)\vec{E}_4\frac{jk_0^2}{4}\iint_{cell=4}\mathrm{H}_0^{(2)}(\mathrm{K}_0\rho_{24})\partial x'\partial y'+$$

$$\ldots\ldots+(\varepsilon_N-1)\vec{E}_N\frac{jk_0^2}{4}\iint_{cell=N}\mathrm{H}_0^{(2)}(\mathrm{K}_0\rho_{2N})\partial x'\partial y'=\vec{E}_2^i$$

or, *For* $m=2$;

$$(\varepsilon_1-1)\vec{E}_1\frac{j\pi k_0 a}{2}J_1(k_0 a)H_0^2(k_0\rho_{21})+\vec{E}_2[1+(\varepsilon_2-1)\frac{j}{2}\{\pi k_0 a\mathrm{H}_1^2(k_0 a)-2j\}]+(\varepsilon_3-1)\vec{E}_3$$

$$\frac{j\pi k_0 a}{2}J_1(k_0 a)H_0^2(k_0\rho_{23})+(\varepsilon_4-1)\vec{E}_4\frac{j\pi k_0 a}{2}J_1(k_0 a)H_0^2(k_0\rho_{24})+\ldots\ldots$$

$$+(\varepsilon_N-1)\vec{E}_N\frac{j\pi k_0 a}{2}J_1(k_0 a)H_0^2(k_0\rho_{2N})=\vec{E}_2^i$$

For $m=3$;

$$\vec{E}_3+(\varepsilon_1-1)\vec{E}_1\frac{jk_0^2}{4}\iint\limits_{cell=1}\mathrm{H}_0^{(2)}(\mathrm{K}_0\rho_{31})\partial x'\partial y'+\vec{E}_2(\varepsilon_2-1)\frac{jk_0^2}{4}\iint\limits_{cell=2}\mathrm{H}_0^{(2)}(\mathrm{K}_0\rho_{32})\partial x'\partial y'+(\varepsilon_3-1)\vec{E}_3$$

$$\frac{jk_0^2}{4}\iint\limits_{cell=3}\mathrm{H}_0^{(2)}(\mathrm{K}_0\rho_{33})\partial x'\partial y'+(\varepsilon_4-1)\vec{E}_4\frac{jk_0^2}{4}\iint\limits_{cell=4}\mathrm{H}_0^{(2)}(\mathrm{K}_0\rho_{34})\partial x'\partial y'+.....$$

$$+(\varepsilon_N-1)\vec{E}_N\frac{jk_0^2}{4}\iint\limits_{cell=N}\mathrm{H}_0^{(2)}(\mathrm{K}_0\rho_{3N})\partial x'\partial y'=\vec{E}_3^i$$

or, *For* $m=3$;

$$(\varepsilon_1-1)\vec{E}_1\frac{jk_0^2}{4}\iint\limits_{cell=1}\mathrm{H}_0^{(2)}(\mathrm{K}_0\rho_{31})\partial x'\partial y'+\vec{E}_2(\varepsilon_2-1)\frac{jk_0^2}{4}\iint\limits_{cell=2}\mathrm{H}_0^{(2)}(\mathrm{K}_0\rho_{32})\partial x'\partial y'+\vec{E}_3[1+(\varepsilon_3-1)$$

$$\frac{jk_0^2}{4}\iint\limits_{cell=3}\mathrm{H}_0^{(2)}(\mathrm{K}_0\rho_{33})\partial x'\partial y']+(\varepsilon_4-1)\vec{E}_4\frac{jk_0^2}{4}\iint\limits_{cell=4}\mathrm{H}_0^{(2)}(\mathrm{K}_0\rho_{34})\partial x'\partial y'+.....$$

$$+(\varepsilon_N-1)\vec{E}_N\frac{jk_0^2}{4}\iint\limits_{cell=N}\mathrm{H}_0^{(2)}(\mathrm{K}_0\rho_{3N})\partial x'\partial y'=\vec{E}_3^i$$

or, *For* $m=3$;

$$(\varepsilon_1-1)\vec{E}_1\frac{j\pi k_0a}{2}J_1(k_0a)H_0^2(k_0\rho_{31})+\vec{E}_2(\varepsilon_2-1)\frac{j\pi k_0a}{2}J_1(k_0a)H_0^2(k_0\rho_{32})+\vec{E}_3[1+(\varepsilon_2-1)\frac{j}{2}$$

$$\{\pi k_0a\mathrm{H}_1^2(k_0a)-2j\}]+(\varepsilon_4-1)\vec{E}_4\frac{j\pi k_0a}{2}J_1(k_0a)H_0^2(k_0\rho_{34})+.....$$

$$+(\varepsilon_N-1)\vec{E}_N\frac{j\pi k_0a}{2}J_1(k_0a)H_0^2(k_0\rho_{3N})=\vec{E}_3^i$$

.....

.....

.....

For $m=N$;

$$\vec{E}_N+(\varepsilon_1-1)\vec{E}_1\frac{jk_0^2}{4}\iint\limits_{cell=1}\mathrm{H}_0^{(2)}(\mathrm{K}_0\rho_{N1})\partial x'\partial y'+\vec{E}_2(\varepsilon_2-1)\frac{jk_0^2}{4}\iint\limits_{cell=2}\mathrm{H}_0^{(2)}(\mathrm{K}_0\rho_{N2})\partial x'\partial y'+\vec{E}_3(\varepsilon_3-1)$$

$$\frac{jk_0^2}{4}\iint\limits_{cell=3}\mathrm{H}_0^{(2)}(\mathrm{K}_0\rho_{N3})\partial x'\partial y'+(\varepsilon_4-1)E_4\frac{jk_0^2}{4}\iint\limits_{cell=4}\mathrm{H}_0^{(2)}(\mathrm{K}_0\rho_{N4})\partial x'\partial y'+.....$$

$$+(\varepsilon_N-1)\vec{E}_N\frac{jk_0^2}{4}\iint\limits_{cell=N}\mathrm{H}_0^{(2)}(\mathrm{K}_0\rho_{NN})\partial x'\partial y'=\vec{E}_N^i$$

or, For $m = N$;

$$(\varepsilon_1 - 1)\vec{E}_1 \frac{j\pi k_0 a}{2} J_1(k_0 a) H_0^2(k_0 \rho_{N1}) + \vec{E}_2(\varepsilon_2 - 1)\frac{j\pi k_0 a}{2} J_1(k_0 a) H_0^2(k_0 \rho_{N2}) + \vec{E}_3(\varepsilon_3 - 1)$$

$$\frac{j\pi k_0 a}{2} J_1(k_0 a) H_0^2(k_0 \rho_{N3}) + (\varepsilon_4 - 1)\vec{E}_4 \frac{j\pi k_0 a}{2} J_1(k_0 a) H_0^2(k_0 \rho_{N4}) + \ldots\ldots\ldots\ldots$$

$$\ldots\ldots + (\varepsilon_N - 1)\vec{E}_N[1 + (\varepsilon_2 - 1)\frac{j}{2}\{\pi k_0 a \mathrm{H}_1^2(k_0 a) - 2j\}] = \vec{E}_N^i$$

The general form can be written from the above expressions in the following:

$$\sum_{n=1}^{N} C_{mn}\vec{E}_n = \vec{E}_m{}^i \quad \text{with m=1,2,3... N} \tag{A. 8}$$

The coefficients C_{mn} are given by,

$$C_{mn} = 1 + \frac{j}{2}(\varepsilon_m - 1)[\pi k_0 a_m H_1{}^{(2)}(k_0 a_m) - 2j] \quad if \; n = m \tag{A.8.a}$$

$$C_{mn} = (\varepsilon_n - 1)(j\pi k_0 a_n / 2) J_1(k_0 a_n) H_0{}^{(2)}(k_0 \rho_{mn}) \quad if \; n \neq m \tag{A.8.b}$$

For m=1,2,3,.....N and n=1,2,3.....N, (N x N) equations of (A.8) can be written in the matrix form as follows:

$$[C][\vec{E}] = [\vec{E}^i] \tag{A.9.a}$$

$$[\vec{E}] = -[C]^{-1}[\vec{E}^i] \tag{A.9.b}$$

APPENDIX B

Matrix Formulation of Scattered Field

The scattered field from equation (A. 4) of appendix A can be written

$$\begin{aligned}\vec{E}^s(x,y) &= \int G(x,y,x',y')O(x',y')\vec{E}(x',y')dx'dy' \\ &= -(j\omega^2\varepsilon_0\mu_0/4)\iint(\varepsilon_r-1)\vec{E}(x',y')H_0^{(2)}(k_0\rho)dx'dy' \\ &= -(jk_0^{\,2}/4)\iint(\varepsilon_r-1)\vec{E}(x',y')H_0^{(2)}(k_0\rho)dx'dy' \\ &= -\frac{\omega\mu_0}{4}\iint J(x',y')H_0^2(k_0\rho)dx'dy' \qquad (B.1)\end{aligned}$$

We can write from (3.11)

$$-\frac{\omega\mu_0}{4}\sum_{n=1}^{N}\vec{J}_n(x',y')\iint_{cell-n}H_0^{(2)}(k_0\rho_{mn})dx'dy' = \vec{E}_m^s \qquad (B.2)$$

The system of equations (B.2) can be written in the following form using the solution for the integral of the zero-order Hankel function over a circular region and Galerkin's method. The integral equation (B.1) can be discretized by the method of moment (MoM). If a_n represents the radius of the equivalent circular cell which has the same cross section area as small square cell n and m=1,2,3...N

$$\sum_{n=1}^{N}\frac{-\omega\mu_0}{2k_0^2}\left[\pi k_0 a_m \mathrm{H}_1^{(2)}(k_0a_m)-2j\right]\vec{J}_m = \vec{E}_m^{\,s} \quad if \quad m=n \qquad (B.2.a)$$

$$\sum_{n=1}^{N}\frac{-\pi\omega\mu_0 a_n}{2k_0}J_1(k_0a_n)\mathrm{H}_0^{(2)}(k_0\rho_{mn})\vec{J}_n = \vec{E}_m^{\,s} \quad if \quad m\neq n \qquad (B.2.b)$$

We obtain the following equation putting m=1,2,3...N and n=1,2,3...N in (B.2.a) and (B.2.b).

For $m = 1;$

$$\frac{-\omega\mu_0}{2k_0^2}[\pi k_0 a \mathrm{H}_1^{(2)}(k_0 a) - 2j]\vec{J}_1 + \frac{-\pi\mu_0 a\omega}{2k_0} J_1(k_0 a)\mathrm{H}_0^{(2)}(k_0\rho_{12})\vec{J}_2 +$$

$$\frac{-\pi\mu_0 a\omega}{2k_0} J_1(k_0 a)\mathrm{H}_0^{(2)}(k_0\rho_{13})\vec{J}3 + \frac{-\pi\mu_0 a\omega}{2k_0} J_1(k_0 a)\mathrm{H}_0^{(2)}(k_0\rho_{14})\vec{J}_4 +$$

$$\ldots\ldots + \frac{-\pi\mu_0 a\omega}{2k_0} J_1(k_0 a)\mathrm{H}_0^{(2)}(k_0\rho_{1N})\vec{J}_N = E_1^s$$

For $m = 2;$

$$\frac{-\omega\mu_0}{2k_0^2}[\pi k_0 a \mathrm{H}_1^{(2)}(k_0 a) - 2j]\vec{J}_2 + \frac{-\pi\mu_0 a\omega}{2k_0} J_1(k_0 a)\mathrm{H}_0^{(2)}(k_0\rho_{21})\vec{J}_1 +$$

$$\frac{-\pi\mu_0 a\omega}{2k_0} J_1(k_0 a)\mathrm{H}_0^{(2)}(k_0\rho_{23})\vec{J}3 + \frac{-\pi\mu_0 a\omega}{2k_0} J_1(k_0 a)\mathrm{H}_0^{(2)}(k_0\rho_{24})\vec{J}_4 +$$

$$\ldots\ldots + \frac{-\pi\mu_0 a\omega}{2k_0} J_1(k_0 a)\mathrm{H}_0^{(2)}(k_0\rho_{2N})\vec{J}_N = E_2^s$$

For $m = 3;$

$$\frac{-\omega\mu_0}{2k_0^2}[\pi k_0 a \mathrm{H}_1^{(2)}(k_0 a) - 2j]\vec{J}_3 + \frac{-\pi\mu_0 a\omega}{2k_0} J_1(k_0 a)\mathrm{H}_0^{(2)}(k_0\rho_{31})\vec{J}_1 +$$

$$\frac{-\pi\mu_0 a\omega}{2k_0} J_1(k_0 a)\mathrm{H}_0^{(2)}(k_0\rho_{32})\vec{J}_2 + \frac{-\pi\mu_0 a\omega}{2k_0} J_1(k_0 a)\mathrm{H}_0^{(2)}(k_0\rho_{34})\vec{J}_4 +$$

$$\ldots\ldots + \frac{-\pi\mu_0 a\omega}{2k_0} J_1(k_0 a)\mathrm{H}_0^{(2)}(k_0\rho_{3N})\vec{J}_N = E_3^s$$

For $m = 4;$

$$\frac{-\omega\mu_0}{2k_0^2}[\pi k_0 a \mathrm{H}_1^{(2)}(k_0 a) - 2j]\vec{J}_4 + \frac{-\pi\mu_0 a\omega}{2k_0} J_1(k_0 a)\mathrm{H}_0^{(2)}(k_0\rho_{41})\vec{J}_1 +$$

$$\frac{-\pi\mu_0 a\omega}{2k_0} J_1(k_0 a)\mathrm{H}_0^{(2)}(k_0\rho_{42})\vec{J}_2 + \frac{-\pi\mu_0 a\omega}{2k_0} J_1(k_0 a)\mathrm{H}_0^{(2)}(k_0\rho_{43})\vec{J}_3 +$$

$$\ldots\ldots + \frac{-\pi\mu_0 a\omega}{2k_0} J_1(k_0 a)\mathrm{H}_0^{(2)}(k_0\rho_{4N})\vec{J}_N = E_4^s$$

.....

.....

.....

.....

For $m = N$;

$$\frac{-\omega\mu_0}{2k_0^2}[\pi k_0 a \mathrm{H}_1^{(2)}(k_0 a) - 2j]\vec{J}_N + \frac{-\pi\mu_0 a\omega}{2k_0} J_1(k_0 a)\mathrm{H}_0^{(2)}(k_0\rho_{N1})\vec{J}_1 +$$

$$\frac{-\pi\mu_0 a\omega}{2k_0} J_1(k_0 a)\mathrm{H}_0^{(2)}(k_0\rho_{N2})\vec{J}_2 + \frac{-\pi\mu_0 a\omega}{2k_0} J_1(k_0 a)\mathrm{H}_0^{(2)}(k_0\rho_{N3})\vec{J}_3 +$$

$$\ldots\ldots + \frac{-\pi\mu_0 a\omega}{2k_0} J_1(k_0 a)\mathrm{H}_0^{(2)}(k_0\rho_{N4})\vec{J}_4 = E_N^s$$

The above expressions are written in general form:

$$\sum_{n=1}^{N} D_{mn}^b \vec{J}_n = \vec{E}_m^{\ s} \quad \text{with m = 1, 2, 3... N} \tag{B.3}$$

The coefficients D_{mn} are given by ,

$$D_{mn} = \frac{-1}{2\omega\varepsilon_0}[\pi k_0 a_m H_1^{(2)}(k_0 a_m) - 2j] \quad \text{if } n = m \tag{B.4.a}$$

$$D_{mn} = \frac{-\pi\eta_0 a_n}{2} J_1(k_0 a_n) H_0^{(2)}(k_0 \rho_{mn}) \quad \text{if } n \neq m \tag{B.4.b}$$

(N x N) equations of (B.4) can be written in the matrix form as follows for m=1,2,3,.....N and n=1,2,3.....N:

$$[D][\vec{J}] = [\vec{E}^s] \tag{B.6.a}$$

$$[\vec{J}] = -[D]^{-1}[\vec{E}^s] \tag{B.6.b}$$

APPENDIX C

Formulation of various fields for analytical Solution

Expressions for analytical solution of electric field inside a homogeneous circular dielectric for TM excitation are given in [50].

If a TM_z uniform plane wave traveling in the +x direction in free space shown in fig.C.1 is incident normally on lossless dielectric circular cylinder of radius 'a', the incident, scattered and transmitted (into the cylinder) electric field can be written as following:

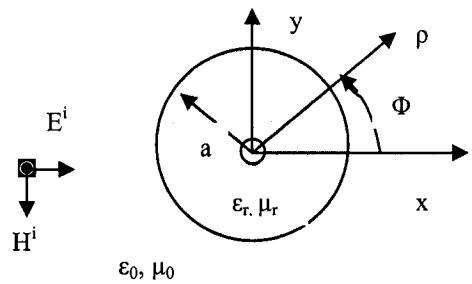

Fig.C.1 The cylindrical object emerged in free space

$$\vec{E}^i = \hat{z}E_z^i = \hat{z}E_0 e^{-jkx} \tag{C.1}$$

$$\vec{E}^i = \hat{z}E_0 \sum_{n=-\infty}^{\infty} j^{-n} J_n(k_0\rho) e^{jn\phi} \tag{C.2}$$

$$\vec{E}^s = \hat{z}E_0 \sum_{n=-\infty}^{\infty} a_n H_n^{(2)}(k_0\rho) e^{jn\phi} \tag{C.3}$$

$$\vec{E}^d = \hat{z}E_0 \sum_{n=-\infty}^{\infty} [b_n J_n(k_d\rho) + c_n Y_n(k_d\rho)] e^{jn\phi} = \hat{z}E_0 \sum_{n=-\infty}^{\infty} b_n J_n(k_d\rho) e^{jn\phi} \tag{C.4}$$

$$c_n = 0 \tag{C.5}$$

$$a_n = j^{-n} \frac{J_n'(k_0a)J_n(k_da) - \sqrt{(\varepsilon_r/\mu_r)}J_n(k_0a)J_n'(k_da)}{\sqrt{(\varepsilon_r/\mu_r)}J_n'(k_da)H_n^{(2)}(k_0a) - J_n(k_da)H_n^{(2)'}(k_0a)} \tag{C.6}$$

$$b_n = j^{-n} \frac{J_n(k_0a)H_n^{(2)'}(k_0a) - J_n'(k_0a)H_n^{(2)}(k_0a)}{J_n(k_da)H_n^{(2)'}(k_0a) - \sqrt{(\varepsilon_r/\mu_r)}J_n'(k_da)H_n^{(2)}(k_0a)} \tag{C.7}$$

Numerical technique: $\pm n$ = truncation number = round ($3k_d a+10$) instead of $\pm\infty$.

$$J_n'(k_0a) = -J_{n+1}(k_0a) + \frac{n}{k_0a}J_n(k_0a) \tag{C.8}$$

$$H_n^{(2)'}(k_0a) = -H_{n+1}^{(2)}(k_0a) + \frac{n}{k_0a}H_n^{(2)}(k_0a) \tag{C.9}$$

Where, $\mu_r = 1$.

REFERENCES:

[1] L.E. Larsen and J. H. Jacobi, Eds., "Medical application of Microwave Imaging". New York: IEEE press, 1986.

[2] S. Caorsi, Andrea Massa, and M. Pastorino, " Numerical assessment concerning a focused microwave diagnostic method for medical application" IEEE trans. Microwave theory Tech., vol. 48, no.11, pp. 1815-1830, Nov. 2000.

[3] Q.H. Liu, Z.Q. Zhang, T.T. Wang, J.A. Bryan, G.A. Ybarra, L.W. Nolte, W.T. Joines, " Active Microwave Imaging I-2-D forward and inverse scattering methods" IEEE trans. On Microwave Theory and Tech. Vol. 50, no. 1, pp.123-133, 2002.

[4] Committee on Technologies for the early Detection of Breast Cancer, Mammography and Beyond: Developing Technologies for early Detection of cancer, S. J. Nass, I. C. Henderson, and J.C. Lashof, Eds, National Cancer Policy Board, Institute of Medicine and Commission on life studies, National research council, 2001.

[5] E. C. Fear, S. C. Hagness, P. M. Meaney, M. Okoniewski, and M. A. Stuchly, "Enhancing breast tumor detection with near-field imaging", IEEE microwave magazine, pp. 48-56, March 2002.

[6] P. M. Meaney, M.W. Fanning, D. Li, S. P. Poplack, and K.D. Paulsen, "A clinical prototype for active microwave imaging of the breast" IEEE trans. Microwave theory Tech., vol. 48, pp. 1841- 1853, Nov, 2000.

[7] Jean-Charles Bolomy, "Recent European Developments in active microwave imaging for industrial, scientific and medical application", IEEE trans., on Microwave theory and Tech. vol. 37, no. 12, Dec.1989.

[8]: R.F. Harrington, "Field computation by Moment Method", New York: Macmillan, 1968.

[9]: J.H. Richmond, " Scattering by dielectric cylinder of arbitrary cross-section shape," IEEE trans. Antenna Prop. Vol. AP-13, issue 3, pp. 334-341, 1965.

[10]: M. M. Ney, "Method of Moments as applied to electromagnetic problems" IEEE trna. Microwave Theory Tech., vol. MTT-33, pp. 972-980, 1985.

[11] R. Penrose, "A generalized inverse for matrices," Proc. Cambridge Phil. Soc., vol. 51, pp. 406-413,1955.

[12] "Computational Methods for Electromagnetics" , A. Peterson , IEEE Press , pp. 59-65, 1998.

[13] S. Caorsi, G.L. Gragnani, and M. Pastorino, " Two-Dimensional microwave imaging by a numerical inverse scattering solution" IEEE trans. Microwave theory Tech., vol. 38,no. 8, pp. 981-988, May 1990.

[14] J. B. Keller, "Geometrical theory of diffraction," J. Opt. Soc. AM. Vol. 52, pp. 116, 1962.

[15] R. Gomez, A. Salinas, A. Rubio Bretores and M. Martin, "Time-domain integral equation for EMP analysis transmission-line system," Int. J. Num. Mod., vol. 4, pp. 153-162, 1991.

[16] E. K. Miller, "A selective survey of computational electromagnetic," IEEE Trans. Antennas Propagat., vol. 36, pp. 1281-1305,1988.

[17] K.S. Yee, " Numerical solution of initial boundary value problems involving Maxwell's equations in isotropic media," IEEE Trans. Antennas Propagat., vol. 14, pp. 302 – 307, 1966.

[18] S. Akhtarzad, and P. B. Johns, "Solution of Maxwell's equations in three space dimensions and time by the TLM method of numerical analysis," Proc. IEE vol. 122, pp. 1344- 1348, 1975.

[19] P. Silvester, " Finite Elements for Electrical Engineers," Camberidge University Press, New York, 1983.

[20] R.K. Muller, M. kaveh and G. Wade, "Reconstructive Tomography and application to ultrasonic" Proc. IEEE, vol. 67, pp. 567-587, 1979.

[21] M. Slaney, A.C. Kak and L.E. Larsen, "Limitations of imaging with first order diffraction tomography" IEEE trans. Microwave Theory Tech., vol. MTT-32, pp. 860-873,1984.

[22] J.V. Candy and C. Pichot, "Active microwave imaging: a model based approach" IEEE trans. Antennas Prop., vol. AP-39, pp. 285-290, 1991.

[23] F. C. Lin and M.A. Fiddy, "Image estimation from scattered field data" Int. J. Image Syst. Tech., vol. 2, pp. 76-95, 1990.

[24] L. Joffre, M. S. Hawley, A. Broquetas, E. Delos Reyes, M. Fernando and A. R. Elias-Fuste, "Medical imaging with microwave tomographic scanner" IEEE Trans. Biomed. Eng., Vol. BME-37, pp. 303-312, 1990.

[25] M.M. Ney, A. M. Smith, and S.S. stuchly, " A solution of electromagnetic imaging using pseudo-inverse transformation" IEEE trans. Med. Imaging, vol. MI-3, pp. 155-162,1984.

[26] C. N. Dorny, "A Vector Space Approach to Models and Optimazation," Huntigton, New York, Krieger, 1980.

[27] S. Coarsi, S. Ciaramella and L. Gragnani, "On the use of regularization techniques in

numerical inverse-scattering solutions for microwave imaging applications", IEEE trans. Microwave Theory Tech., vol. MTT-43, pp. 632-640, 1995.

[28] "Equivalent current density reconstruction for microwave imaging purposes", S. Coarsi, G.L. Gragnani and Pastorino, IEEE trans. on MTT, vol. 37, no. 5, pp. 910-916 1989.

[29] "An approach to Microwave Imaging using a multiview Moment Method solution for a two-dimensional infinite cylinder", S. Caorsi, G.L. Gragnani and M. Pastorino, IEEE Trans. On MTT, vol. 39, no. 6, pp. 1062-1067,1991.

[30] "Electromagnetic vision-oriented numerical solution to three-dimensional inverse scattering", S. Coarsi, G. L. Gragnani, and M. Pastorino, Radio sci., vol. 23, pp. 1094-1106, 1988.

[31] S. Coarsi, G. L. Gragnani, and M. Pastorino, "Redundant electromagnetic data for microwave imaging of three-dimensional diel;ectric objects", IEEE trans. Antennas propagat., vol. Ap-42,pp. 581-589,1994.

[32] M. Moghaddam and W.C. Chew, "Study of some practical issues in inversion with the Born iterative method using time-domain data", IEEE trans. Antennas Prop., vol. AP-41, pp. 177-184, 1993.

[33] N. Jaochimowicz, C. Pichot and J. P. Hugonin, "Inverse scattering: an iterative numerical method for electromagnetic imaging", IEEE Trans. Antennas Prop., vol. AP-39, pp. 1742-1752, 1991.

[34] A.N. Tikhonov and V.Y. Arsenin, "Solution of ill-posed problems". V.H. Winston & Sons, 1977.

[35] Y. Liu and I. R. Ciric, "A more convergent iterative algorithm for electromagnetic

imaging," IEEE Trans. Magnetics, vol. 31, pp. 1302-1305, 1995.

[36] Y. Liu and I. R. Ciric, "An adaptive algorithm for electromagnetic imaging", IEEE Trans. Magnetics, Vol. 32, pp. 1302-1305, 1996.

[37] A. Franchois and C. Pichot, "Microwave imaging-complex permittivity reconstruction with a Levenberg-Marquardt method", IEEE Trans. Antennas Prop., vol. AP-45, pp. 203-215, 1997.

[38] P. Lobel, R. kleinman, C. Pichot, L. Feraud and M. Barluad, "Conjugate gradient method for solving inverse scattering with experimental data", IEEE Antenns prop. Mag., vol. 38, pp. 45-51, 1996.

[39] P. Lobel, C. Pichot, L. Feraud and M. Barluad, "Conjugate gradient algorithm with edge-preserving regularization for image reconstruction from experimental data", IEEE AP-S Int. symp., vol. 1, pp. 644-647, Baltimore, USA, 1996.

[40] P. M. Meaney, K. D. Paulsen and T. R. Ryan, "Two-dimensional hybrid element image reconstructed for TM illumination", IEEE Trans. Antennas Prop., vol. AP-43, pp. 239-247, 1995.

[41] Y. Qin, I. R. Ciric, "High-resolution electromagnetic imaging of lossy objects in the presence of noise", IEEE Trans. Magnetics, vol. 31, pp. 1936-1939, 1995.

[42] Y. Qin, I. R. Ciric, "Efficient techniques for choosing the regularization parameter for electromagnetic imaging", Proc. ANTEM'96, 1996, (Montreal, Canada).

[43] Y. Qin, I. R. Ciric, "Method of selecting regularization parameter for microwave imaging", Electron. Letters, vol. 30, pp. 2028-2029, 1994.

[44] M. Baribuad, "Microwave imagery: analytical method and maximum entopy method", J. Appl. Phys., vol. 23, pp. 269-287, 1990.

[45] L. Garnero, A. Franchois, J. P. Hugonin, C. Pichot and N. Joachimowicz, "Microwave imaging-complex permittivity reconstruction by simulated annealing", IEEE Trans. Microwave Theory Tech., vol. MTT-39, pp. 1801-1807, 1991.

[46] S. Coarsi, G. L. Gragnani, S. Medicina, M. Patorino and Z. Zunino, "Microwave imaging method using a simulated annealing approach", IEEE Microwave guide letters, vol. 1, pp. 331-333, 1991.

[47] D.O. Batrakov, and N.P. Zhuk, "An iterative solution to the inverse problem of remote sensing of nonuniform media based on values of the polarization parameters," J. Commun. Tech. Elec., vol. 38, pp. 108-115, 1993.

[48] D. O. Batrakov, and P. N. Zhuk, "Solution of general inverse scattering problem using the distorted Born approximation and iterative technique," Inverse problems, vol. 10, pp. 39-54, 1994.

[49] C. T. Tai, "Dyadic Green's functions in Electromagnetic Theory." Scranton, PA: International Textbook Company, 1971.

[50] Chapter 11' "Advanced Engineering Electromagnetics" C. Balanis, Wiley, 1989.

[51] J. Hadamard, "Lectures on Chauchy's Problem in linear Partial Differential Equation" New Haven, CT, Yale University. Press, 1923.

[52] T.K. Sarkar, D.D. Weiner and V.K. Jain, "Some mathematical considerations in dealing with inverse problems" IEEE trans. Antenna Propagation, vol. AP-29, pp. 373-37, 1981.

[53] J. H. Richmond, " TE-wave scattering by dielectric cylinder of arbitrary cross-section shape" vol. AP-14, no. –4, pp. 460 – 464, IEEE trans. On Antenna and Propagation, July, 1966.

[54] W. Weiyan, and Z. Shourong, "Unrelated illumination method for electromagnetic inverse scattering of inhomogeneous lossy dielectric bodies," IEEE Trans. Antenna propagat., vol. 40, pp. 1292-1296, 1992.

[55] Shakti K. Davis, Henri Tandradinata, Susan C. Hagness, Barry D. Van Veen, "ultrawideband microwave breast cancer detection:a detection-theoretic approach using thegeneralized likelihood ratio test," IEEE Trans. on biomedical engineering, VOL. 52, NO. 7, JULY 2005, page: 1237-1250

[56] Hermann Singer, Heinz-Dietrich Briins, Guido Burger , "State of the art in the method of moments," IEEE international symp.on electromagnetic compatibility, 19-23 Aug.1996, page:122-127